Structural insights into the oligomeric assembly of EHD2 and its role at caveolae

Inaugural Dissertation
to obtain the academic degree
Doctor rerum naturalium (Dr. rer. nat.)

submitted to the Department of Biology, Chemistry, Pharmacy
of Freie Universität Berlin

Elena Vázquez Sarandeses

Berlin, Germany

2023

The present work was carried out between February 2019 and June 2023 at the Max-Delbrück Center for Molecular Medicine (MDC-Berlin) under the supervision of Prof. Dr. Oliver Daumke.

1st Reviewer: Prof. Dr. Oliver Daumke

2nd Reviewer: Prof. Dr. Volker Haucke

Date of defense: 27.02.2024

Declaration of Independence / Selbstständigkeitserklärung

Herewith I certify that I have prepared and written my thesis independently and that I have not used any sources and aids other than those indicated by me.

Hiermit bestätige ich, dass ich die vorliegende Arbeit selbstständig und nur unter Zuhilfenahme der angegebenen Literatur erstellt habe.

Berlin, 01.11.2024

_____
Signature / Unterschrift

Table of contents

Summary

Eps15-homology domain containing protein 2 (EHD2) is a dynamin-related ATPase which is thought to localize to the neck of caveolae and participate in their stabilization at the plasma membrane. Similar to other members of the dynamin family, EHD2 oligomerizes upon recruitment to artificial lipid bilayers and induces membrane tubulation. X-ray crystallography and cryo-Electron Tomography (cryo-ET) studies indicated that EHDs exist as open dimers in solution and as closed oligomers on membranes, and that the transition between the two states is triggered by membrane curvature. However, structural and mechanistic details about how EHD2 restricts caveolae mobility, the regulatory roles of specific domains in oligomeric assembly and the coordination of the ATP hydrolysis cycle with conformational changes in EHD2 have remained obscure.

To address these open questions, full-length (FL) and N-terminally truncated (ΔN) EHD2 were reconstituted on tubular membranes. Cryo-Electron Tomography (cryo-ET) and Subtomogram Averaging (StA) yielded structures of membrane-bound oligomeric EHD2-FL and EHD2ΔN at an average resolution of 6.7 and 11 Å, respectively, and a model of the EHD2 oligomers was obtained by a flexible fitting and refinement approach. EHD2 in its closed conformation forms ring-shaped oligomers, which embrace the most highly curved regions of the membrane tubules, while adjacent membrane regions without an EHD2 coat bulge out, suggesting membrane curvature stabilization via a scaffolding and wedging mechanism. In the cryo-ET map, an N-terminal sequence stretch projects towards the membrane. Its deletion did not abolish oligomerization and membrane tubulation but led to a tight compaction of adjacent EHD2 oligomeric filaments, in line with a role of the N-terminus in coordinating membrane binding with proper spatial organization of the EHD2 filaments in their environment. A large-scale movement consisting of distancing and rotation of the EH domains from their position in the closed EHD2 dimer, allows assembly via the G-interface, thereby explaining the auto-inhibition role of the EH domain. Biochemical and cryo-ET studies revealed that ATP binding is required for oligomeric assembly, whereas ATP hydrolysis appears to drive the disassembly. Finally, it was shown that the necks of caveolae are significantly narrower and more elongated in the absence of EHD2, supporting a role of EHD2 in the stabilization of caveolae at the plasma membrane.

Results of this thesis refine our knowledge of the structural transition from EHD2 dimers in solution to ring-shaped filaments on membranes as a prerequisite to understand the cellular function of EHD2 in restricting caveolae to the plasma membrane.

Zusammenfassung

Das „Eps15-homology domain containing protein 2 (EHD2)“ ist eine Dynamin-verwandte ATPase, von der man annimmt, dass sie am Hals von Caveolae lokalisiert ist und an deren Stabilisierung an der Plasmamembran beteiligt ist. Ähnlich wie andere Mitglieder der Dynamin-Familie oligomerisiert EHD2 nach Anlagerung an artifizielle Lipiddoppelschichten und induziert Membrantubulation. Röntgenkristallographie- und Kryo-Elektronentomographie-Studien deuten darauf hin, dass EHDs in Lösung als offene Dimere und auf Membranen als geschlossene Oligomere vorliegen und dass der Übergang zwischen den beiden Zuständen durch Bindung an gekrümmte Membranen ausgelöst wird. Strukturelle und mechanistische Details darüber, wie EHD2 die Mobilität von Caveolae einschränkt und wie spezifische Domänen die Oligomerbildung regulieren und den ATP-Hydrolysezyklus mit Konformationsänderungen koordinieren, sind jedoch unklar.

Um diese offenen Fragen zu klären, wurde EHD2 in voller Länge (FL) und N-terminal verkürzt (ΔN) auf Membranentubuli rekonstituiert. Strukturen von membrangebundenen EHD2-FL und EHD2ΔN-Oligomeren wurden mittels Kryo-Elektronentomographie (Kryo-ET) und Subtomogram Averaging mit einer durchschnittlichen Auflösung von 6,7 bzw. 11 Å gelöst, und ein Modell der Oligomere durch flexible Einpassung und Verfeinerung erstellt. EHD2 bildet in seiner geschlossenen Konformation ringförmige Oligomere aus, die die am stärksten gekrümmten Bereiche der Membrantubuli umschließen, während sich benachbarte Membranbereiche ohne EHD2-Hülle ausbeulen, was auf eine Stabilisierung der Membrankrümmung durch einen Gerüst- und Einkeilungsmechanismus hindeutet. In der Kryo-ET-Karte ragt ein N-terminaler Sequenzabschnitt in Richtung der Membran; seine Deletion hob die Oligomerisierung und Tubulation nicht auf, sondern führte zu einer engen Verdichtung benachbarter oligomerer EHD2-Filamente. Dies steht mit einer Rolle des N-Terminus für der Koordinierung der Membranbindung mit der richtigen räumlichen Organisation der EHD2-Filamente in ihrer Umgebung in Einklang. Eine weitreichende Bewegung der EH-Domänen von ihrer Position im geschlossenen EHD2-Dimer zu einer neuen Stelle an der Oberseite des Filaments ermöglicht die Assemblierung über eine Interaktionsfläche in der GTPase-Domäne und erklärt damit die Rolle der EH-Domäne in der Autoinhibition. Biochemische und Kryo-ET-Studien ergaben, dass ATP-Bindung für den Zusammenbau des Oligomers erforderlich ist, während ATP-Hydrolyse dessen Abbau zu steuern scheint. Schließlich wurde gezeigt, dass die Hälse der Caveolae in Abwesenheit von EHD2 deutlich schmaler und länger sind, was die Rolle von EHD2 bei der Stabilisierung der Caveolae an der Plasmamebran unterstützt.

Die Ergebnisse dieser Arbeit verfeinern unser Wissen zu den strukturellen Übergängen von EHD2-Dimeren in Lösung zu ringförmigen Filamenten auf Membranen als Voraussetzung, um die zellulären Funktion von EHD2 bei der Stabilisierung von Caveolae an der Plasmamembran besser zu verstehen.

1. Introduction

1.1. Biological membranes in eukaryotes

Biological membranes are defined by a double layer of lipid molecules, including phospholipids, glycolipids, and sterols, known as the phospholipid bilayer. Along with different types of lipids, membrane proteins and sugars are also important constituents. All these components are essential to maintain membrane structural integrity, organization and flow of material (Watson, 2015). Membranes not only define cell and organelle boundaries, but they also function as an essential medium for intracellular communication (Cheng & Smith, 2019). In fact, a complex system of intracellular membranes is responsible for sorting, processing, and transporting different types of cargoes, such as membranes themselves, but also proteins and other molecules (Figure 1). These are transported inside vesicles, in both the anterograde (from the endoplasmic reticulum towards the plasma membrane) and retrograde (from the plasma membrane to organelles) directions, to and from the plasma membrane or other cellular compartments (Watson, 2015). Membrane trafficking in both directions is a highly selective and controlled process which involves a myriad of proteins and signaling mechanisms (Cheng & Smith, 2019).

Membranes are also fundamental for the vesicular transport of cargo between the cytoplasm and the extracellular space. Exocytosis consists of the fusion of vesicles with the plasma membrane and results in the release of the vesicular material into the extracellular space. The vesicular transfer of material in the opposite direction, namely the internalization of extracellular cargo, is termed endocytosis (Wu et al., 2016) (Figure 1).

Cellular membranes normally adopt flat shapes and energy is needed to deform them into curved bilayers competent for the multiple cellular processes in which they are involved. There is a plethora of protein machineries specialized in promoting and executing membrane deformation activities (Bonifacino & Glick, 2004). In general, shape transformations of membranes can be divided into two classes: 1) reshaping is due to distortions of the membrane continuity and reconnections of its surface, and 2) the change in membrane shape results from bending and does not require disruptions nor re-connections of the membrane (Campelo et al., 2010). The first class refers to fission and fusion activities, which topologically transform the membrane. Some examples are the fusion of docked vesicles with the plasma membrane by synaptotagmin (Martens et al., 2007), the fusion of ER tubules by atlastin (Wang et al., 2016), or the fission of clathrin coated vesicles by dynamin (Praefcke & McMahon, 2004).

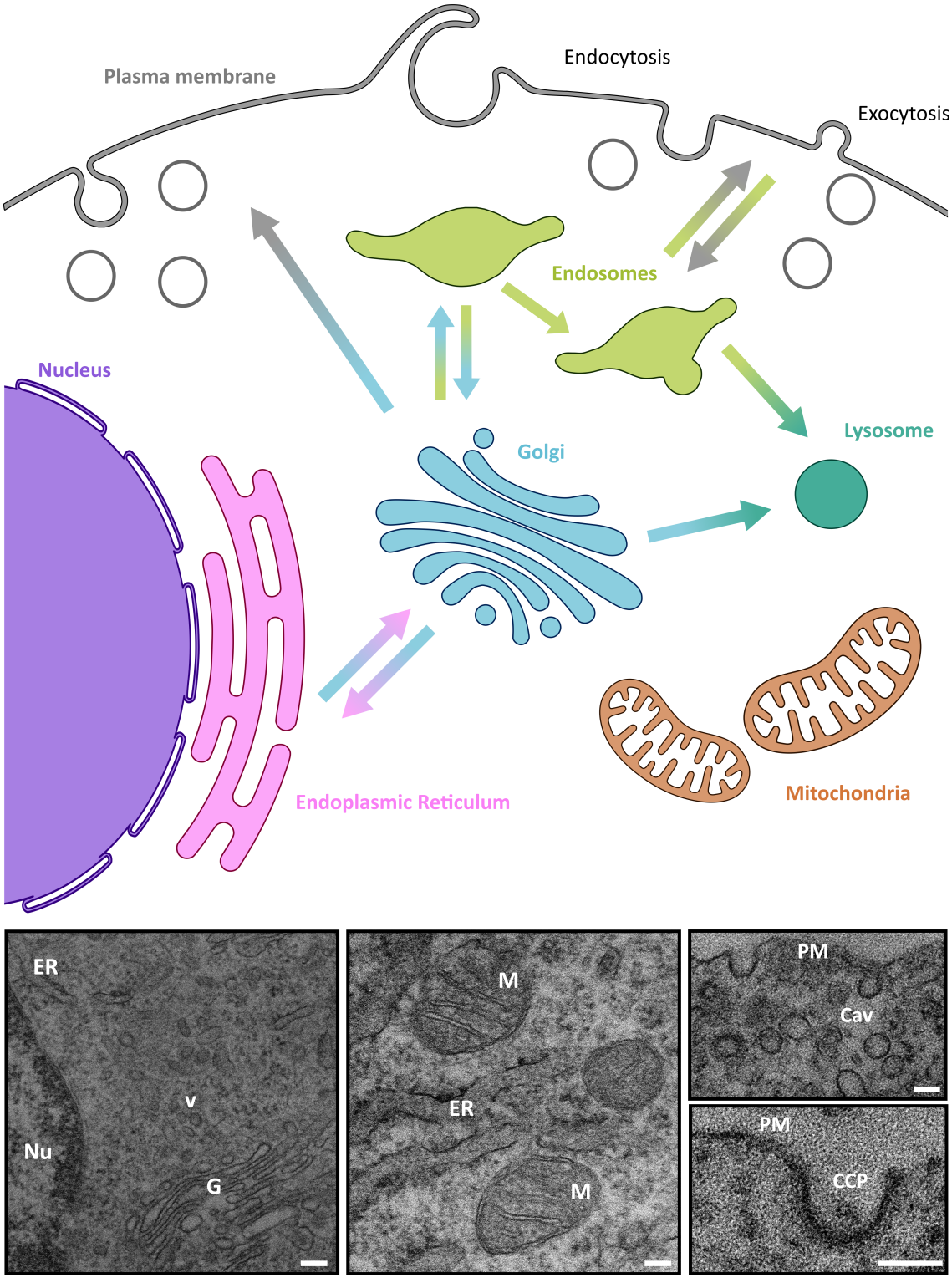

Figure 1. Biological membranes. Schematic representation of cellular membranes and trafficking. Arrows indicate trafficking of membranous vesicles. Electron micrographs from epoxy-embedded mouse embryonic fibroblasts show prominent membranous organelles involved in trafficking. PM: plasma membrane; Cav: caveolae; CCP: clathrin coated pit; ER: endoplasmic reticulum; Nu: nucleus; G: golgi; v: vesicles; M: mitochondria. Scale bars: 100 nm.

The second class of membrane deformation is often referred to as the generation of membrane curvature and it includes activities like flattening, tubulating, or squeezing. Proteins that belong to this class have the ability to bind to lipid bilayers and to bend them (Campelo et al., 2010). Membrane bending is particularly relevant in this study, and it is further introduced below.

1.1.1. Membrane remodelling – generation of curvature

Membrane curvature is an important parameter in defining the morphology of cells, organelles and local membrane subdomains (McMahon & Boucrot, 2015). Curvature can be dynamically modulated by several different mechanisms, including: 1) changes in lipid composition, 2) influence of integral membrane proteins that have intrinsic curvature or have curvature on oligomerization, 3) changes in cytoskeletal polymerization and pulling by motor proteins, 4) direct and indirect scaffolding of the bilayer, 5) active amphipathic helix insertion into a leaflet of the lipid bilayer, and 6) protein crowding originating from nonspecific and concentration-dependent interactions between the membrane surface and proteins associated with it (Kozlov & Taraska, 2023; McMahon & Gallop, 2005). A schematic representation of some of these mechanisms is shown in Figure 2.

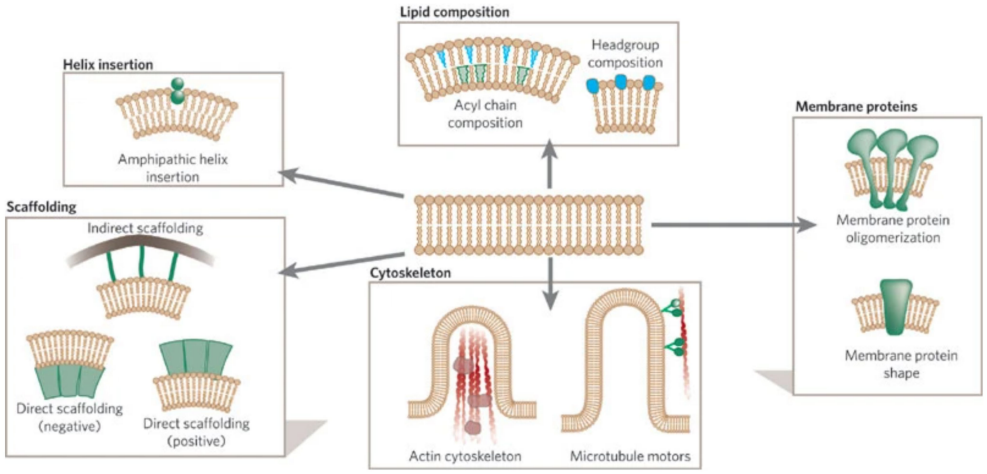

Figure 2. Mechanisms of membrane deformation. Five mechanisms for membrane remodelling that generate positive or negative curvature, according to (McMahon & Gallop, 2005).

For the work presented in this thesis about the dynamin-related protein EHD2 (Eps15-homology domain-containing protein 2), the mechanisms of hydrophobic insertion and scaffolding are of special importance.

Hydrophobic insertion, or wedging, is mediated by the embedding of amphipathic helices or of small hydrophobic loops and hairpins into the hydrophobic core of a lipid monolayer. This insertion creates a local structural asymmetry which causes bending (Kozlov & Taraska, 2023). These types of insertions generate curvature only locally, generally within a few nanometers around the embedded protein domains (Kozlov & Taraska, 2023). Some well-characterized examples of hydrophobic insertion are the ENTH domains of epsins (Kroppen et al., 2021), the ANTH domains of CALM (Miller et al., 2015), the N-BAR family of proteins (Gallop et al., 2006), the small GTPases Sar1 (Joiner & Fromme, 2021) and Arf1 (Hooy et al., 2022) involved in the formation of COPII and COPI coats, respectively, or the C2A and C2B domains of synaptotagmin 1 (Martens et al., 2007).

The scaffolding mechanism requires the binding of a hydrophilic domain which possesses an intrinsically curved shape to the lipid bilayer surface (Campelo et al., 2010; Kozlov & Taraska, 2023). The attractive interactions established between the protein scaffold and the membrane surface must be stronger than the resistance of the bilayer to bend. The scaffold must be sufficiently rigid compared to the membrane and the energy of the protein-lipid interaction must be larger than the energy cost of the bilayer deformation (Campelo et al., 2010; Kozlov & Taraska, 2023). Typically, the curvature originates from electrostatic interactions between oppositely charged groups, for example positively charged residues in the protein and the negatively charged phospholipids. Sometimes, the curvature may also be caused by binding to adaptor proteins anchored in the membrane (Campelo et al., 2010; Kozlov & Taraska, 2023). Scaffolding is a universally employed mechanism by a vast variety of proteins, some examples are: core subunits of retromers (Leneva et al., 2021), dimers of sorting nexins (SNXs) (Lopez-Robles et al., 2023), the homopentameric B subunits of Shiga toxins (StxB) (Delivery et al., 2021), COPI (Dodonova et al., 2015) and COPII (Hutchings et al., 2018) proteins, dynamin (Kong et al., 2018), ESCRT protein complexes (Pavlin & Hurley, 2020), or the intraviral protein Gag in HIV (Sundquist & Kra, 2012).

1.2. Endocytosis

Endocytosis is described as the *de novo* generation of internal membranes from the plasma membrane. This mechanism allows the incorporation of plasma membrane lipids, integral proteins and extracellular molecules and fluid (Gary J. Doherty & Mcmahon, 2009). Endocytosis is a key cellular pathway involved in a multitude of essential and seemingly disparate processes such as mitosis, antigen presentation, nutrient uptake, transmembrane receptor internalization, recycling, extracellular milieu sensing, plasma membrane maintenance and composition and cell migration, among others (Gary J. Doherty & Mcmahon, 2009; Thottacherry et al., 2019). In addition, pathogens often exploit endocytic routes to integrate inside the cell (Gary J. Doherty & Mcmahon, 2009). Diverse endocytic systems operate in a cell (Figure 3). However, the prerequisite of a budding structure from the plasma membrane is common to all of them (Gary J. Doherty & Mcmahon, 2009). To date, the classification of endocytic mechanisms is based on whether clathrin is required for the budding process (Thottacherry et al., 2019). Thus, endocytosis can be clathrin-mediated, known as CME (clathrin-mediated endocytosis) or clathrin-independent, CIE (clathrin-independent endocytosis). The activation of CME or CIE depends on the cellular type and context, on the cargo to be internalized and its destination, and on the proteins involved (Thottacherry et al., 2019).

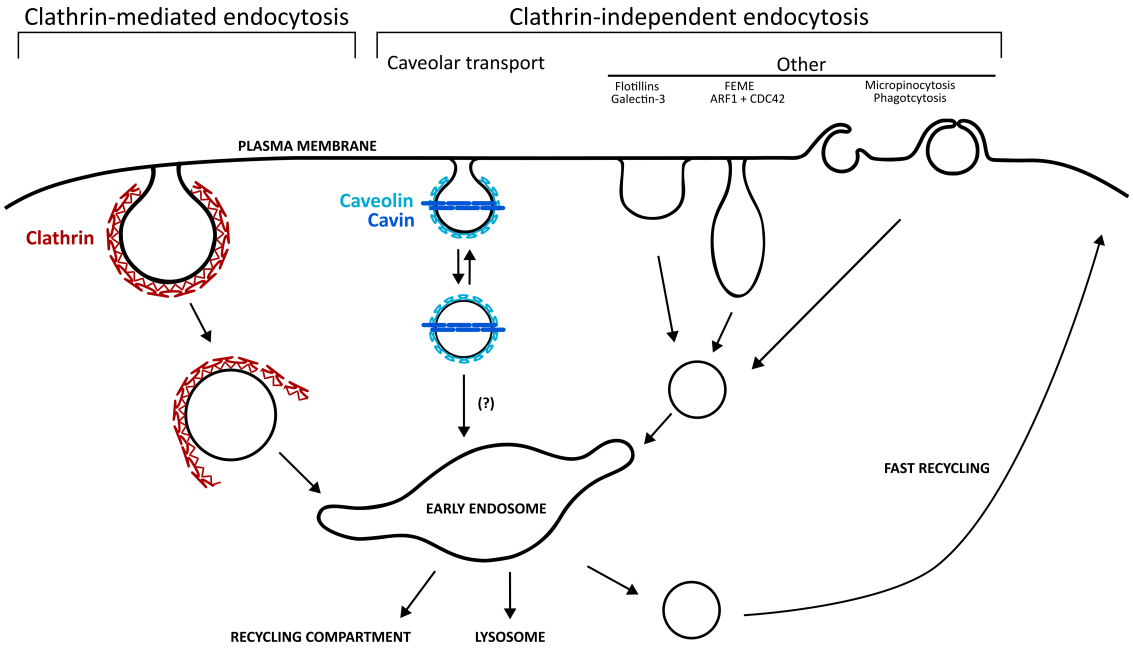

Figure 3. Endocytosis can be clathrin-mediated (CME) or clathrin-independent (CIE). Budding vesicles from the plasma membrane serve as the first event in endocytosis and it is common to all different pathways. The final destination of the cargo may differ depending on the cellular context. Some pathways are not yet fully understood.

1.2.1. Clathrin-mediated endocytosis

Clathrin-mediated endocytosis (CME) is the cellular process which utilizes clathrin-coated vesicles that originate from the plasma membrane for the uptake of material inside the cell (McMahon & Boucrot, 2011). This is a versatile pathway due to the diverse types of cargoes which can be packaged, as well as the wide range of accessory adaptor proteins that participate in it (McMahon & Boucrot, 2011). Notably, CME is a universal process employed by all eukaryotic cells (Thottacherry et al., 2019).

A complex and modular protein machinery can transiently cluster and assemble on the plasma membrane and shape it into clathrin-coated vesicles which contain the selected cargo (Kaksonen & Roux, 2018). This process can be divided in five stages (Figure 4). First, clathrin and clathrin-adaptor proteins, including the AP2 (heterotetrameric adaptor protein) complex, CALM (clathrin assembly lymphoid myeloid leukemia protein) and epsins, bind to the lipids at the plasma membrane and to cargo molecules. Scaffolding proteins such as clathrin itself, EPS15 (epidermal growth factor receptor substrate 15) and intersectins, convey the clustering and formation of the clathrin cage. These protein assemblies, together with on-site actin polymerization, promote membrane bending and the formation of vesicles. BAR domain proteins (endophilins and amphiphysins) and the large GTPase dynamin cooperate for the constriction and scission of the vesicle neck. The clathrin vesicle is therefore released from the plasma membrane and trafficked to its destination within the cell. Upon arrival, the clathrin coat disassembles allowing fusion with the target membrane (Kaksonen & Roux, 2018; McMahon & Boucrot, 2011).

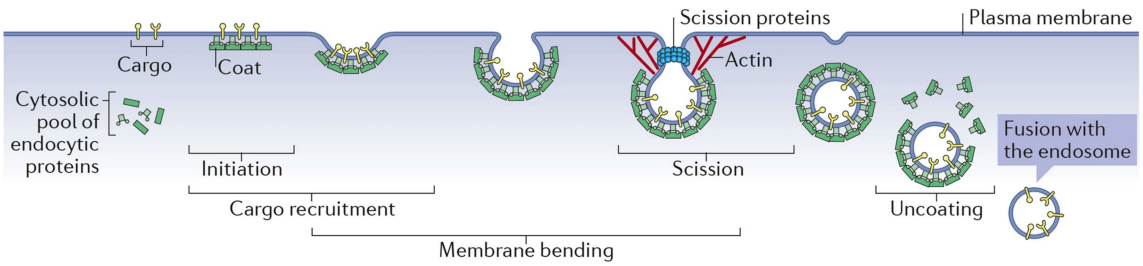

Figure 4. Clathrin-mediated endocytosis. There are five main steps in CME which involve a complex machinery of diverse proteins. Figure adapted from (Kaksonen & Roux, 2018).

1.2.2. Clathrin-independent endocytosis

Various mechanisms of clathrin-independent endocytosis (CIE) have been categorized based on the protein machineries which mediate the formation of plasma membrane invaginations and budding vesicles (Figure 3) (Sandvig et al., 2011). It is worth noting that the occurrence of one pathway or another is highly dependent on the cell-type and also on the context, for example specific cargo, lipid composition, cell polarization, cell density and signaling pathways (Sandvig et al., 2011).

According to recent developments in the field, clathrin-independent endocytosis routes can be divided into those which are dependent on dynamin and those which do not require dynamin for vesicle scission (Sandvig et al., 2018; Thottacherry et al., 2019). Dynamin-dependent mechanisms include: caveolar endocytosis, FEME (Fast Endophilin A-Mediated Endocytosis) and phagocytosis. Pathways in which dynamin is not involved feature endocytosis regulated by the small GTPases ARF1 (ADP-ribosylation factor 1) and CDC42, Flotillin-mediated endocytosis, Galectin-3-based budding mechanisms, micropinocytosis, and ARF6-dependent endocytosis.

Some of these pathways are not completely understood and some studies have provided conflicting results and conclusions. For example, it is not clear that the destination of caveolar cargo is the endosome, and caveolae have been seen as rather stable structures that do not account for a high internalization rate (Echarri & Del Pozo, 2015; Sandvig et al., 2018). Furthermore, although classically associated with dynamin, recent publications have contradicted this assumption and showed that dynamin-2 was absent from caveolae (Matthaeus et al., 2022), or that dynamin-2 could only be stably localized with the bulb of a subset of caveolae and was indeed not required for the fission of caveolae (Larsson et al., 2023).

Given the significance of caveolae in this thesis, the subsequent sections provide a more detailed introduction to these plasma membrane nanodomains.

1.3. Caveolae

Caveolae, plasma membrane invaginations with diameters ranging from 70 to 100 nm, exhibit a distinct bulb shape which protrudes into the cytosol (Figure 5). They are highly abundant in adipocytes, endothelial cells, muscle cells, fibroblasts and astrocytes, but are scarce in other cell types (Echarri & Del Pozo, 2015; Matthaeus & Taraska, 2021; Parton, Del Pozo, et al., 2020).

Rich in cholesterol, sphingomyelin, and ceramides, caveolae create unique lipid environments, acting as reservoirs in the plasma membrane for these molecules (Hubert et al., 2020; Parton, Kozlov, et al., 2020).

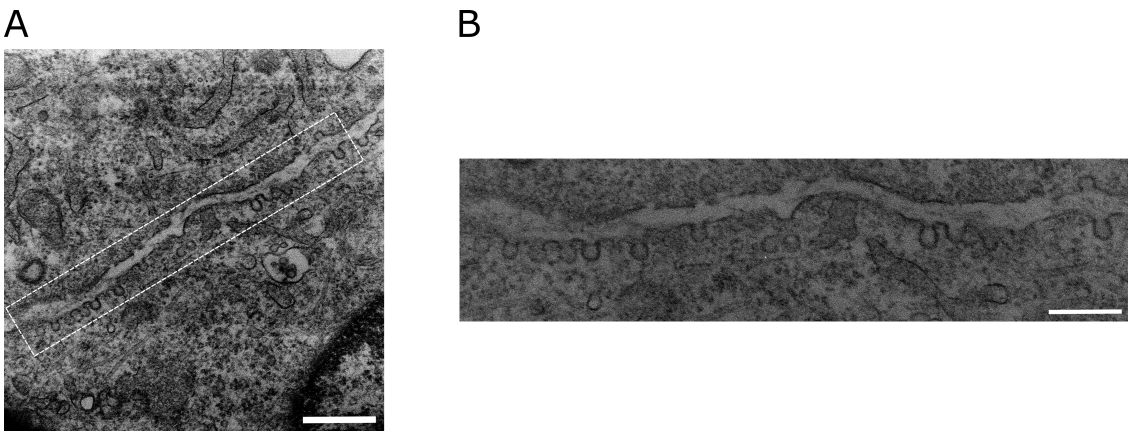

Figure 5. Caveolae. A) Electron micrograph of caveolae at the plasma membrane of mouse embryonic fibroblasts. B) Magnified view of the inlet highlighted in A. Scale bar: 500 nm.

1.3.1. Functions of caveolae

Two prominent cellular processes involving caveolae are mechanoprotection and control of lipid homeostasis (Matthaeus & Taraska, 2021; Parton, Del Pozo, et al., 2020; Parton, McMahon, et al., 2020; Sotodosos-Alonso et al., 2023).

Caveolae can rapidly respond to mechanical forces and reorganize their morphology accordingly. They can be found at the plasma membrane as singles pits (more or less bent (Matthaeus et al., 2022)) or they can form higher-order structures called rosettes, characterized by multiple caveolae connected to the plasma membrane through a single neck (Echarri & Del Pozo, 2015; Sotodosos-Alonso et al., 2023). In general, caveolae undergo flattening when subjected to increased membrane tension and they invaginate at low tension, thus providing a tension-buffering system (Echarri & Del Pozo, 2015). Moreover, caveolae play a role in sensing shear stress in endothelial cells where they can interact with the endothelial nitric oxide synthase (eNOS) to regulate the production of nitric oxide and, in consequence, modulate vascular tone (Matthaeus et al., 2019; Rizzo et al., 1998). Furthermore, caveolae contribute to the intricate communication between cells and the extracellular matrix (ECM) at focal adhesions, where caveolin-1 participates in integrin-dependent signaling (Echarri & Del Pozo, 2006).

The role of caveolae in lipid homeostasis is associated with their implication in clathrin-independent endocytosis and in transcytosis. Although, to date, no caveolae-specific cargo has been identified, studies have shown evidence for caveolae involvement in the conventional endocytic pathway, but also in the possible migration of caveolae to the endoplasmic reticulum and to lipid droplets. Also, it has been proposed that caveolae can return to the plasma membrane in polarized cells (Echarri & Del Pozo, 2015; Parton, Del Pozo, et al., 2020; Parton, Kozlov, et al., 2020). The idea that the intracellular fate of caveolae are lipid droplets has been gaining attention lately due to their potential role in regulating lipid metabolism (Hubert et al., 2020; Matthaeus & Taraska, 2021; Morén et al., 2019; Sotodosos-Alonso et al., 2023). For example, cholesterol distribution in the Golgi and at the plasma membrane is highly dependent on caveolin-1 expression and, in the absence of caveolin-1, cholesterol tends to accumulate in these compartments (and, in consequence, also in the ER and mitochondria), affecting proper cell functioning (Chaudhary et al., 2014; Hayer et al., 2010; Parton, Kozlov, et al., 2020). In fact, lipid accumulation within the caveolar membrane promoted caveolae detachment. This and other sources of enhanced caveolae mobility resulted in more abundant and larger lipid droplets, and in an increased fatty acid uptake (Matthaeus et al., 2020; Morén et al., 2019). One hypothesis is that caveolae may work as lipid sensors at the plasma membrane and respond to critical unbalances in the equilibrium of these molecules by detaching and being trafficked to lipid droplets. However, this transport mechanism and whether only caveolin-1 or whole vesicles are transferred to the lipid droplet is not completely understood (Hubert et al., 2020; Matthaeus et al., 2022; Morén et al., 2019; Sotodosos-Alonso et al., 2023).

Despite being important in numerous fundamental cellular processes, the deletion of caveolin-1 or Cavin1 is not lethal. Nevertheless, caveolin or cavin deficient mice suffer from impaired lipid metabolism and lipodystrophy, cardiomyopathies and muscular dystrophy (Matthaeus & Taraska, 2021).

1.3.2. Caveolar proteins

Caveolae form as a result of the co-assembly at the plasma membrane of two distinct sets of proteins: caveolins (three orthologous in humans, CAV1-3) and cavins (Cavin1-4) (Matthaeus & Taraska, 2021; Parton, McMahon, et al., 2020). Several studies have shown that Caveolin-1 oligomerizes while being transported through the secretory pathway and associates with cholesterol molecules (Fernandez et al., 2002; Hayer et al., 2010). Once at the plasma membrane, caveolin/cholesterol complexes can cluster phosphatidylserine and more cholesterol and form elongated invaginations by shaping and remodelling the membrane (Han et al., 2020; Porta et al.,

2022). However, caveolin alone cannot generate the typical bulb shape and it is believed that Cavin proteins are responsible for sculpting the omega (Ω)-like configuration (Matthaeus & Taraska, 2021; Parton, McMahon, et al., 2020). Cavins are recruited from the cytosol and oligomerize into trimers (homo- and hetero-oligomers). These assemblies can surround the caveolar membrane by forming a scaffolding coat which results in structured caveolae (Figure 5 and Figure 6) (Ludwig et al., 2016; Stoeber et al., 2016). Importantly, caveolae are tightly coupled to actin filaments, which play a role in their lateral movement and in internalization (Echarri & Del Pozo, 2015). Caveolins and cavins are essential for the formation of the special architecture of caveolae, however, other proteins play crucial roles for the appropriate function of these plasma membrane nanodomains (Matthaeus & Taraska, 2021; Parton, McMahon, et al., 2020). Figure 6 displays a schematic representation of the proteins which localize to caveolae.

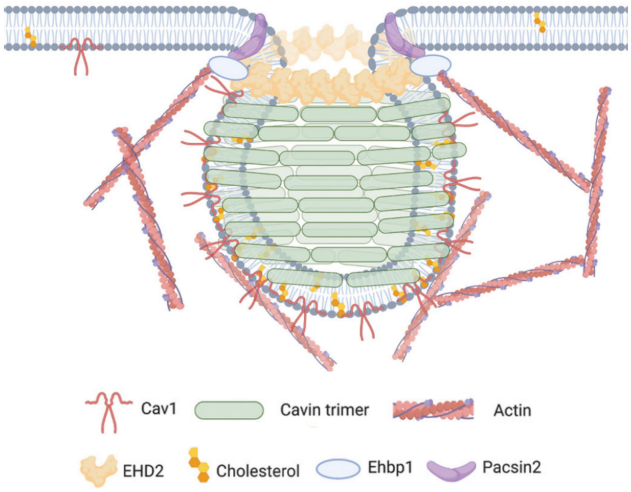

Figure 6. Several proteins are involved in the caveolar system. Illustration showing one caveola and its most relevant components. Figure modified from (Matthaeus & Taraska, 2021).

The F-BAR domain protein syndapin2, also known as Pacsin2, has been shown to be important for bending the membrane and for its stabilization (Hansen et al., 2011; Senju et al., 2011). The dynamin-related ATPase EHD2 is believed to oligomerize around the neck of caveolae and stabilize membrane curvature (Ludwig et al., 2013; Matthaeus et al., 2020; Morén et al., 2012). Moreover, the EHD2 binding partner EHBP1 can also associate with caveolae (Matthaeus et al., 2022). In an analogy to clathrin-coated vesicles, dynamin has been proposed to be important for the process of caveolae detachment from the plasma membrane (Oh et al., 2012; Senju et al.,

2011; Shajahan et al., 2004) and some studies could show co-localization of dynamin with CAV1 (Larsson et al., 2023; Matthaeus et al., 2020; Shajahan et al., 2004). However, a recent study failed to localize dynamin to caveolae across multiple experimental systems but could not exclude a role for dynamin in caveolae depending on specific cellular triggers or compensation mechanisms (Matthaeus et al., 2022). In fact, this study reported that caveolae are dynamic structures that undergo reversible curvature changes. The bending degree has a direct impact on the subset of proteins which are recruited: cavins and caveolins were found at all caveolae, independently of curvature degree, including flat caveolae; EHD2 localizes at both low and highly curved caveolae; Pacsin2 and EHBP1 only associate intermittently with lowly curved caveolae and highly curved caveolae, respectively (Matthaeus et al., 2022). All in all, these studies show the high degree of complexity that governs caveolar architecture. In addition, there are many open questions regarding the specific function of some of the implicated proteins, such as EHD2, EHBP1 and Pacsin2.

Also, structural information on these proteins is relatively scarce. Recently, the cryo-EM structure of detergent-solubilized full-length caveolin-1 was solved. The structure is composed by eleven subunits of caveolin-1 that assemble into a disc-like oligomer with a flat membrane-embedded surface. This study altered the classical model on how caveolins interact with the membrane and suggested that they induce membrane curvature in a unique way (Porta et al., 2022). A crystal structure of the minimal N-terminal domain HR1 of Cavin1 showed that this domain is required and sufficient for trimerization (Kovtun et al., 2014). Although the full-length structure of Pacsin1 is known (Rao et al., 2010), to date, only the dimeric F-BAR domain of Pacsin2 was solved by X-ray crystallography (Plomann et al., 2010). A crystal structure of the bMERB domain of EHBP1 in complex with Rab8 is available (Rai et al., 2020). The dimeric structure of full-length EHD2 was solved by X-ray crystallography, but questions about oligomerization and membrane interaction remained unanswered (Daumke et al., 2007). All the structures mentioned above are shown in Figure 7.

It is evident that more structural work is necessary for a complete understanding of the individual architecture and function of these proteins, ideally when present on caveolae. In addition, there is little information about how they interact with each other to form complexes that bind and remodel the membrane and establish networks with the actin cytoskeleton. To gain new insights into the structure of caveolar proteins, the work presented in this thesis focuses on the structure and function of the dynamin-related ATPase EHD2. The following sections provide a thorough introduction to EHD proteins, which belong to the dynamin family of proteins.

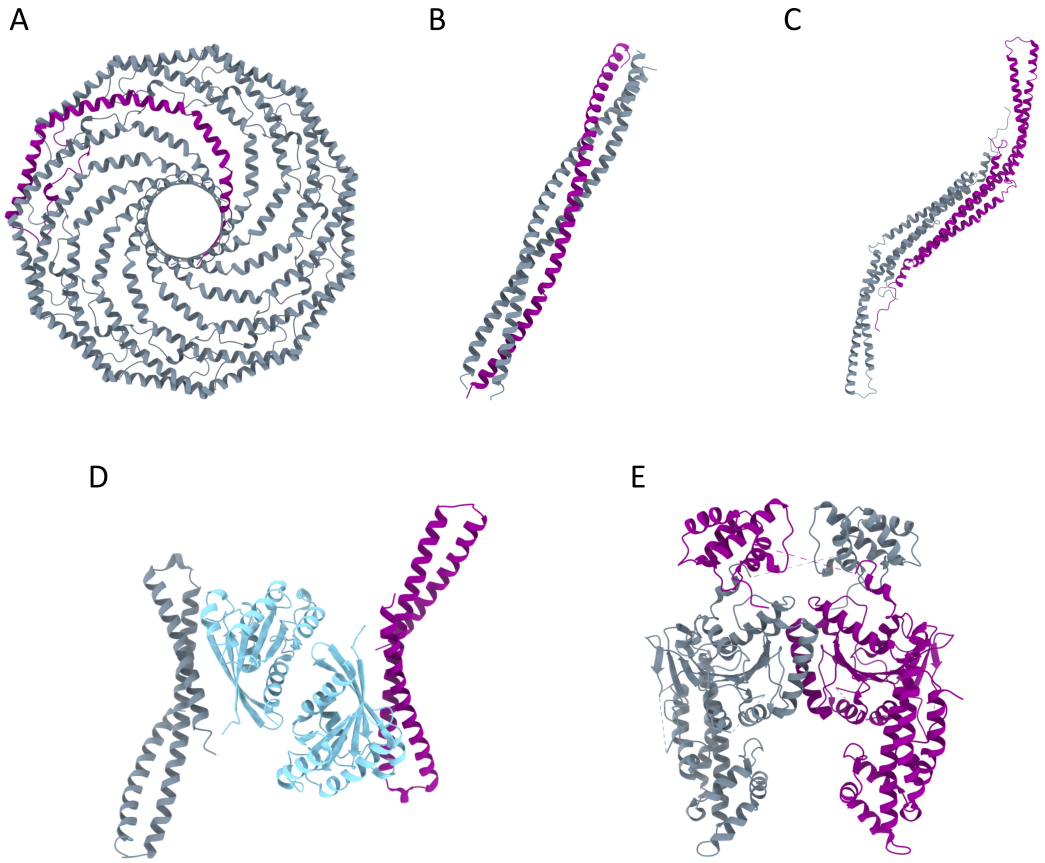

Figure 7. Available structures of caveolar proteins. A) Caveolin-1 forms disc-like oligomers of eleven subunits (PDB: 7SC0). B) The HR1 domain of Cavin1 is sufficient for trimerization (PDB: 4QKV). C) The F-BAR domain of Pacsin2 can dimerize (PDB: 3LLL). D) The bMERB domains of EHBP1 interact with Rab8 (light blue) (PDB: 6ZSI). E) The ATPase EHD2 is a dimer in solution (PDB: 2QPT). For each structure, one monomer is highlighted in purple, and the other monomers are shown in gray. Note that these structures are shown for illustrative purposes and are not accurately scaled.

1.4. The dynamin family of proteins

Proteins from the dynamin superfamily are multidomain mechano-chemical GTPases which are implicated in nucleotide-dependent membrane remodelling events. Considerably diverse proteins belong to this family since they share conserved structural elements: the amino-terminal G domain, which is followed by one or two helical domains, known as the bundle signaling element (BSE) and/or stalk domain (Faelber et al., 2013). At the C-terminus, dynamin-related proteins contain membrane-binding sites and/or protein-protein interaction domains (Figure 8).

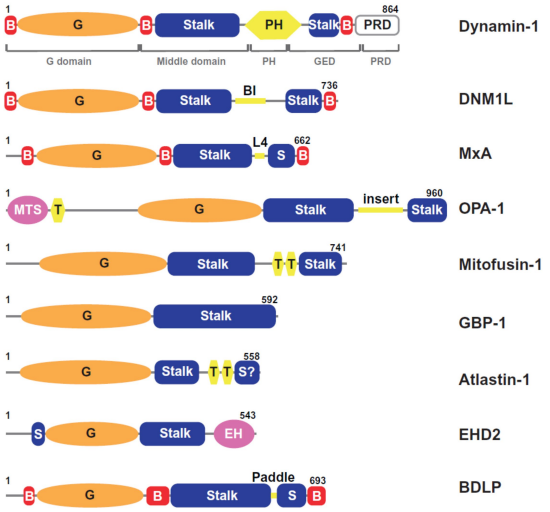

Figure 8. Domain architecture of dynamin and dynamin-related proteins. Structure-based domain architecture of dynamin superfamily members. G: GTPase domain, B: bundle signaling element, PH: pleckstrin homology domain; PRD: proline- and arginine-rich domain; T: transmembrane domain; BI: B-insert; L4: Loop 4; EH: Eps15-homology domain. Figure modified from (Faelber et al., 2013).

For dynamin, the pleckstrin homology (PH) domain mediates membrane binding, however, atlastin, mitofusins and BDLP have predicted transmembrane helices (Faelber et al., 2013). Others, such as MxA and DRP1 interact with membranes via a loop at the tip of the stalk. In the case of EHDs, membrane binding is mediated by ionic and hydrophobic interactions between residues within the stalk and the phospholipids of the membrane (Faelber et al., 2013). Furthermore, other domains and motifs present in these proteins are involved in specific functions to each member. For example, the proline- and arginine-rich domain (PRD) of dynamin is engaged in the recruitment to clathrin-coated vesicles since it can interact with Src-homology 3 (SH3) domains from Bin/Amphiphysin/Rvs (BAR)-domain containing proteins (Soulet et al., 2005). Another example is the EH domain of EHD proteins, which can bind to Asn-Pro-Phe (NPF) repeat motifs in binding partners (Naslavsky & Caplan, 2011).

1.4.1. Cellular functions

The membrane remodelling events in which dynamin and related proteins are involved include fusion and fission processed at a wide range of vesicles and organelles (Figure 9) (Daumke & Praefcke, 2016).

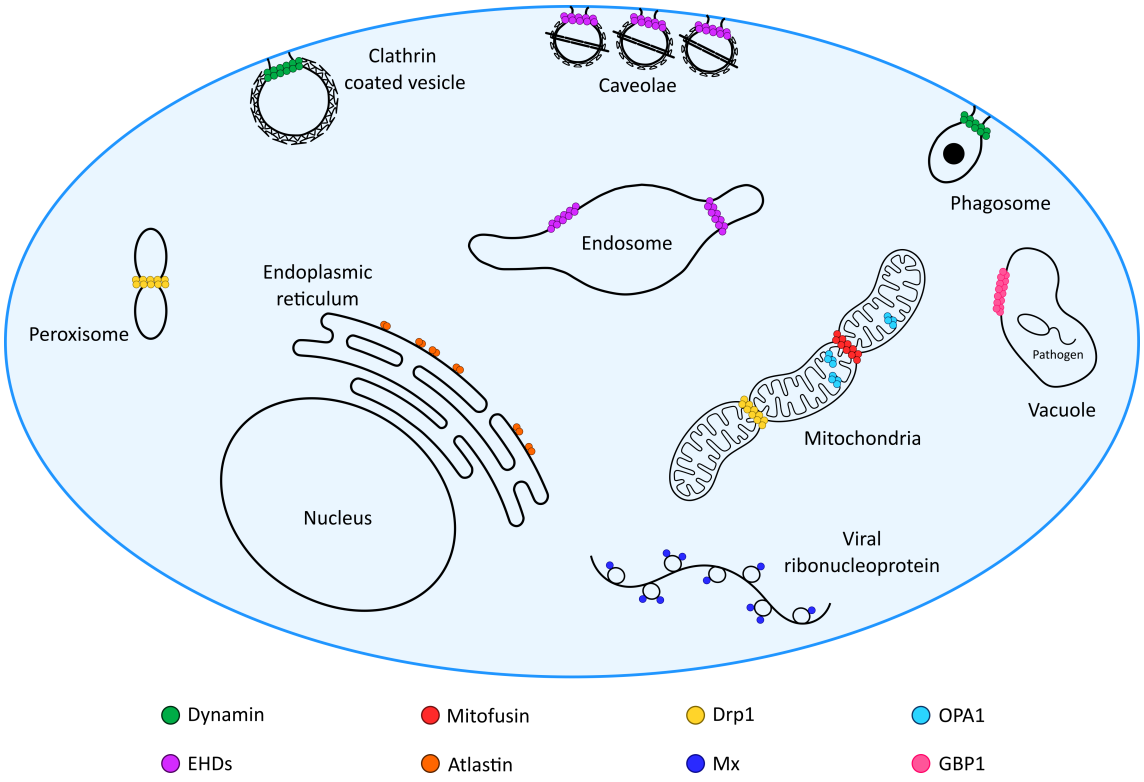

Figure 9. Members from the dynamin superfamily. Dynamin and dynamin related proteins are involved in membrane fusion and fission events in a wide variety of organelles and processes in the animal cell.

Classical dynamins are involved in the scission of clathrin-coated vesicles at the plasma membrane, the cleavage furrow, the Golgi and at endosomes, but they also mediate other clathrin-independent endocytic events at the plasma membrane (Praefcke & McMahon, 2004) (see Section 1.2). In animal cells, the other members of the family are required for organellar division and fusion (Praefcke & McMahon, 2004). Dynamin-related protein 1 (Drp1) mediates the division of peroxisomes and mitochondria (Mcbride & Frost, 2016). OPA1 (optic atrophy 1) and mitofusins are involved in the fusion of the inner and outer mitochondrial membranes, respectively (Cao et al., 2017; Raymond Liu & Chan, 2017). Myxovirus resistance proteins (Mx proteins) are induced by interferons and confer resistance against RNA viruses by interacting with viral ribonucleoproteins (Haller et al., 2010). Atlastin tethers and fuses endoplasmic reticulum (ER) tubules and localizes transiently to newly formed three-way junctions at the ER (Wang et al., 2016). GBP1 (guanylate binding protein 1) is recruited to pathogen-containing vacuoles during infection and it is supposed to restrict pathogenic growth and activate the inflammasome pathway (Meunier et al., 2014). Lastly, bacterial dynamin-like proteins (BDLPs) are suggested to facilitate membrane tethering and confer resistance against phage infection (Low et al., 2009). Plants contain many different dynamin proteins which are involved in similar events, such as scission of

clathrin-coated vesicles, the formation of the cell plate or chloroplast division (Praefcke & McMahon, 2004). The cellular functions of EHD proteins are introduced in Section 1.5.1.

1.4.2. Oligomerization mechanism

The stalk is the central assembly hub mediating oligomerization in members of the dynamin family (Chappie et al., 2010; Faelber et al., 2013, 2019; Reubold et al., 2005, 2015). In dynamin, two stalks assemble in a crisscross fashion via a highly conserved central interface (interface-2) to form stable dimers. One stalk dimer oligomerizes via two additional conserved interfaces (interfaces-1 and 3) with the neighboring stalk dimer (Chappie et al., 2010; Faelber et al., 2013, 2019; Reubold et al., 2005, 2015) (Figure 10).

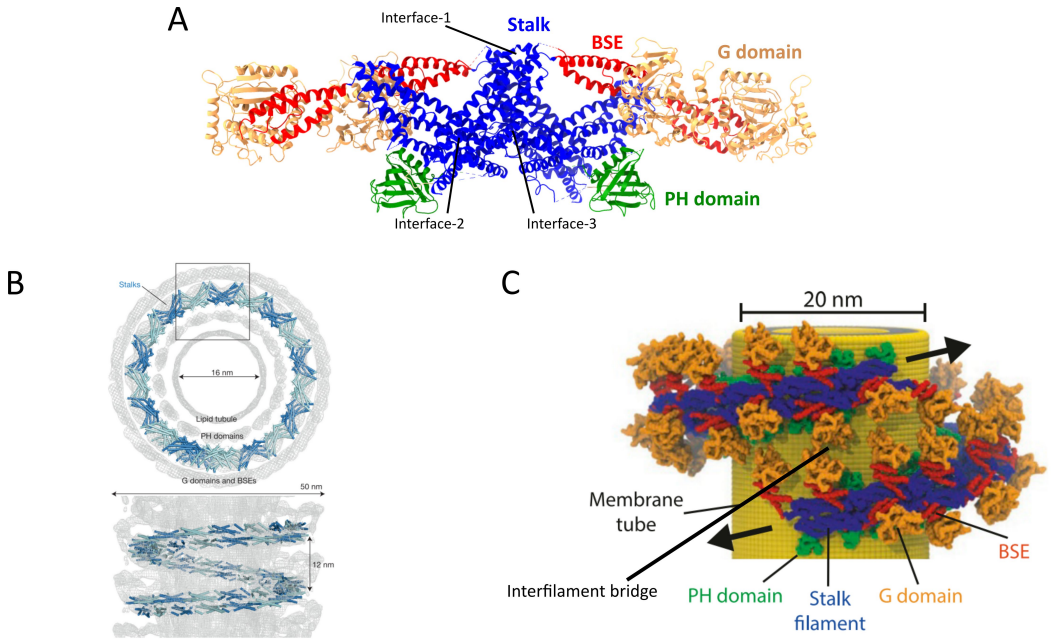

Figure 10. Dynamin oligomerization. A) Crystal structure of the human dynamin tetramer (PDB:5A3F). Three highly conserved interfaces involving the stalk domain drive oligomerization. B) Schematic representation of dynamin helical filaments around membranes. C) The G domains in dynamin form nucleotide-dependent cross-bridges between filaments. Panels B and C are modified from (Reubold et al., 2015) and (Ganichkin et al., 2021), respectively.

Oligomerized dynamin forms helical filaments of fixed pitch during active constriction of membranes (Ganichkin et al., 2021). Furthermore, the dynamin filament has the ability to form nucleotide-dependent cross-bridges between neighboring turns (Ganichkin et al., 2021). This means that the G domains are oriented to the outside of the filament so that they form inter-filament stabilizing interfaces (Kong et al., 2018; Jiwei Liu et al., 2021) (Figure 10).

1.4.3. GTP hydrolysis – the power stroke

Proteins of the dynamin family are considered as mechano-chemical enzymes because they use the energy of GTP hydrolysis to remodel membranes (Daumke & Praefcke, 2016). For all GTPases, efficient hydrolysis requires: 1) the correct positioning of a water molecules for a nucleophilic attack on the γ-phosphate, 2) neutralization of a negative charge that develops between the β- and γ-phosphates in the transition state, and 3) stabilization of the conformationally flexible switch regions within the catalytic core (Chappie et al., 2010). These conditions are achieved either through interaction with a GTPase-activating protein (GAP), in the case of Ras-like GTPases, or through dimerization, in the case of dynamin and dynamin-related proteins (Chappie et al., 2010).

In dynamin proteins, nucleotide hydrolysis has been shown to generate a mechanical movement of the helical domain. In the case of dynamin, the crystal structure of the non-hydrolysable GTP analog GMPPCP-bound form corresponds to the open conformation of the bundle signal element (BSE) (Chappie et al., 2011). However, when dynamin is in the apo state or bound to the transition state mimic GDP-AlF4 or to GDP, the BSE adopts a closed conformation (Chappie et al., 2011; Daumke & Praefcke, 2016; Faelber et al., 2011). During this transition, the BSE rotates 70º around the hinge region between this domain and the GTPase domain (Figure 11, panel A). This movement acts as a power stroke and is thought to trigger relative sliding of the helical filament around the membrane, leading to constriction and fission (Figure 11, panel B) (Antonny et al., 2016; Chappie et al., 2011; Faelber et al., 2011, 2019; Ganichkin et al., 2021).

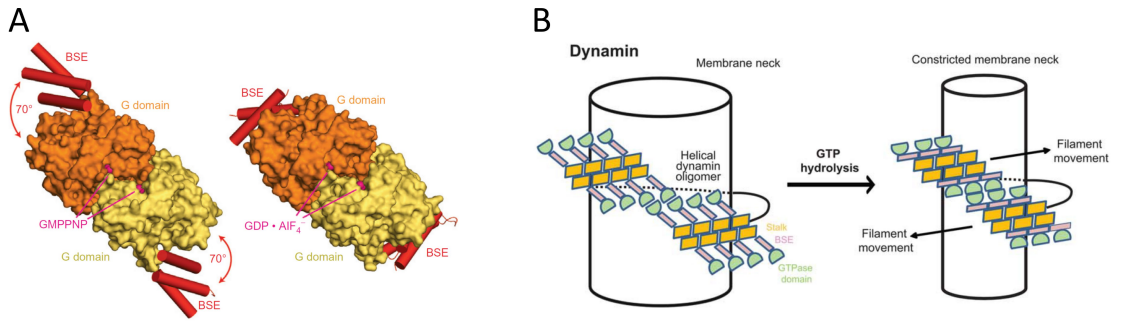

Figure 11. GTP hydrolysis is translated into a power stroke necessary for membrane remodelling. A) Comparison between GMPPNP- and GDP-AlF_4^--bound structures of a G domain-minimal BSE construct (PDB: 3ZYC and 2X2E, respectively). Dynamin undergoes a structural rearrangement of the BSE upon GTP hydrolysis. Figure modified from (Faelber et al., 2013). B) Schematic representation of the GTP hydrolysis-dependent constriction action of dynamin. Figure modified from (Daumke & Praefcke, 2016).

Recently, the crystal and cryo-ET structures of fungal Mgm1 (OPA1 in animals) were solved and it was proposed that these proteins might undergo a similar power stroke (Faelber et al., 2019). Nevertheless, these large structural rearrangements are induced by nucleotide and or lipid binding and vary among the different members of the family (Daumke & Praefcke, 2016). Some prominent examples are shown in Figure 12.

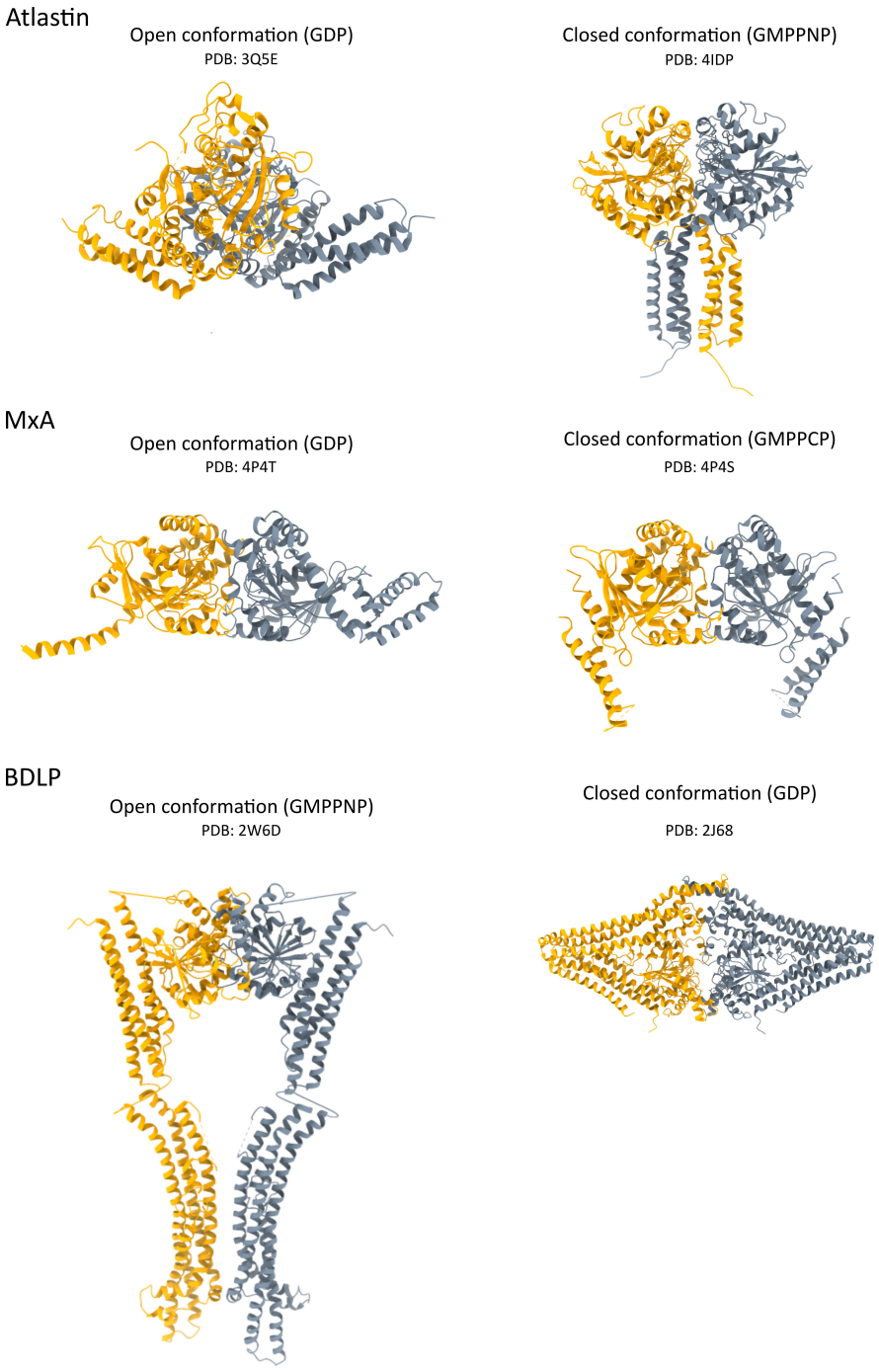

Figure 12. Open and closed conformations of some members of the dynamin family of proteins. Conformational rearrangements are induced by GTP hydrolysis and/or the recruitment to membranes.

1.4.4. Membrane remodelling

Previous sections have already briefly introduced that dynamin and dynamin-related proteins oligomerize via their stalk domain by forming different interfaces that generate a helical filament on the surface of lipid bilayers *in vitro*. As also stated above, in the cell, they carry out membrane remodelling activities, such as fusion or fission, in a nucleotide hydrolysis-dependent manner. It is worth noting that different proteins convey fundamentally different activities. The dynamin filament constricts the underlying membrane until it generates a fission intermediate. Later the insertion of hydrophobic residues from the membrane binding domain complete scission (Daumke & Praefcke, 2016; Ganichkin et al., 2021; Kong et al., 2018; Jiwei Liu et al., 2021). Similar fission mechanisms may also apply for MxA (Haller et al., 2010; Von Der Malsburg et al., 2011) or Drp1/DNM1L (Fröhlich et al., 2013; Ingerman et al., 2005). Two examples of membrane fusion in the dynamin family of proteins are atlastins and the bacterial BDLP. Atlastin has been proposed to promote tethering at opposing ER tubules by pulling membranes towards each other (Byrnes et al., 2013; Byrnes & Sondermann, 2011; Wang et al., 2016). Membrane fusion may be facilitated by the transmembrane regions and the C-terminal amphipathic helix (Tina Y. Liu et al., 2015). BDLP forms highly curved membrane tubules, probably by insertion of the paddle region. These tubules have been suggested to undergo membrane fusion upon conformational rearrangements that lead to dissociation of the protein coat (Low et al., 2009). Recently, Mgm1 (OPA1 in animals) was shown to remodel liposomes into membrane tubules where it was found to form helical filaments both in the outside (positive membrane curvature) and in the inside (negative membrane curvature) (Faelber et al., 2019). When assembled on the outside, Mgm1 forms left-handed helices that would expand the diameter of the tubule. Conversely, in the inside, Mgm1 forms right-handed helices that would result in constriction (Faelber et al., 2019). These different geometries might explain how Mgm1 can drive inner-membrane fusion, scission or stabilization of cristae (Faelber et al., 2019).

1.5. The EHD family of proteins

Eps15-homology domain-containing proteins (EHDs) comprise a highly conserved (see Appendix E) family of mechano-chemical ATPases which are involved in the regulation of different membrane trafficking pathways (Naslavsky & Caplan, 2011). EHDs are exclusive to eukaryotes; there are four members in mammalians (EHD1-4) and one in *C. elegans, D.*

melanogaster, A. thaliana and in some parasites from the genera *Trypanosoma, Plasmodium* and *Toxoplasma* (Naslavsky & Caplan, 2011). EHDs oligomerize into helical or ring-like structures upon recruitment to membranes, where they are believed to stabilize membrane curvature (Daumke et al., 2007; Melo et al., 2022).

1.5.1. Cellular functions

EHD proteins have been associated with diverse cellular processes that require remodelling and/or preservation of specific membrane shapes, mainly: endocytic recycling, caveolae biogenesis, ciliogenesis, formation of T-tubules in skeletal muscles and membrane resealing after rupture (Figure 13) (Bhattacharyya & Pucadyil, 2020). The initial findings that allowed linking EHD proteins to endocytic pathways were rooted in the investigation of the *C. elegans* EHD1 ortholog RME-1. This protein was found to associate with endocytic organelles and defects in recycling pathways arose in RME-1 mutants (Grant et al., 2001). In the last twenty years, many authors have contributed to a better understanding of the cellular functions of EHDs. The most notable ones are briefly summarized, according to site or pathway, in the following.

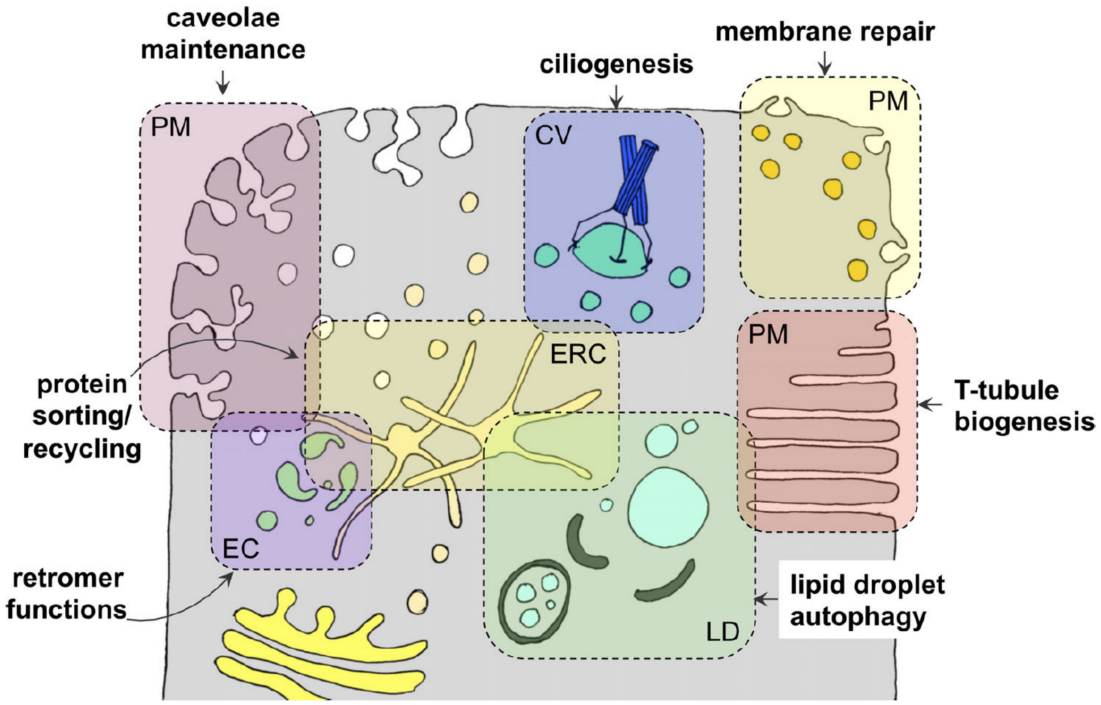

Figure 13. Schematic representation of the sites and pathways where EHDs play a role. The four mammalian paralogs are implicated in functions which require membrane remodelling and/or maintenance. Main functions have been described in endocytic recycling and sorting, caveolae biogenesis and consequent lipid homeostasis, ciliogenesis, membrane repair and T-tubule formation in muscle cells. Figure from (Bhattacharyya & Pucadyil, 2020).

With regard to endocytosis, many studies show the involvement of EHD1 in endocytic recycling (Bhattacharyya & Pucadyil, 2020). EHD1 has been localized to vesicular and tubular structures in the perinuclear area that partially coincide with markers of the endocytic recycling compartment (ERC), such as Rab8, Rab11 and MICAL-L1 (Grant & Caplan, 2008; Naslavsky & Caplan, 2011; Pant et al., 2009; Sharma et al., 2010; Zhang et al., 2012). Mutations or a deletion of EHD1 result in a delayed recycling of multiple receptors (Rapaport et al., 2006), (Lin et al., 2001). Therefore, some studies suggest that EHD1 could regulate receptor sorting and/or release of vesicles from the ERC (Lee et al., 2015; Rapaport et al., 2006). Others observed that loss of EHD1 results in the confinement of proteins in tubular compartments (Cai et al., 2012), and that the addition of EHD1 induces the transformation of vesicles into tubules, followed by fission of these tubular structures (Cai et al., 2013). More recently, it was shown that EHD1 forms scaffolds on membrane tubes and catalyzes their fission (Deo et al., 2018). These findings support the idea that EHD1 could be involved in regulating vesicle fission and release (Bhattacharyya & Pucadyil, 2020). Furthermore, EHD3 was shown to be involved in the regulation of retrograde trafficking to the Golgi (Naslavsky et al., 2009) and it has been suggested that EHD4 functions at early endosomes regulating recycling from them (Sharma et al., 2008).

EHD proteins have been associated with various aspects of muscle development and muscle tissue specialization (Bhattacharyya & Pucadyil, 2020). Muscle maturation involves myoblast fusion to create syncytial myotubes, crucial for skeletal muscle development and regeneration in adulthood (Bhattacharyya & Pucadyil, 2020). Myoferlin is a membrane protein present at myoblast and myotube fusion sites and is essential for muscle regeneration (Katherine R. Doherty et al., 2005). EHD2 was shown to interact with myoferlin and facilitate its delivery to the cell surface (Katherine R. Doherty et al., 2008). In addition, EHD2 was also found accumulating at sites of injury in human myotubes being involved in the membrane repair process (Marg et al., 2012). Also, in skeletal muscle, EHD1 is localized to T-tubules, which are deep plasma membrane invaginations that are connected to the endoplasmic reticulum, and defects in its ATPase activity lead to an excessive number of T-tubules (Demonbreun et al., 2015). EHD3 appears to be crucial for the structural and functional specialization of membrane tubules in cardiomyocytes (Gudmundsson et al., 2012).

Primary cilia are crucial organelles that regulate various signaling pathways. Defects in ciliogenesis are associated with human diseases termed ciliopathies (Bhattacharyya & Pucadyil, 2020). EHDs are involved in intracellular ciliogenesis. This mechanism relies on the formation of the distal appendage vesicles (DAVs) and the ciliary vesicle (CV), which fuses with the plasma membrane to expose the cilia (Bhattacharyya & Pucadyil, 2020). EHD1 knock-out is lethal at the embryonic stage in mice due to ciliogenesis defects (Bhattacharyya et al., 2016). Depending on the tissue, EHD1 and/or EHD3 are recruited to DAVs during early steps of ciliogenesis where

they might be involved in recruiting the SNARE protein SNAP29, which mediated fusion of DAVs to form the CV (Lu et al., 2015). Furthermore, previously described binding partners of EHDs MICAL-L1 and Pacsins 1 and 2 are also required in early steps of ciliogenesis (Insinna et al., 2019; Xie et al., 2018).

Caveolae have already been introduced in detail in Section 1.3. Several studies have shown that EHD2 localizes these plasma membrane invaginations, more specifically to their neck (Daumke et al., 2007; Ludwig et al., 2013, 2016; Matthaeus et al., 2022; Stoeber et al., 2012). There, EHD2 has been proposed to play an important role in the stabilization of membrane curvature, by oligomerizing around the neck and restricting lateral diffusion and detachment (Hubert et al., 2020; Matthaeus et al., 2020; Morén et al., 2012, 2019). Mutations in EHD2 that decrease membrane binding, impede oligomerization or affect nucleotide binding and hydrolysis, result in abnormal caveolae morphology (Daumke et al., 2007; Hoernke et al., 2017; Morén et al., 2012; Shah et al., 2014). A deletion of EHD2 results in increased caveolae mobility which leads to enlarged and more abundant lipid droplets, deposits of white fat around organs and bigger adipocytes (Matthaeus et al., 2020). Therefore, EHD2 is proposed to be a critical component for maintaining caveolae integrity and, consequently, to be a key regulatory player in lipid homeostasis (Hubert et al., 2020; Matthaeus et al., 2020). Interestingly, one study has shown that EHD1 and EHD4 are recruited to caveolae in the absence of EHD2, suggesting that they can act in compensation mechanisms (Yeow et al., 2017).

Notwithstanding, these proposed cellular functions have yet to be fully understood in accordance with the biochemical and intrinsic properties of EHD proteins (Bhattacharyya & Pucadyil, 2020).

1.5.2. Domain architecture of EHD proteins

The first structure of an EHD protein was that of mouse EHD2 bound to the non-hydrolysable ATP analog AMPPNP. This crystal structure revealed that EHD2 is a dimer in solution and that each monomer is composed of a G domain, a helical domain and an EH domain (Figure 14) (Daumke et al., 2007). Although present in the crystallized construct, residues 1-18 could not be solved due to lack of electron density. However, because of the relevance of the N-terminus in EHD proteins (see Section 1.5.2.3) and in this thesis, it is highlighted in Figure 14.

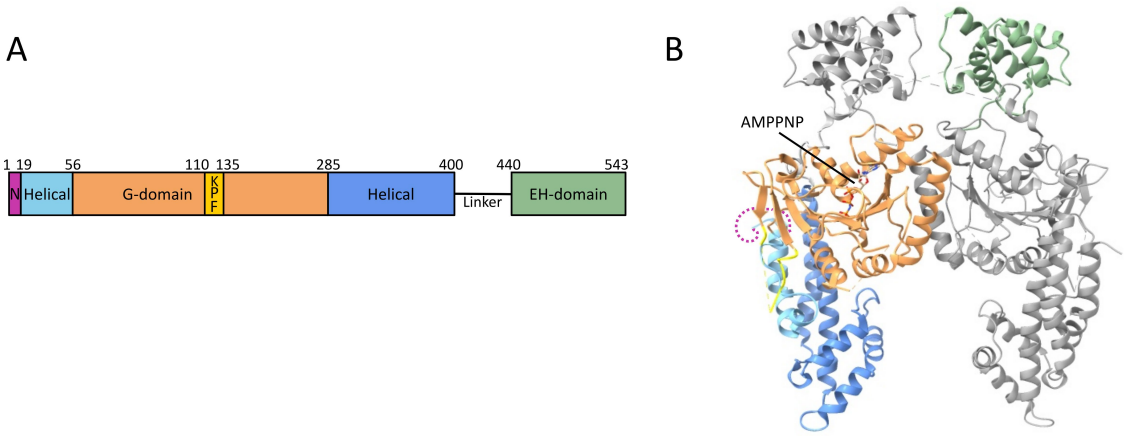

Figure 14. Domain architecture of EHD proteins and crystal structure of mouse EHD2. A) Schematic representation of the domains present in EHD proteins. The numbering corresponds to mouse EHD2 residues. B) Crystal structure of mouse EHD2 bound to AMPPNP (PDB: 2QPT, (Daumke et al., 2007)). One monomer is colored according to A, and the other one is shown in gray. Although unsolved, the N-terminal residues (1-18) are highlighted in magenta; the structure and position of these residues is unknown in this structure.

1.5.2.1. The G domain

The G domain is the most highly conserved domain in members of the dynamin superfamily. Eight β-strands form the central β-sheet, which is surrounded by seven α-helices and two single-turn helices (Daumke et al., 2007; Reubold et al., 2005). Five highly conserved motifs (G1-G5), including the phosphate binding loop (P-loop) and switch I and II, participate in nucleotide binding and hydrolysis (Daumke et al., 2007). The G1 motif tightly binds to the β-phosphate and contributes to the coordination of a Mg^{2+} ion crucial for nucleotide hydrolysis. Binding of magnesium is as well mediated by conserved residues of the G2 and G3 motifs. These two motifs contact the γ-phosphate and localize to the switch I and switch II regions, respectively (Daumke et al., 2007; Daumke & Praefcke, 2016). The switch regions undergo conformational changes upon nucleotide binding and hydrolysis. In other dynamins, an aspartate residue in the G4 motif is responsible for binding the guanine base of GTP (Daumke & Praefcke, 2016). However, the G domain in EHD proteins binds ATP since: 1) the conserved aspartate in G4 (D222 in EHD2) forms a hydrogen bond with an arginine residue (R536 in EHD2) located in the C-terminal tail of the EH domain, and 2) the amino group of the guanine cannot be accommodated in the nucleotide binding pocket because a methionine (M223 in EHD2), which directly follows the G4 motif, would sterically restrict this interaction (Daumke et al., 2007). At the distal side of the G domain, a unique and highly conserved motif, the KPF loop (residues 110-135 in EHD2), was shown to undergo conformational rearrangements depending on the opening state of the protein and to play

a role in oligomerization (Hoernke et al., 2017; Melo et al., 2017, 2022; Morén et al., 2012) (see Section 1.5.2.3). Some of the aforementioned structural details can be observed in Figure 14 and in Figure 15. Moreover, the G domain in EHD proteins contains a unique dimerization interface and it plays an essential role in oligomerization. For more details about dimerization and oligomerization in EHD proteins see Section 1.5.3.

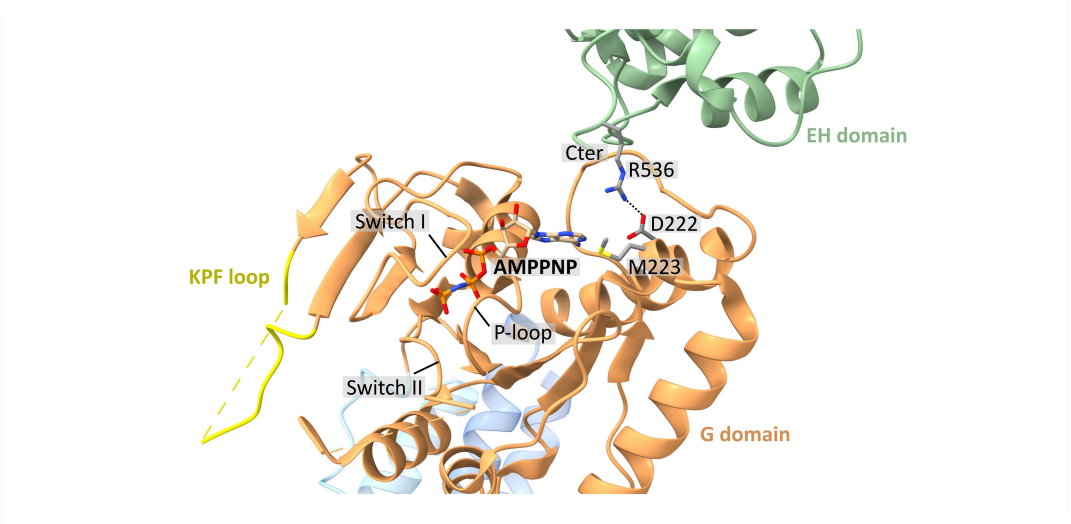

Figure 15. Nucleotide binding pocket of EHD2. The G domain in EHD proteins is highly conserved and includes the G1-4 motifs. Important elements in nucleotide binding, like the P-loop and the switch regions I and II are indicated. Despite being conserved, the G domain in EHD proteins binds ATP (and its analogs) because of several structural differences in comparison to other GTPases. In EHD2, Met223 sterically prevents the accommodation of a guanine, and D222 (recognizes the guanosine in other GTPases) forms a hydrogen bond with R536 in the EH domain.

1.5.2.2. The helical and EH domains

The helical domain is composed of two α-helices from the N-terminal region (residues 18-55 in EHD2) and five α-helices following the G domain (residues 285-400 in EHD2) (Figure 14, panel A). This domain mediates membrane binding via hydrophobic and positively charged residues at the tip of helices α9 and α11 (Figure 16, panel A) (Daumke et al., 2007; Shah et al., 2014). It also forms extensive contacts with the G domain, and it drives oligomerization by providing multiple assembly interfaces (Daumke et al., 2007; Melo et al., 2017, 2022). For more details about oligomerization in EHD proteins see Section 1.5.3.2.

Following the helical domain, a 40-residue linker connects with the C-terminal EH domain (residues 440-543 in EHD2) (Figure 14, panel A). It comprises two perpendicular EF hands

(helix-loop-helix motifs) which are connected by a short β-strand (Figure 16, panel B) (Daumke et al., 2007). The EH domain is localized on top of the G domain and binds to a GPF motif present in the flexible linker (Figure 16, panel B) (Daumke et al., 2007). EH domains have been typically assigned to opposing monomers in the two EHD2 crystal structures (Figure 14, panel B) (Daumke et al., 2007; Shah et al., 2014), but to the monomer directly below in the cryo-ET EHD4ΔN structure (Melo et al., 2022). It has been proposed that the EH domains could act as autoinhibitory modules by sterically blocking G domain mediated oligomerization (Daumke et al., 2007).

Additionally, the EH domain could mediate the interaction of EHD proteins with their binding partners. It has been suggested that, upon conformational rearrangements, the EH domain could be repositioned to make contacts with NPF motif-containing proteins (Daumke et al., 2007; Kieken et al., 2007; Melo et al., 2022; Naslavsky & Caplan, 2011; Shah et al., 2014). Some examples are interactions with proteins involved in endosomal trafficking such as Rabenosyn-5 (Naslavsky et al., 2004), MICAL-L1 (Pant et al., 2009) and Pacsin1 and Pacsin2 (Giridharan et al., 2013; Sharma et al., 2010), among others, and caveolar proteins like Pacsin2 (Morén et al., 2012; Senju et al., 2011) and EHBP1 (Guilherme et al., 2004), in the case of EHD2.

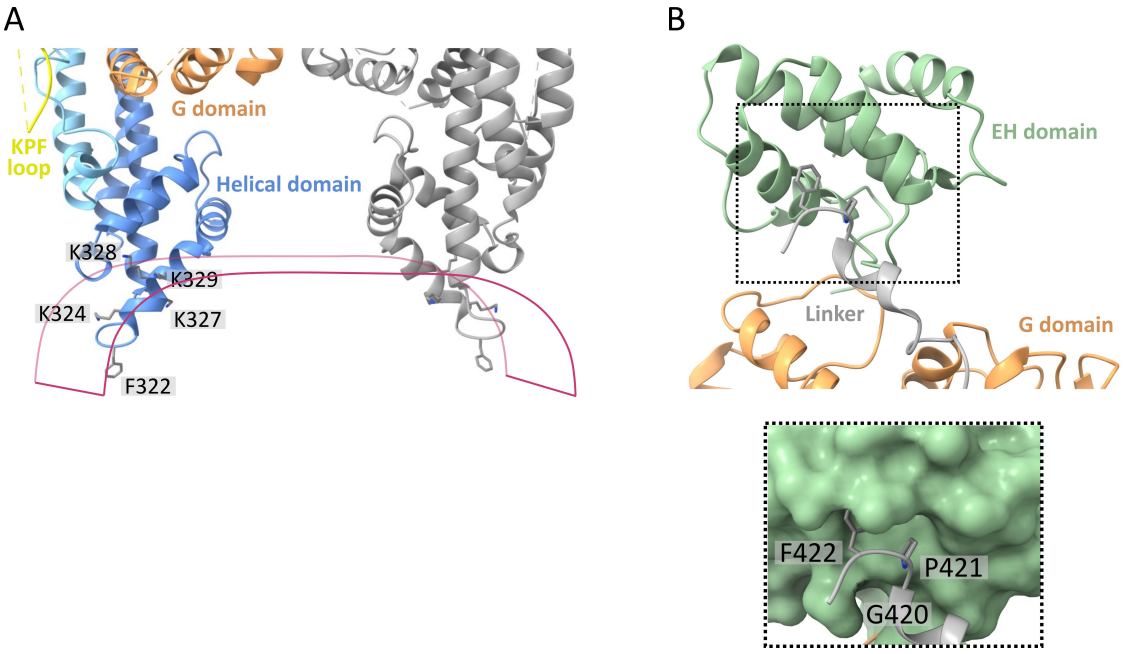

Figure 16. The helical and the EH domains. A) Positively charged and hydrophobic residues at the tip of the helical domain mediate membrane binding. The numbers of the indicated residues correspond to mouse EHD2. The lipid bilayer is represented by the magenta lines. One monomer is colored according to Figure 14, A, the other one is shown in gray. B) Top panel: the EH domain and part of the linker that connects it to the helical domain (not shown). The EH domain sits on top of a G domain and interacts with the GPF motif present in the linker (residue numbers correspond to mouse EHD2). Bottom panel: inlet highlighted on the top panel showing the binding groove of the EH domain.

1.5.2.3. The N-terminus

The N-terminal stretch of EHD2 has been defined as the short sequence comprising residues 1-18 (Figure 14, panel A, and Figure 17, panel A). These residues are highly conserved (Figure 17, panel A) and have been proposed to have a regulatory role in previous studies (Hoernke et al., 2017; Melo et al., 2017; Shah et al., 2014). It is known that the N-terminus folds back into a conserved hydrophobic pocket of the G domain (Figure 17, panel B) (Hoernke et al., 2017; Melo et al., 2017; Shah et al., 2014). Current models suggest that, upon recruitment to membranes, the N-terminal residues are displaced from this pocket, which becomes occupied by the peripheric KPF loop from the G domain (Figure 17, panels C and D). In turn, the N stretch could interact with the lipid bilayer and mediate membrane binding since EPR experiments showed that it can insert into liposomes (Hoernke et al., 2017; Melo et al., 2017; Shah et al., 2014). Furthermore, Shah and colleagues demonstrated an increased localization of N-terminally truncated EHD2 to caveolae in cells. Crystallographic studies using an EHD4 construct lacking the N-terminus (EHD4ΔN) presented an open conformation of the protein (Figure 17, panel C) and suggested that the absence of these residues had driven such conformational rearrangements (Melo et al., 2017). Moreover, as it had been shown for EHD2, the deletion of the N-terminal stretch of EHD4 resulted in increased membrane association in cells (Melo et al., 2017). At the same time, using biochemical and spectroscopy-based techniques, another study showed similar results for EHD2 concerning its domain reorganization upon membrane binding (Hoernke et al., 2017). Together, these studies paved the way to propose a model in which EHDs exist in two states: a closed one, represented by the two AMPPNP-bound EHD2 crystal structures (PDB: 2QPT and 4CID) (Figure 14, panel B and Figure 17, panel B, respectively) and an opened one, represented by the ATPγS- and ADP-bound EHD4ΔN structures (PDB: 5MVF and 5MTV) (Figure 17, panel C) (Hoernke et al., 2017; Melo et al., 2017).

In an effort to further understand mechanistic aspects about EHDs, a recently published cryo-ET structure of membrane-bound EHD4ΔN confirmed that in the oligomerized structure, the G domain is close towards the membrane so that the N-terminus can exit its hydrophobic pocket, allowing the KPF loop to enter it (Figure 17, panel D) (Melo et al., 2022). Consequently, the N-terminus could be free to insert into the membrane bilayer as proposed previously.

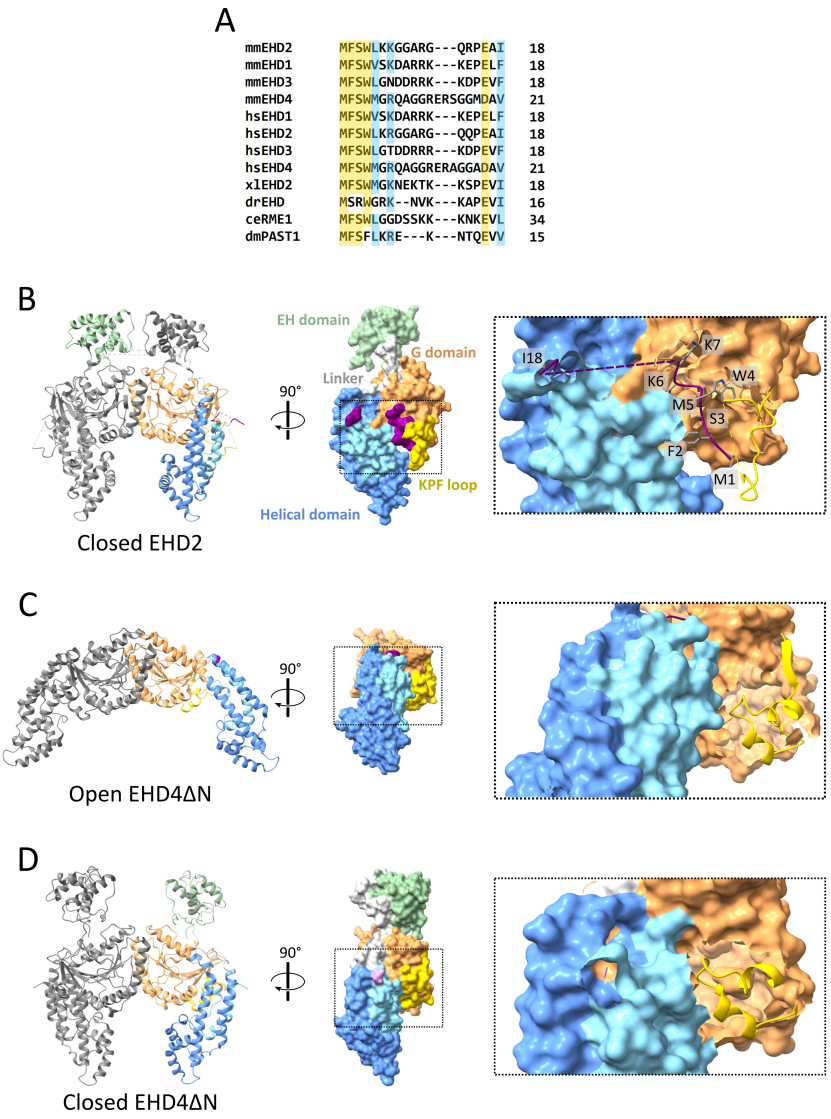

Figure 17. The N-terminal stretch of EHDs. A) Multiple sequence alignment of the N-terminal residues of several EHD proteins. The first 18 residues of mouse EHD2 were used as a reference. Identical and highly conserved residues are highlighted in yellow, residues with similar properties are highlighted in blue. mm: *Mus musculus*, hs: *Homo sapiens*, xl: *Xenopus laevis*, dr: *Danio rerio*, ce: *Caenorhabditis elegans*, dm: *Drosophila melanogaster*. B, C and D show three different EHD structures. The left panels correspond to the dimeric structures, where one monomer is colored according to the domain architecture of mouse EHD2 (Figure 14, A) and the other one is shown in gray. A side view (rotation of 90°) in a surface representation can be observed in the middle panels. On the right, a magnified view of the inlets indicated in the middle panels shows the hydrophobic pocket of the G domain, the KPF loop (in cartoons), and the N-terminal residues (in cartoons, if included in the structure). B) The crystal structure of mouse EHD2 structure is in the closed conformation (PDB: 4CID, (Shah et al., 2014)). The first eight residues of the N-terminus were solved and occupy the hydrophobic pocket of the G domain. Residues which could not be modeled are indicated by dashed lines. B) The crystal structure of N-terminally truncated mouse EHD4 is in the open conformation (PDB: 5MTV, (Melo et al., 2017)). The hydrophobic pocket of the G domain is occupied by the KPF loop. Residues 20 and 21 from the N-terminus were included in the model and are highlighted in magenta. The magnified view in the right panel is slightly rotated (130° with respect to the dimerization axis, left panel) for better visualization. C) The cryo-ET structure of N-terminally truncated and membrane-bound mouse EHD4 is in the closed conformation (PDB: 7SOX, (Melo et al., 2022)). The hydrophobic pocket of the G domain is occupied by the KPF loop. The first residue of the second stretch of the helical domain (Q22) is highlighted in pink to show where the N-terminus would end.

This study also revealed that, when bound to the membrane, oligomeric EHD4ΔN is in the closed state (Figure 17, panel D) (Melo et al., 2022). Melo and colleagues proposed the following model: EHDs are in the open state in solution and in the closed state when oligomerized and bound to membranes (for more details about the oligomerization mechanism see Section 1.5.3.2). Nevertheless, this work was not conclusive about the exact role of the N-terminus in EHD proteins since full-length EHD4 could not be expressed for comparison and, consequently, the effect of the truncation could not be fully assessed.

Furthermore, a study carried out using EHD1 also pointed out the relevance of the N-terminal residues. A deletion of residues 2 – 9 of EHD1 resulted in a significant defect in endocytic recycling and the typical EHD1 membrane bulging was less prominent (Deo et al., 2018). In accordance with the EHD2 and EHD4 studies, Deo and colleagues speculated that N-terminally truncated EHD1 scaffolds are unstable and that sustained self-assembly is not promoted.

All in all, these investigations show the importance of the N-terminal residues in the domain arrangement of EHDs, in the interaction with the membrane and in the oligomerization mechanism. These aspects are further introduced in the following sections.

1.5.3. Dimerization and oligomerization

1.5.3.1. Dimerization in EHDs and in the dynamin family of proteins

The G domain in EHDs contains a unique dimerization interface that is different from the canonical G-interface that drives dimerization in other GTPases (Daumke et al., 2007). EHD dimers are formed by interactions between highly conserved (see Appendix E) hydrophobic and charged residues from helices α6 of opposing monomers (Figure 18) (Daumke et al., 2007). Residue W238 is at the center of the interface and buried in a hydrophobic pocket. Mutations of this residue render the protein insoluble (Daumke et al., 2007).

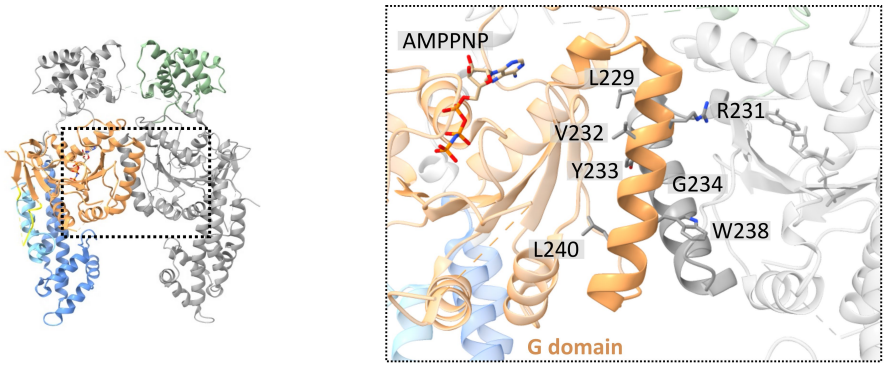

Figure 18. Dimerization interface in EHD proteins. The crystal structure of mouse EHD2 is shown on the left. A magnified view of the dimerization interface is on the right. The dimerization interface involves hydrophobic and charged residues from helix α6 in the G domain. These residues are highly conserved (numbers correspond to mouse EHD2). The nucleotide binding pocket is not involved in dimerization in EHD proteins.

All other members of the dynamin superfamily dimerize across the highly conserved G-interface which involves the nucleotide binding pockets (Figure 19) (Chappie et al., 2010). In these dimers, the active sites face each other, thereby sequestering the nucleotides from the solvent and reciprocally stabilizing the switch regions, while the BSEs (bundle signaling elements) extend in opposite directions from the dimer core. The formation of this interface is crucial for the GTPase activity (Chappie et al., 2010).

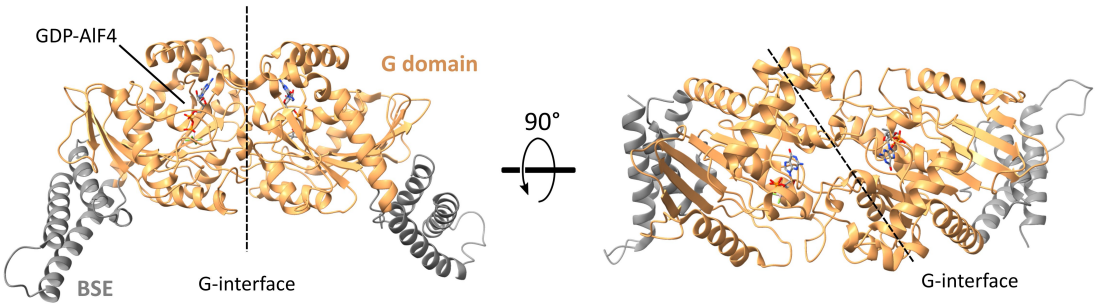

Figure 19. Members of the dynamin family dimerize across the G-interface. The GTP binding pockets of opposing monomers face each other. The structure corresponds to the GG dimer of human dynamin 1 bound to GDP-AlF4 (PDB: 2X2E, (Chappie et al., 2010)). BSE: bundle signaling element.

In contrast, the ATP binding pockets in EHD proteins point in opposite directions within the dimer (Figure 20, panel A). Crystallographic studies previously suggested that the G-interface might

form in EHD proteins and that it could be involved in oligomerization (Daumke et al., 2007; Melo et al., 2017). The cryo-ET structure of oligomerized EHD4ΔN revealed that the canonical G-interface is indeed assembled between the G domains of two adjacent dimers within the oligomeric filament (Figure 20, panel B) (Melo et al., 2022). The G-interface in EHD proteins is now referred to as interface-3 in the oligomeric assembly (Melo et al., 2022) (see next section).

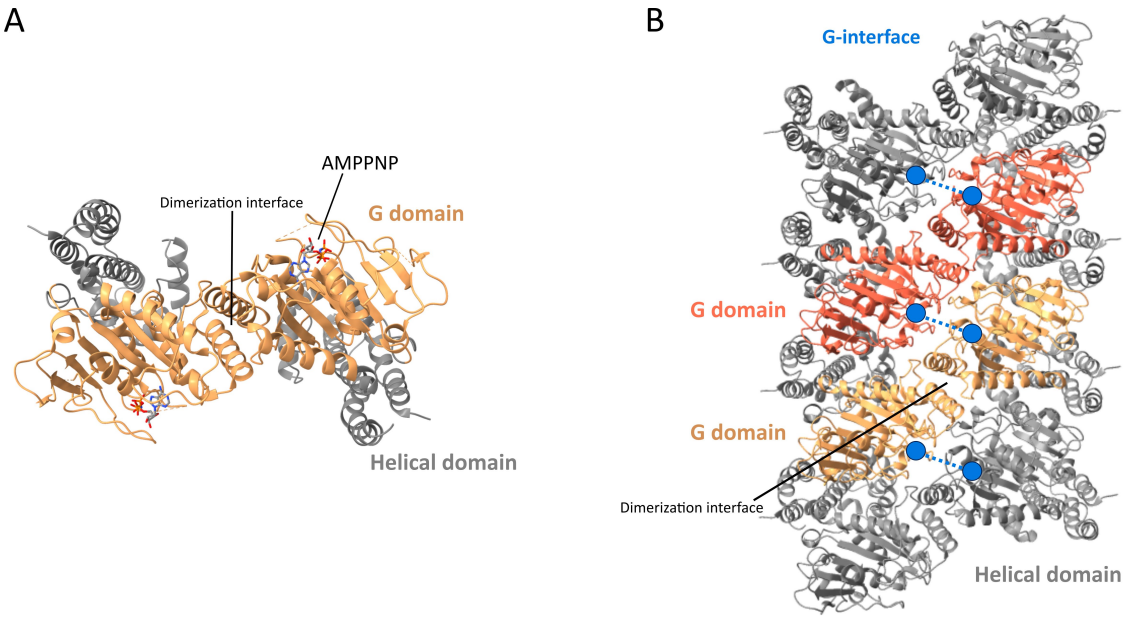

Figure 20. The G-interface in EHD proteins. A) Top view of the crystal structure of mouse EHD2 (the EH domains are not shown for a better visualization, PDB: 2QPT). The nucleotide binding pockets point to opposite directions and the canonical G-interface cannot be formed within one EHD dimer. B) Top view of the cryo-ET structure of an EHD4ΔN oligomeric filament (the EH domains are not shown for a better visualization, PDB: 7SOX). The formation of the G-interface involves the G domains of adjacent dimers within the filament. The G domains of two consecutive dimers are highlighted in two shades of orange. The blue dots represent the ATP binding pocket and the dashed lines the G-interface.

1.5.3.2. Oligomerization in EHDs

Electron microscopy of negatively stained samples of EHD2 showed that it can remodel liposomes into tubules and form ring-like oligomeric structures around them (Figure 21) (Daumke et al., 2007). Daumke and colleagues suggested that EHD2 dimers could oligomerize via the G-interface (see previous section) and speculated that the EH domains might switch from the top site in the dimer to a lateral position (Daumke et al., 2007). Moreover, the formation of organized oligomers was proposed to be dependent on ATP binding (Morén et al., 2012; Shah et al., 2014).

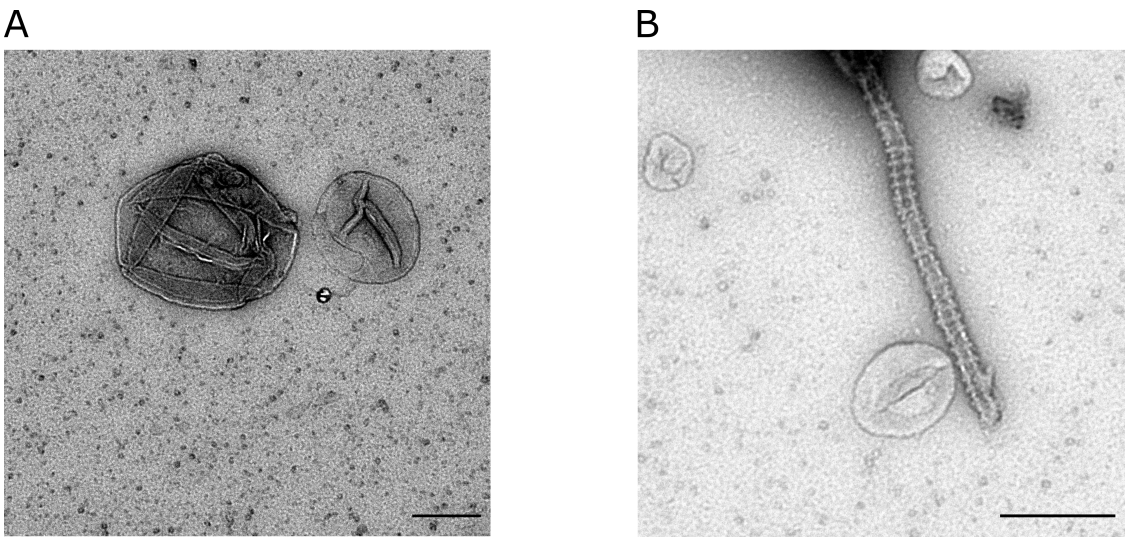

Figure 21. EHD proteins oligomerize on the surface of lipid bilayers. A) Electron micrograph showing Folch liposomes. B) Electron micrograph showing that EHD2 remodels liposomes into tubules and forms oligomeric ring-like structures around them in the presence of ATP. Scale bars: 200 nm.

Later, the crystal packing of N-terminally truncated EHD4 in the open conformation (see Section 28) was proposed to reflect an oligomerized EHD (Melo et al., 2017). Melo and colleagues suggested that, apart from the G-interface, oligomerization could be driven by an additional interface established between the KPF loop of one dimer (occupying the hydrophobic pocket in the G domain) and the helical domain of the opposing dimer (Melo et al., 2017). Moreover, the lack of electron density for the EH domains on top of the dimer further supported the idea that the EH domain might be flexible and switch positions upon oligomerization (Daumke et al., 2007; Melo et al., 2017). In this same study, an oligomerization model was proposed in which EHDs exist in a closed and autoinhibited state in solution but are in the active and open state when bound to membranes. In parallel, another study carried out with EHD2 found similar results about the open conformation representing the active membrane-bound and oligomerized state of an EHD protein (Hoernke et al., 2017).

The models proposed in these investigations were mainly based on crystallographic structures and, evidently, the actual conformation of an EHD protein bound to the lipid bilayer remained unknown. Recently, new insights about the oligomerization mechanism in EHD proteins were provided by the cryo-ET structure of EHD4ΔN (Melo et al., 2022). This structure confirmed the previous hypothesis that oligomerization is driven by the formation of two interfaces: 1) contacts between the KPF loop and the helical domain of the adjacent dimer (termed interface-2), and 2) the G-interface between the nucleotide pockets of opposing monomers (termed interface-3) (Figure 22) (Melo et al., 2022). Unexpectedly, this study revealed that EHD4ΔN is in the closed

conformation in its oligomeric membrane-bound form (Figure 22, see also Figure 17, panel C) and a new model was proposed: ATP-bound dimers exist in solution in the open conformation and are recruited to flat membranes where they oligomerize via interface-2. Membrane curvature induces the transition to the closed conformation, that allows the membrane-binding site to insert into the bilayer and promote increased membrane bending. At high curvature, a stable helical filament (EHD2 may form ring-like structures as seen by negative stain electron microscopy (Figure 21, and (Daumke et al., 2007; Shah et al., 2014)) can be formed by engaging interface-3. In this state, the protein can further constrict the membrane generating tubes decorated with protein filaments (Figure 22) (Melo et al., 2022).

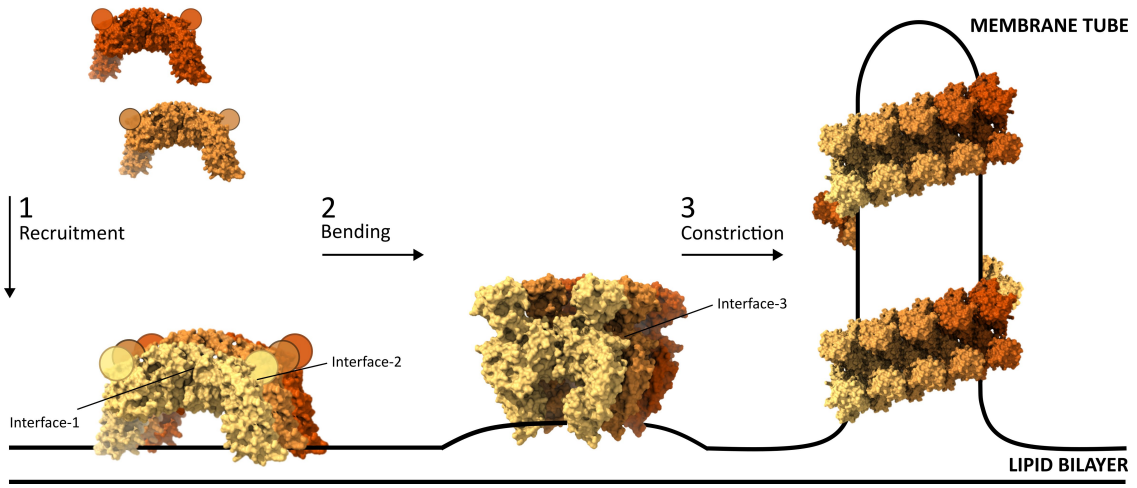

Figure 22. EHD oligomerization model. 1) EHD dimers in the open conformation are recruited to flat membranes where they oligomerize via interface-2. Interface-1 corresponds to the dimerization interface. 2) Membrane curvature induces the transition to the closed conformation. The insertion of the tip of the helical domain in the bilayer generates bent membranes. A stable filament is formed via interface-3. 3) Further constriction of the membrane results in an elongated tube around which helical or ring-like filaments are organized. This model is based on the cryo-ET structure of EHD4ΔN and was proposed in (Melo et al., 2022). The open conformation corresponds to the crystal structure of EHD4ΔN (PDB: 5MTV). Since the EH domains were not solved in this structure, they are represented by circles in the proposed lateral position. The closed conformation corresponds to the cryo-ET structure of EHD4ΔN (PDB: 7SOX).

Oligomerization, both in the open and closed conformations, requires the formation of interface-2. For that, the KPF loop must be in the hydrophobic pocket of the G domain (Figure 23) (Melo et al., 2022). The interaction between the N-terminus and the hydrophobic pocket in the G domain (see Section 1.5.2.3) might happen in solution before recruitment to membranes or after disassembly of the filament.

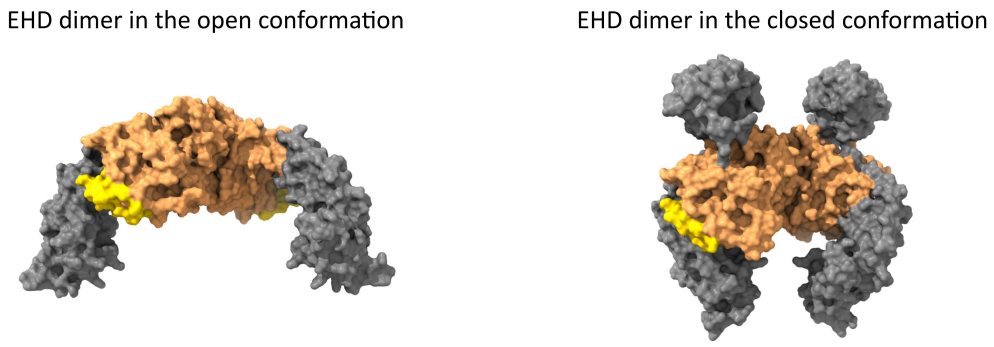

Figure 23. The KPF loop occupies the hydrophobic pocket in the G domain for oligomerization. Oligomerization of EHD dimers is driven by the formation of interface-2 between the KPF loop in one dimer and the helical domain in the adjacent dimer. For these contacts to be established, the KPF loop must be buried in the hydrophobic pocket of the G domain. This conformation has been found both in the open state, here represented by the crystal structure of EHD4ΔN (PDB: 5MTV), and in the closed state, here represented by cryo-ET structure of EHD4ΔN (PDB: 7SOX).

Contrary to previous speculations, in EHD4ΔN filaments the EH domains are placed above the G domains and do not adopt a lateral position (Figure 22). Although resolved at low resolution (13 Å), the EH domains could be modeled in this structure and were found to be slightly displaced towards the periphery of the filament, consistent with the formation of a G-interface (Figure 24) (Melo et al., 2022). Moreover, there was electron density suggesting that the EH domains from adjacent dimers might contact each other (Figure 24) (Melo et al., 2022).

Another important and interesting aspect that was revealed by the cryo-ET structure of EHD4ΔN is that the oligomeric filaments can assemble on membranes of different curvature (Figure 25). Depending on the degree of curvature, EHD4ΔN filaments vary in pitch, rise and subunits per turn (Melo et al., 2022). Melo and colleagues could show that the helical angle (deviation of the helical filament from a simple ring around the tube) increased as the tube radius decreased. This is possible because individual EHD4ΔN dimers adapt their orientation to generate filaments of different conformations in different tube diameters (Melo et al., 2022). EHD oligomers vary from the canonical oligomer architecture shared by several proteins of the dynamin family, like dynamin, DRP1, MxA and Mgm1/OPA1. As introduced in previous sections, the stalk is the central assembly hub in these proteins and the G domains are oriented to the outside of the filament. In opposition, the nucleotide-dependent interface (interface-3) in EHDs is oriented along the filament (Melo et al., 2022).

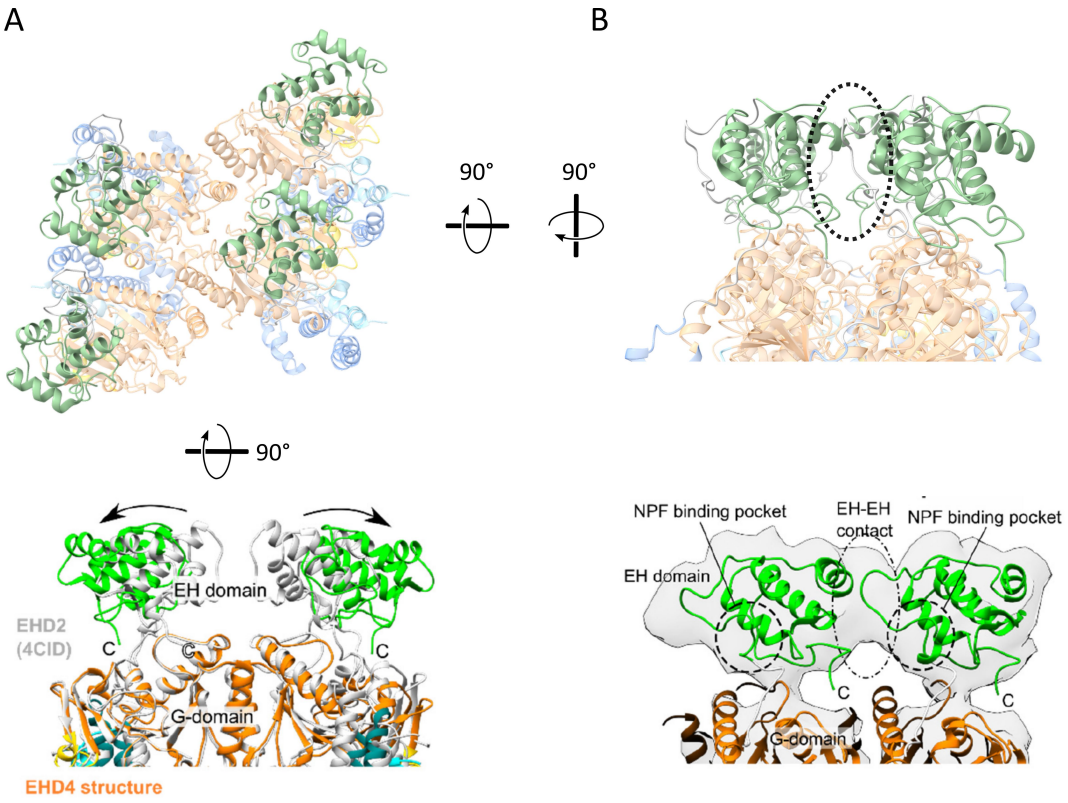

Figure 24. The EH domains are displaced towards the periphery. A) Upper panel: top view of the cryo-ET EHD4ΔN filament showing one tetramer. The EH domains sit on top of the G domains and do not adopt a lateral position in the filament. EH domains were assigned to the monomer directly below. Bottom panel: front view of the EHD4ΔN (colored cartoons) overlaid with the crystal EHD2 structure (gray cartoons). The EH domains are slightly displaced towards the periphery of the filament. They would clash in the oligomerization model based on the EHD2 structure. B) Upper panel: side view of the EH domains in the cryo-ET EHD4ΔN filament. Bottom panel: same view as in the upper panel showing the EHD4ΔN model fitted in the density. The contact between the EH domains of adjacent dimers is highlighted inside the dashed ellipse. Both bottom panels are modified from (Melo et al., 2022).

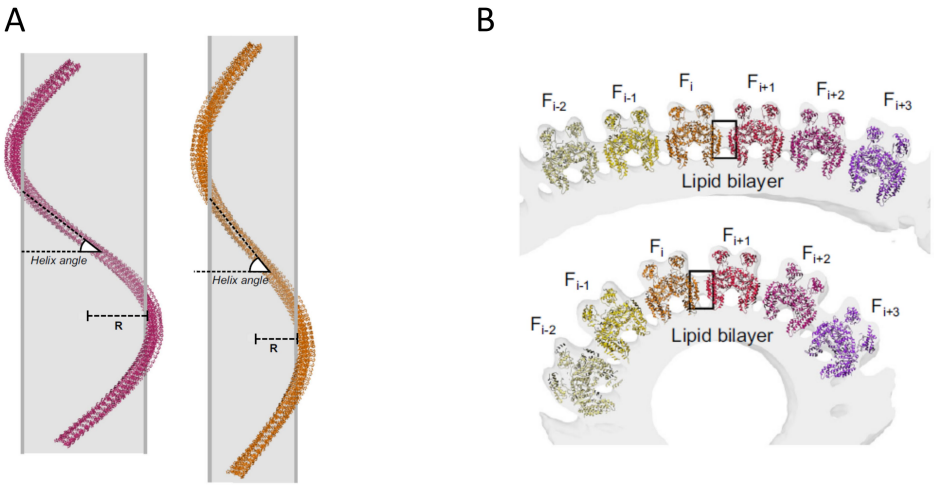

Figure 25. EHD4ΔN filaments adapt to different membrane curvatures. A) The helical angle of the filament increases as the tube diameter decreases (higher membrane curvature). B) The angle between filaments increases in tubes of higher curvature (bottom). Figure modified from (Melo et al., 2022).

1.5.4. ATP hydrolysis in EHD proteins

EHD proteins bind and hydrolyze ATP to ADP. Like other dynamin proteins, ATP hydrolysis is stimulated by membrane binding (Daumke et al., 2007). The ATPase activity in EHDs seems to be fundamental. It has been shown that the loss of ATP binding ability renders EHD2 completely cytoplasmatic and altered ATP hydrolysis rates affect both membrane binding and membrane remodelling (Daumke et al., 2007; Morén et al., 2012; Stoeber et al., 2012). For example, the hydrolysis mutant T94A generates distorted and enlarged caveolae and the nucleotide binding deficient mutant T72A cannot localize to caveolae (Daumke et al., 2007; Hoernke et al., 2017; Morén et al., 2012; Stoeber et al., 2012). Furthermore, the transfection of the ATPase deficient mutant F122A in EHD2 knock-out cells failed to recover the enlarged lipid droplet phenotype (Matthaeus et al., 2020). Remarkably, the absence of the EH domain was found to prevent ATP hydrolysis in EHD2 (Daumke et al., 2007; Morén et al., 2012). Also the deletion of the N-terminus results in an ATPase deficient EHD2 construct (Shah, 2013). Similar results were obtained when analogous residue mutations were investigated in EHD4 (Melo et al., 2017). It was also found that ATP hydrolysis in EHD1 is essential for endocytic recycling (Deo et al., 2018).

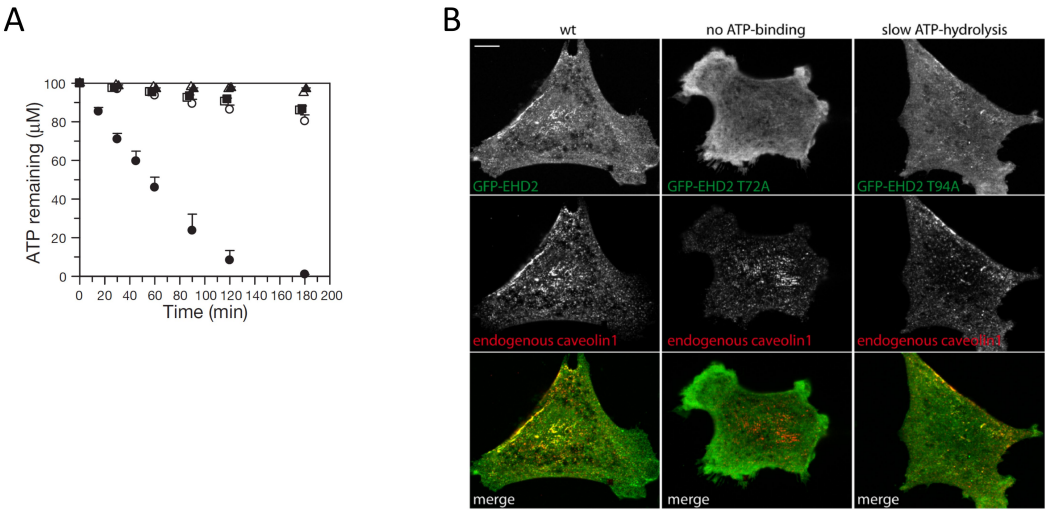

Figure 26. The ATP hydrolysis of EHD2 is stimulated on membranes and is essential for its function in the cell. A) The intrinsic ATPase activity of EHD2 (open circles) is very low but it is stimulated in the presence of Folch liposomes (filled circles). Open and filled squares correspond to the T72A mutant, which cannot bind ATP. Open and filled triangles correspond to GTP measurements. Figure modified from (Daumke et al., 2007). B) Fluorescence micrographs of 3T3-L1 cells expressing GFP-tagged EHD2 variants and co-stained for endogenous caveolin-1. ATP binding and hydrolysis are necessary for membrane targeting. Figure modified from (Morén et al., 2012).

According to the importance of ATP hydrolysis, previous studies have suggested that ATP binding is involved in the formation of regular oligomers since it stabilizes the switch region thereby promoting oligomeric assembly (Melo et al., 2017, 2022). It has also been suggested that membrane binding only occurs when the protein is bound to ATP (Deo et al., 2018; Hoernke et al., 2017; Melo et al., 2017). Moreover, membrane remodelling/tubulation is believed to happen in an ATP-dependent manner (Daumke et al., 2007; Deo et al., 2018; Melo et al., 2017, 2022; Shah et al., 2014). In fact, Melo and colleagues showed that, in the absence of nucleotide, EHD4ΔN can bind to the surface of liposomes, but does not assemble into a filament nor forms tubules (Melo et al., 2022). In addition, only the nucleotide-bound EHD1 forms membrane remodelling scaffolds (Deo et al., 2018).

For some time, it was unclear whether EHDs utilize the energy from ATP hydrolysis for membrane sculpting activities like other members of the dynamin family. However, several authors have hypothesized that ATP hydrolysis might be required for the disassembly of the protein filament and detachment from the membrane. This hypothesis has already been proposed for EHD4, EHD2 and EHD1 (Deo et al., 2018; Hoernke et al., 2017; Melo et al., 2022). Consequently, it was suggested that ATP has a dual role: ATP binding is required for membrane insertion and oligomeric assembly, and ATP hydrolysis is required for dissociation (Deo et al., 2018; Hoernke et al., 2017; Melo et al., 2022). Together with the cryo-ET structure of EHD4ΔN, Melo and colleagues argued that ATP hydrolysis may act as an intrinsic timer to disassemble the EHD scaffold (Figure 27).

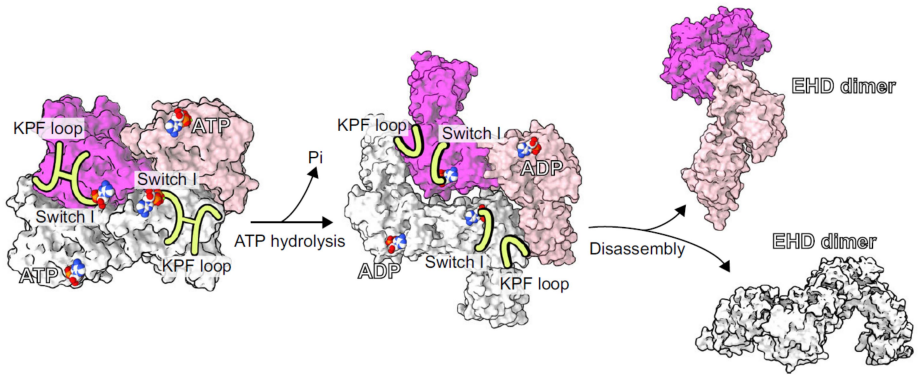

Figure 27. ATP hydrolysis may lead to dissociation of the oligomeric filament. ATP hydrolysis destabilizes the G-interface, since in ADP-bound dimers the interaction between the KPF loop and the switch I region is weakened. This has been suggested to drive disassembly. Figure modified from (Melo et al., 2022).

Since in the ADP-bound state, the interaction between the switch regions and the KPF loop is reduced (Melo et al., 2017), these authors hypothesized that oligomeric interfaces-2 and -3 must also be weakened in the ADP-bound state. This weakening is thought to lead to dissociation of the oligomer (Melo et al., 2022). Furthermore, ATP hydrolysis is expected to destabilize the G-interface, which is also necessary for oligomerization (Melo et al., 2022).

Despite the high conservation, EHDs exhibit quite different ATP hydrolysis rates. For example, EHD2 is a very slow ATPase (5.4 ± 0.2 h^{-1}, (Daumke et al., 2007)), but the stimulated ATP hydrolysis rate is about 40 times higher in EHD1 (Deo et al., 2018) and 7 times higher in N-terminally truncated EHD4 (Melo et al., 2017). This aspect highlights biochemical differences among EHD paralogs, which might be related to their diverse functions in the cell (see Section 1.5.1).

1.5.5. Membrane binding and remodelling

EHDs interact with membranes via the amphipathic helices at the tip of the helical domain (see Section 1.5.2.2) and, possibly, via the amphipathic N-terminal stretch (see Section 1.5.2.3). Additionally, EHDs can remodel negatively charged liposomes into tubules by forming oligomeric filaments on their surface which act as scaffolds (see Section 1.5.3.2).

Previous sections have introduced that, although ATP binding is essential for assembling into regular and organized oligomers, EHDs do not use the energy of ATP hydrolysis to perform their remodelling activities. Instead, the energy to deform a membrane was suggested to be drawn from the EHD2 assembly into membrane-bound oligomers (Hoernke et al., 2017). Investigations using EHD1 showed its preference for high-positive membrane curvature where it organizes into membrane-active scaffolds that bulge the underlying tube causing extension and thinning at intermediate regions of the tube (Deo et al., 2018). Furthermore, a significant fraction of the bulged and thinned tubes (below 25 nm in radius) underwent scission (Deo et al., 2018). These authors claimed that membrane bulging results from the underlying lipid bilayer adapting to the arc-shaped membrane binding surface of EHDs.

This idea has been supported by the recent publication of the cryo-ET structure of EHD4ΔN (Melo et al., 2022). Although EHD4 did not show any scission capabilities, these authors highlighted the undulating appearance of the outer membrane layer of EHD4-coated tubes and the generation of membrane buckling resulting from the insertion of the helical tip region into the membrane (Melo et al., 2022). Melo and colleagues postulated that curved membranes facilitate the insertion of amphipathic regions in EHDs which, in turn, generate higher curvature by a wedging mechanism.

This deformation of the membrane is believed to promote assembly into helical or ring-like oligomers (Melo et al., 2022). Oligomeric filaments can adapt their orientation and geometry according to the underlying membrane curvature, and can further remodel the membrane into elongated tubules of varying shapes (Melo et al., 2022). These studies have emphasized the differences among EHDs regarding membrane remodelling: the low spontaneous membrane curvature of the EHD4 filament is in line with its reported cellular localization in macroendosomes or early endosomes. In contrast, EHD1 and EHD2 form assemblies around tubes of higher curvature, in accordance to their cellular localization on endocytic tubes and at the neck of caveolae, respectively (Melo et al., 2022). Hence, the preference of different EHD paralogs for specific membrane curvatures observed *in vitro* may reflect their specialized cellular localizations and functions (see Section 1.5.1).

2. Scope of the thesis

Recent studies aimed to characterize the cellular function of EHD2 demonstrated that EHD2 can be found at caveolae of different invagination degrees, and that at highly curved caveolae, EHD2 is required to stabilize membrane curvature at the neck, thereby confining these vesicles to the plasma membrane. However, structural details about how EHD2 performs this function have remained obscure.

Over the past years, large efforts have been made to structurally and mechanistically characterize EHD proteins. Insights about their different conformations, activation mechanism and interaction with the membrane were revealed in several studies. Over the course of my thesis, my colleagues and I examined how lysine acetylation reduces membrane binding and remodelling *in vitro*, and alters the subcellular localization of EHD2:

Lysine acetylation regulates the interaction between proteins and membranes.
Okada AK, Teranishi K, Ambroso MR, Isas JM, **Vázquez-Sarandeses E**, Lee JY, Melo AA, Pandey P, Merken D, Berndt L, Lammers M, Daumke O, Chang K, Haworth IS, Langen R. (2021).
Nature Communications. 9;12(1):6466.

We also investigated the cryo-Electron Tomography of N-terminally truncated EHD4 in its membrane-bound oligomeric conformation:

Cryo-electron tomography reveals structural insights into the membrane remodelling mode of dynamin-like EHD filaments.
Melo AA, Sprink T, Noel JK, **Vázquez-Sarandeses E**, van Hoorn C, Mohd S, Loerke J, Spahn CMT, Daumke O. (2022).
Nature Communications. 10;13(1):7641.

Still, details about the regulatory roles of specific domains in oligomeric assembly and in membrane curvature generation, as well as about the ATP hydrolysis cycle are scarce. The goal of the work carried out in this thesis was to deepen the current understanding of the EHD2 structure, in the context of the membrane, and to provide a link between the structural findings and the reported physiological function of EHD2. To this end, full-length (FL) and N-terminally truncated (ΔN) EHD2 were reconstituted on tubular membranes to determine their membrane-bound oligomeric structure using cryo-Electron Tomography and Subtomogram Averaging. The analysis and comparison of these two structures, together with biochemical assays and electron tomography of resin-embedded cells, have provided a better mechanistic understanding of the oligomeric assembly of EHD2 and its role at caveolae. A manuscript including the results of this thesis is in preparation.

3. Materials and Methods

3.1. Materials

3.1.1. Instruments

Instruments used in this thesis are listed in Appendix A.

3.1.2. Chemicals and reagents

Chemicals used in this thesis are listed in Appendix B.

3.1.3. Enzymes

DNAse I (Roche, Mannheim, D), GST-PreScission Protease (expressed and purified in the laboratory).

3.1.4. Bacteria strains

Escherichia coli Rosetta 2 (DE3) and *Escherichia coli* BL21 (DE3).

3.1.5. Eukaryotic cell lines

Human Umbilical Vein Endothelial Cells (HUVEC) were purchased from Promocell.

3.1.6. Media and buffers

Buffers used in this thesis and their composition are listed in Appendix C.

3.1.7. Software

All software used in this thesis are listed in Appendix D.

3.2. Methods

3.2.1. Protein expression and purification

Mouse EHD2 constructs [full-length (residues 1-543) and ΔN (residues 19-543) were expressed in E. coli (BL21(DE3)-Rosetta2 strain) from a modified pET28 vector as N-terminal His6-tag fusions followed by a PreScission protease cleavage site (according to Daumke et al., 2007). Cells were grown shaking at 37 °C in TB (Terrific Broth medium, HP6.1, Roth). Protein expression was induced by the addition of 40 µM isopropyl-β- D-thiogalactopyranoside (IPTG) at an optical density of 0.6, followed by overnight incubation at 18 °C. Cells were harvested by centrifugation (4500 rpm, 20 min, 4 °C) and pellets were resuspended in Resuspension Buffer. Lysis was carried out using a microfluidizer. After centrifugation (20000 rpm, 40 min, 4 °C), cleared lysates corresponding to the soluble protein fraction were applied to a nickel-charged affinity resin (Ni-NTA). The column was extensively washed with Washing Buffers 1 and 2 and the protein was eluted using Elution Buffer 1. For His-tag cleavage, 150 µg of PreScission protease were used per 5mg of EHD2 construct. The protein sample was dialyzed overnight at 4 °C against Dialysis Buffer for imidazole removal and then re-applied to the Ni-NTA column. Despite cleavage of the His-tag, the protein bound unspecifically to the resin. Consequently, the column was washed with Washing Buffer 3 and the protein was eluted in two steps of increasing imidazole concentration using Elution Buffers 2 and 3. Concentrated protein was injected into a Superdex200 gel filtration column, previously equilibrated with SEC Buffer. A second run of size exclusion chromatography was performed as a polishing step. Fractions containing EHD2 were pooled, concentrated and flash-frozen in liquid nitrogen.

3.2.2. Biochemistry and molecular biology

3.2.2.1. Liposome preparation

Folch fraction I bovine brain lipids were dissolved in chloroform at a concentration of 25 mg/ml. To form the liposomes, 50 µl of the lipid solution were mixed with 200 µl of a Chloroform/Methanol (3:1 v/v) mixture and dried under an Argon stream and inside a desiccator. The lipids were resuspended in Liposome Buffer and sonicated in a water bath for 30 seconds. Liposomes containing additional lipids were prepared as a 50% w/w mixture of Folch fraction and phosphatidylserine or phosphatidylethanolamine, or as a 70/30 % w/w mixture of Folch fraction and galactocerebrosides or cholesterol. When indicated, the resuspended and sonicated

lipids were extruded 11 times through a polycarbonate membrane of different pore sizes (800, 400 and 200 nm).

3.2.2.2. ATP hydrolysis assay

The ATP hydrolysis activity of EHD2 constructs was determined in the absence and presence of 1 mg/ml non-extruded Folch liposomes, using 100 µM ATP as substrate and ATPase Buffer. The reaction was incubated at 30 °C and 400 rpm and was initiated by adding the protein at a final concentration of 10 µM. At different time points, 12 µl aliquots were 2.5-fold diluted in HPLC buffer and incubated for 1 min at 80 °C to stop the reaction. ATP and ADP were separated using a reversed-phase Hypersil ODS-2 C18 column equilibrated with HPLC Buffer. Nucleotides were detected by absorption at 254 nm and quantified by integrating the corresponding peaks.

3.2.2.3. Liposome co-sedimentation assay

The binding of different EHD2 constructs to vesicles was determined using 10 µM protein and 1 mg/ml Folch liposomes in Liposome Buffer. The reaction was incubated at room-temperature for 20 min. Samples were spun at 70000 rpm for 30 min at 20 °C. The supernatant and pellet fractions were analyzed by SDS-PAGE.

3.2.2.4. Transformation of chemically competent E. coli cells

Escherichia coli BL21 and Rosetta (DE3) strains were used for plasmid propagation and for protein expression, respectively. For transformation, the heat shock method was employed according to standard methods.

3.2.3. Cell culture

HUVEC cells were grown at 37 °C and 5% CO_2 in DMEM (Gibco Dulbecco's Modified Eagle Medium, Thermo Scientific) supplemented with 10% fetal bovine serum and 1% penicillin-streptomycin. When confluent, cells were split using trypsin/EDTA for detachment. The maximum number of passages was kept below 30.

3.2.4. Transmission Electron Microscopy

3.2.4.1. Tubulation assay

For the generation of protein-decorated lipid tubules, 10 µM of the indicated EHD2 construct was incubated with 1 mg/ml Folch liposomes in Liposome Buffer and, when indicated, in the presence of 1 mM ATP. The reaction was incubated at room-temperature for 15 min. Samples were deposited on carbon-coated copper grids. After 30 seconds, excess of sample was blotted on filter paper and 4 µl of 2% uranyl acetate were applied for 30 seconds to negatively stain the sample. Excess of stain was removed by blotting and grids were air-dried. Electron micrographs were collected using a Talos L120C at 120kV.

3.2.4.2. Cell fixation, embedding and sectioning

Cells were cultured and transfected (when indicated) as described above. Once cells reached confluency, culture dishes were handed to the MDC Electron Microscopy Facility for fixation, staining, resin embedding and sectioning.

For tomography of semi-thin sections (150 – 180 nm), a 1:30 dilution of 5 or 10 nm fiducial gold beads was spotted for 30 seconds on glow-discharged formvar, and carbon coated copper grids. Excess of beads was removed by blotting on filter paper and grids were washed twice using milliQ water. These grids were used to fish the sections from the microtome.

3.2.4.3. Electron tomography of thick sections

Tilt series of thick sections were acquired using a Talos L120C at 120kV and the software SerialEM. Images were collected from 60° to -60° with a 2° increment and bidirectionally, starting at 0°. Tomograms were reconstructed using IMOD. For caveolae morphology analysis and visualization, tomograms were binned 4 times and reconstructed using a SIRT-like filter with 8 iterations. Measurements were done in IMOD. Structures of interest were segmented using Microscopy Image Browser and Amira. Smoothening of segmented surfaces, visualization and videos were created using Chimera and ChimeraX.

For statistics and plotting, GraphPad Prism v.7.05 was used. Normal distribution was assessed by applying a D'Agostino-Pearson test. To calculate the significant difference between two groups, normally distributed data was analyzed using a Student t-Test (two-tailed P-value), otherwise a Mann-Whitney-Rank-Sum (two-tailed P-value) was used. Differences of $p \leq 0.05$ were considered significant ($p \leq 0.05$*, $p \leq 0.01$**, $p \leq 0.001$***, $p \leq 0.0001$****).

3.2.5. Cryo Electron Tomography and Subtomogram Averaging

3.2.5.1. Sample preparation and data collection of EHD2 samples

The ratios of the membrane tubulation reaction described in Section 3.2.4.1 were adjusted and optimized for cryo conditions. Firstly, the indicated EHD2 construct was diluted to a working stock concentration of 300 µM using Cryo-EM Buffer. Samples were prepared by incubating 80 µM of the indicated EHD2 construct with 1.125 mM ATP for 5 min at room temperature. Afterwards, Folch liposomes were added to yield a final concentration of 2 mg/ml and the sample was incubated for 10 min at room temperature. For apo conditions, the 5 min incubation with ATP was omitted. Prior to plunge-freezing in liquid ethane, 5 nm gold beads were added to the sample at a 1:40 ratio. Glow-discharged carbon-coated copper Quantifoil grids were spotted with 4 µl of sample, back-blotted for 3 seconds and plunge-frozen using a Vitrobot Mark II device. Tilt series were acquired using a ThermoScientific Titan Krios electron microscope equipped with a Gatan K2 detector and operated at 300 kV. All tilt series were collected using the software SerialEM and, in some cases, in combination with the PACEtomo package. The nominal magnification was 42,000 x resulting in a pixel size of 1.1 Å in super-resolution mode. Tilted images were collected following a dose-symmetric scheme from -60° to 60° degrees with a 3° increment. Defocus values ranged from -6 to -2.5 µm. More details about data collection are available in Appendix G.

3.2.5.2. Data processing and tomogram reconstruction

Tomograms were reconstructed either manually using the Etomo package from IMOD, or semi-automatically using tomoBEAR. Tomograms were generated as weighted back projections. Eight-times binned tomograms were used to pick particles. Subtomograms were manually picked along the axis of the lipid tubules in Dynamo. Initial particles had a size of 100 voxels.

3.2.5.3. Subtomogram Averaging

This part of the work was carried out by my collaborator Vasilii Mikirtumov (Kudryashev Lab, MDC, Berlin), who also wrote this section.

The initial coordinates of full-length EHD2 particles were imported into SUSAN and reconstructed with the angular information from the drawn models. This initial average showing cylindrical density was used as a starting reference for alignment of eight-time-binned subtomograms. Two iterations with only translational searches and fixed low-pass filter, followed by 10 iterations with translational and rotational searches and adaptive low-pass filter were performed. At this stage halves of rings were aligned to each other, indicating that tubes have

different radii. These 14491 particles were then imported into RELION4-beta and classified into 8 classes in bin 8 with global angular search and 7.5o degree step. Four classes with 6932 particles representing rings of different radii were selected for further processing. All particles were pooled and averaged, followed by symmetry expansion with C8 point-group. Although the underlying data does not have the C8 symmetry, this trick was used in order to sample the non-aligned parts of the rings, effectively performing subboxing along the ring surface. Half-set IDs of subboxed particles were kept same as their respective "full-ring" particles to ensure no spurious correlations in the FSCs. Particles were then recentered on the ring surface and subjected to auto-refinement in bin 8. After this, some subboxed positions converged on the same particles, leaving 44095 particles after duplicate removal. Consecutive rounds of auto-refinement followed by duplicate removal were performed in bin 2 (with and without imposing local symmetry) and bin 1, followed by one round of polishing and CTF refinement without high-order aberrations. Final auto-refinement of polished particles in bin 1 with C2 symmetry led to a 9 Å resolution map. A final cycle of TomoFrameAlignment and CTF refinement with tighter mask resulted in an 8 Å resolution map. A final subset of 37169 particles before polishing was then converted into a dynamo-style table and then projected on the high-dose non-tilted images and converted to SPA-style particles STAR file. This was done with the custom script adopted from the hybridSTA method. These particles were imported into CryoSPARC and subjected to local refinement with non-uniform filtering, angular search constrained to 1 degree and translational search to 10 Å. Then, particles were reoriented to match C2 point-group symmetry axis and C2 symmetry was applied in all successive alignment rounds. The consensus map of the row of 14 EHD2 monomers was used to focus on the central six monomers of EHD2 and the particle set was expanded by subboxing four monomers on each side, giving a final set of 75439 particles after duplicate removal. Several rounds of particle subtraction, mask optimization and local refinement were performed. Lastly, the final particle stack was re-imported back into RELION for reconstruction, postprocessing and local resolution estimation. The final map had a nominal resolution of 6.7 Å.

From the initially picked 98584 particles of N-terminally truncated EHD2, only 30449 were kept by excluding coordinates closer than 136 Å, imported into SUSAN and reconstructed with the angular information from the drawn models. This initial average showing cylindrical density was used as a starting reference for alignment of subtomograms in bin 8 (17.104 Å/pix). Two iterations with only translational searches and fixed low-pass filter, followed by 10 iterations with translational and rotational searches and adaptive low-pass filter were performed. These particle coordinates were projected on to high-dose at 0° tilt micrographs with modified hybridSTA script extracted and binned 4 times and subjected to 2D classification in RELION (into 50 classes with 600 A circular mask diameter, 25 iterations, T=2 and default global in-plane angular search. 1838 particles from 6 selected classes were imported into RELION4, auto-refined in bin 8 with

spherical mask and global angular search and subjected to 3D classification with 4 classes and alignment constrained to +- 45o degree range. 506 particles from the class showing a full circle on a tube Z-slice were selected and auto-refined. The resulting map was used to subbox protein rows along the pseudo-helix with ChimeraX and custom script to keep particle poses. 17204 particles after subboxing were reoriented to match the symmetry axis, auto-refined in bin 4, bin 2 and bin 1 with applied C2 symmetry, local angular searches and a mask covering the 12 central monomers in the row. Final bin 1 auto-refinement of "polished" particles with a mask covering the 8 central monomers reached 12.4 Å resolution. These particles were then converted into a dynamo-style table, projected on the high-dose non-tilted images, and converted to SPA-style particles STAR file. This was done with the custom script adopted from the hybridSTA method. These particles were imported into CryoSPARC and subjected to local refinement with non-uniform filtering, C2 symmetry, angular search constrained to 1 degree and translational search to 8 Å, giving the final 10.1 Å map of six central monomers. Local resolution was estimated in CryoSPARC.

Illustrative summaries of the subtomogram averaging workflow are available in Appendix F.

3.2.5.4. Flexible fitting and structure determination

This part of the work was carried out by my collaborator Dr. Jeffrey K. Noel (Daumke Lab, MDC, Berlin), who also wrote this section.

The atomic models consistent with the cryo-EM maps were generated using MDfit. MDfit uses the cryo-EM map as an umbrella potential to bias (i.e., deform) an underlying structure-based model (SBM) in order to maximize the cross-correlation between the experimental density and the simulated electron density. An SBM is a molecular force field that is explicitly, albeit not rigidly, biased toward a certain native structure. The SBM for fitting was the EHD2 homo-dimeric crystal structure (4CID) with the sequence homology modeled by Swiss-Model to remove any missing residues. The portion of the SBM for the KPF loop (residues 110-135), which is missing from the EHD2 structure, is based on the EHD4 crystal structure (5MVF). Building the SBM from the two crystal structures ensured that the resulting model was maximally consistent with the crystal conformation. This entailed no significant changes in structure as the sequences are highly similar. A preprocessing step was then necessary to move the EH domains within the dimer into a cis positioning because 4CID placed the EH domains *in trans*. This involved only reorientation of the (421-439 loop), no other residue positions were changed. We refer to this dimeric structure as EHD2-init. An SBM using EHD2-init as the input structure was then generated using SMOGv2.3 with the template "SBM_AA" meaning all non-hydrogen atoms were explicitly represented.

The density corresponding to the central two dimers within the cryo-EM map was chosen as the constraint for MDfit, since this region had the best resolution. Relaxation of the SBM under the influence of the cryo-EM map is performed by molecular dynamics (MD), and, thus, requires an initial condition. Two EHD2-init were rigid-body fit into the map using the “Fit in Map” tool of Chimera. This tetramer includes all studied interfaces and is in principle sufficient to model, however, the unfilled electron density due to missing filament neighbors would disrupt the fit. In order to initialize the neighbors on either side of two dimers, the translational symmetry of the filament was exploited. Four additional copies of EHD2-init were added, two positioned on either side, placed such that each dimer-dimer interface was identical. Technically, this was performed by 1) measuring the transformation X between the two central dimers in VMD, 2) duplicating the central dimers, and 3) applying X or -X to the duplicates. This six-dimer system served as the initial condition for MD. Alternating every 10^4 MD steps, 1) the dynamics were subject to only the SBM and electron density umbrella, 2) additionally a symmetrizing restraint potential. The symmetrizing restraint potential was implemented by rmsd fitting a central monomer to each monomer and employing weak position restraints. This process allowed the structure to explore the cryo-EM density while additionally maintaining the symmetry of the filament. Through this iterative process, the structure converged within 3×10^5 steps. The middle two dimers were taken as the atomic model. Note that even though the filament’s local C2 rotational symmetry was not explicitly enforced by us during MD, the fact that the SBM was based on a C2 symmetric structure ensured that this symmetry was included.

After flexible fitting, the model was refined in real space using Phenix. Some clashes and outliers were fixed using Coot. The results of the refinement are available in Appendix G.

4. Results

4.1. Sample preparation for Cryo-Electron Tomography

4.1.1. Protein purification

Previous studies in our group have demonstrated that several EHD protein constructs are stable in solution and that they can be expressed in high yields (Daumke et al., 2007; Melo et al., 2017; Shah et al., 2014). To reconstitute EHD2 on liposomes, a mouse full-length construct (Figure 28, panel A) was expressed in *E. coli* and purified according to established protocols (Daumke et al., 2007) and as described in Section 3.2.1. A representative SDS-PAGE showing the evolution of the protein sample at different stages of affinity chromatography, as well as after size exclusion chromatography is shown in Figure 28, panel B. The corresponding size exclusion chromatogram can be observed in Figure 28, panel C.

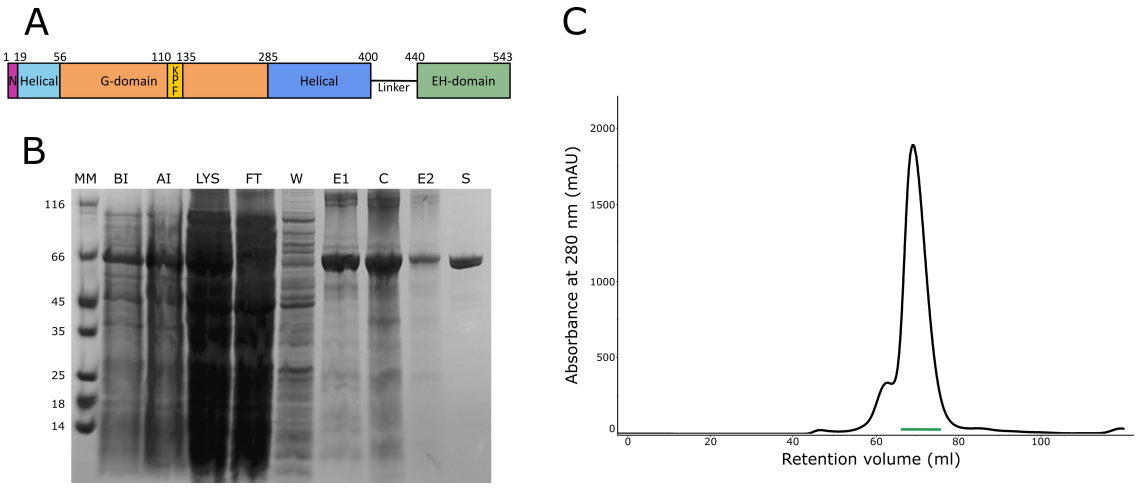

Figure 28. Purification of EHD2 constructs. A) Domain architecture and residue numbering of mouse full-length EHD2. B) SDS-PAGE of the purification of mouse full-length EHD2. MM: molecular marker (kDa); BI: *E. coli* culture before induction with IPTG; AI: *E. coli* culture after induction with IPTG; LYS: soluble extract after cell lysis, applied to the nickel column; FT: flow-through fraction containing contaminants that do not bind to the resin; W: first washing step; E1: eluted fraction from the Ni-NTA resin; C: fraction after His-tag cleavage; E2: eluted protein after re-application to the Ni-NTA column; S: purified EHD2 after size exclusion chromatography. C) Size exclusion chromatogram. Pooled and concentrated protein fractions are indicated by the green line.

Any other construct mentioned in this thesis was purified following the same protocol and yielded similar results.

4.1.2. Evaluation of lipid binding affinity to different types of liposomes

Previous research from our group and others has shown that, like other members of the dynamin family of proteins, EHDs can also bind to membranes and remodel them by oligomerizing on the surface of the lipid bilayer (Daumke et al., 2007; Melo et al., 2017, 2022; Shah et al., 2014). The specificity of EHD2 to bind to liposomes depends on their lipidic composition. EHD2 can efficiently bind to brain-derived lipids (Folch extract) and to phosphatidyl-serine, whereas the affinity to phosphatidyl inositols (PtdIns) is lower and varies depending on the type, with the highest binding affinity found for PtdIns(4,5)bisphosphate (Daumke et al., 2007). A recently published cryo-ET structure of an EHD4 construct was determined in the presence of liposomes containing a mixture of Folch lipids, phosphatidylethanolamine and cholesterol (Melo et al., 2022). These studies show the relevance of using an appropriate lipid composition to boost binding of EHDs to the membrane and allow membrane remodelling.

The preference of EHD2 to bind a certain type of liposomes was evaluated in order to select those which would yield the most efficient interaction. For the same reason, liposomes varying in size were tested. Liposome co-sedimentation assays were carried out as described in Section 3.2.2.3.

Figure 29 shows that EHD2 binds to Folch liposomes with high affinity (panel A). Using a mixture of Folch lipids and phosphatidylserine or phosphatidylethanolamine did not increase binding. However, slightly decreased co-sedimentation was observed when liposomes containing galactocerebrosides or cholesterol were tested (Figure 29, panel A). Regarding the preference of EHD2 to bind liposomes of a certain size, non-extruded liposomes and liposomes extruded through an 800 nm filter did not yield significant differences (Figure 29, panel B). Per contra, membrane binding was decreased when smaller liposomes (extruded through 400 nm and 200 nm filters) were employed (Figure 29, panel B).

Figure 29. Co-sedimentation assays to analyze how the lipid composition and size of liposomes affects membrane interaction. A) Liposomes containing different lipids were tested. EHD2 shows high affinity to 100% Folch liposomes (F). Similar binding was observed for liposomes containing a mixture of Folch lipids and phosphatidylserine (PS) or phosphatidylethanolamine (PE) in a 1:1 w/w ratio. Folch liposomes enriched with 30% galactocerebrosides (GC) or cholesterol (Ch) decreased the binding affinity of EHD2. B) EHD2 shows preferred binding to either non-extruded (n.e.) liposomes or to liposomes extruded through an 800 nm filter. Binding is decreased when the size of the liposomes is decreased (extruded through 400 nm and 200 nm filters). In the absence of liposomes (Ctrl), EHD2 remains soluble in the supernatant. S: supernatant fraction after centrifugation. P: pelleted fraction after centrifugation.

This indicates that EHD2 might have a preference to bind to membranes with a lower degree of curvature. This aspect is further analyzed and discussed in the following sections. For convenience, non-extruded liposomes consisting of 100% Folch lipid extract were used for subsequent experiments.

4.1.3. Optimization of the membrane remodelling activity of EHD2

Two important aspects in a sample directly impact the successful protein structure determination by means of cryo-Electron Microscopy and Tomography techniques. One is the requirement of having a highly concentrated sample, with many individual particles per field of view. This is crucial to obtain the large number of particles needed for solving a structure at high-resolution (Weissenberger et al., 2021). The second critical element to consider is sample homogeneity. Although orientation heterogeneity is usually desired in order to visualize the particle from different points of view, successful single particle analysis (SPA) or subtomogram averaging (STA) rely on the homogeneity of the particles to be averaged in terms of size, conformation, and flexibility, among other (Weissenberger et al., 2021). Having the aim of solving the structure of membrane bound oligomerized EHD2 at subnanometer resolution, the sample conditions were optimized to increase the number of protein-decorated tubules and their homogeneity.

Transmission electron microscopy of EHD2-coated lipids was shown previously (Daumke et al., 2007; Shah et al., 2014) and initial cryo-ET conditions were also assayed but could not be exploited at the time (Shah et al., 2014). In the current study, previously existing protocols were reproduced, as described in Section 3.2.4.1 (Figure 30, panels A and B). Using negative-stain electron microscopy, remodelling of liposomes resulting in long lipid tubules was observed. However, tubulation was increased when slight modifications of the ratios between reaction components were tested (Figure 30, panel C). These experimental adjustments consisted of reducing the protein:ATP ratio from 1:100 to 1:14 and the protein:liposomes ratio from 1:1.7 to 1:0.5. These conditions were chosen for the preparation of grids (see Section 3.2.5.1). Nevertheless, even though the number of tubules increased, the heterogeneity of their shape could not be overcome (see Section 4.2.2).

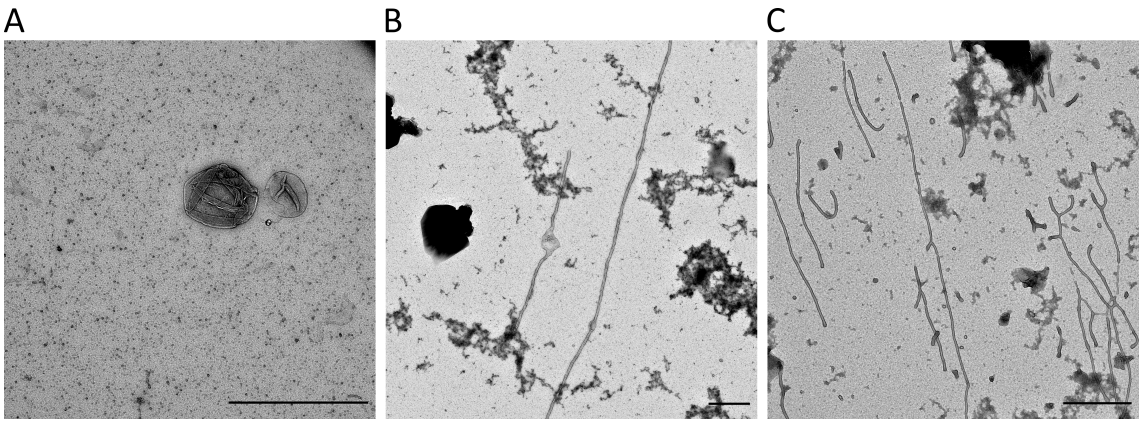

Figure 30. Increased remodelling activity of EHD2. A) Non-tubulated Folch liposomes. B) EHD2 deforms liposomes into tubules in the presence of ATP. C) The tubulating activity of EHD2 could be increased by modifying the ratios of the reaction components. Scale bars: 1 μm.

4.1.4. Selection of grids

Another fundamental aspect for successful cryo-EM/ET data acquisition is selecting the optimal grids which will serve as support for the sample. Different types of grids differ in terms of material, coating, mesh size and hole size.

In the first data acquisition sessions using conventional Quantifoil Holey copper grids with a carbon support, EHD2 tubules were found to stick to the carbon covering the mesh of the grid and were hardly ever found inside the holes, where the electron beam can penetrate best (Figure 31, panel A). After systematically testing different types of grids, copper grids covered with a gold film instead of carbon were found to increase the chances of finding lipid tubules inside the holes (Figure 31, panel B). These grids were used for all cryo-ET tilt series datasets.

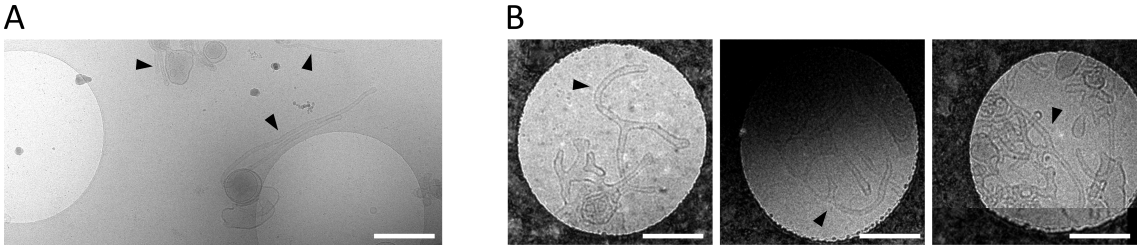

Figure 31. Effects of employing different types of grids. A) EHD2-coated lipid tubules were hardly ever found inside the holes when copper grids with a carbon support were used. B) Using grids carrying a gold film increased the chances of finding lipid tubules inside the holes. Black arrowheads highlight the lipid tubules. Scale bars: 1 μm.

4.2. Overall architecture of EHD2 oligomers

4.2.1. EHD2 assembles on lipid bilayers of different curvature

The cryo-ET structure of an N-terminally truncated EHD4 revealed that it can remodel membranes into tubules and oligomerize forming helices around them (Melo et al., 2022). EHD4 oligomers can assemble on lipid tubules of a wide range of diameters (30 to 100 nm) and adapt their helical geometry according to the curvature of the membrane (Melo et al., 2022).

To gain insights into the overall architecture of oligomerized EHD2, 95 cryo-ET tilt series were collected and reconstructed into tomograms as described in Section 3.2.5.2, using the optimized sample conditions described above and detailed in Section 3.2.5.1. Similar to EHD4ΔN, EHD2 can also oligomerize on lipid bilayers of varying curvature in the presence of ATP (Figure 32). EHD2 can form short filaments on the surface of non-tubulated liposomes, where membrane curvature is low (Figure 32, panel B). At transition areas in which membrane curvature increases, oligomeric filaments can contact each other and remodel the vesicles into lipid tubules (Figure 32, panel C). Continuous oligomeric ring-like filaments were observed around (Figure 32, panel D). As reported for EHD4ΔN (Melo et al., 2022), these results show that EHD2 assemblies can as well adapt to different membrane curvatures. However, in comparison to EHD4ΔN, EHD2 deformed liposomes into tubes of much smaller diameters (Figure 32, panel D and Section 4.2.2) but failed to form continuous filaments on membranes of low curvature, like tubules of greater diameter or on the surface of intact vesicles.

Taken together, these results show that EHD2 filaments form on the surface of membranes of different curvature degrees and suggest that membrane curvature plays a role in the length and shape of the EHD2 oligomers.

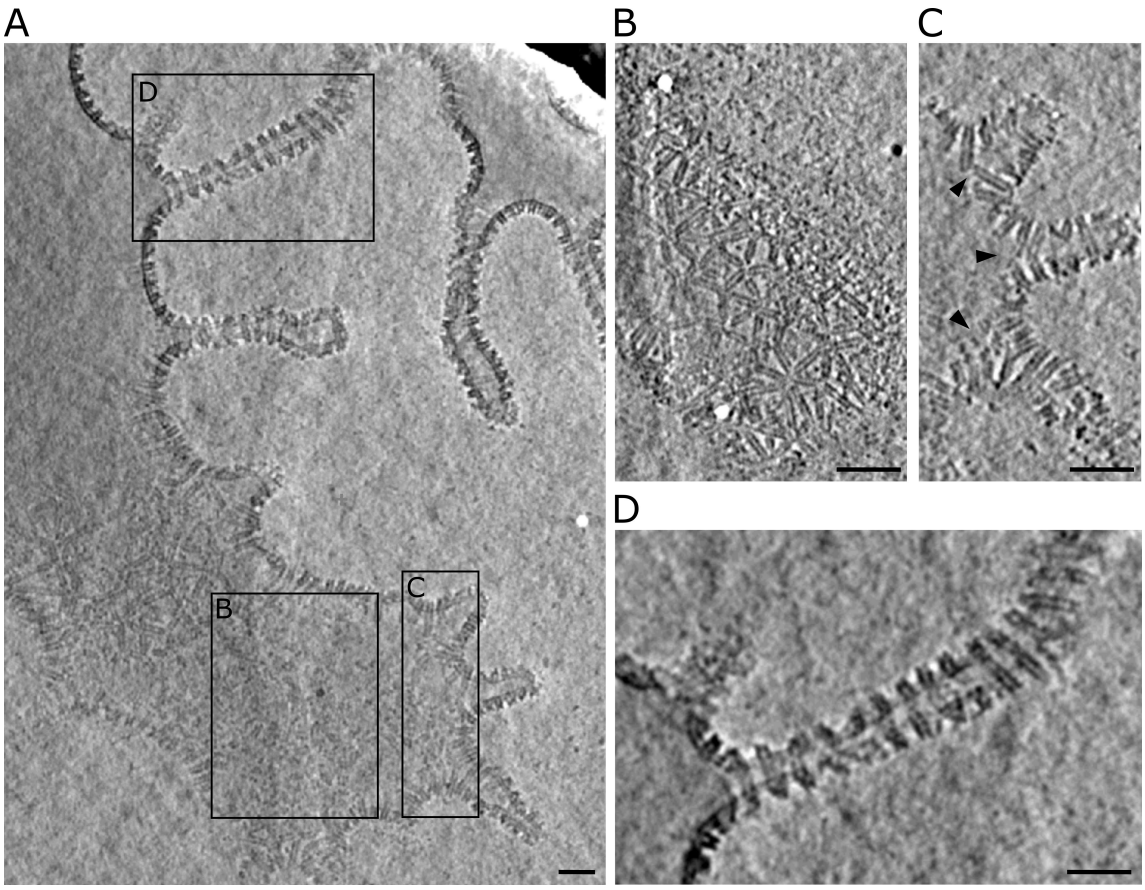

Figure 32. EHD2 forms oligomers on lipid bilayers of varying curvatures. A) Central Z-slice of a representative tomogram shows how EHD2 binds to membranes of different curvature and remodels them into different shapes by oligomerizing on their surface. B) EHD2 can form short filaments on membranes of low curvature. C) Membrane tubulation occurs at areas of higher curvature where oligomeric filaments encounter (arrowheads). D) EHD2 oligomerizes into ring-like structures around lipid tubules of high curvature. Images in panels B, C and D correspond to the inlets highlighted in A and show higher Z slices of the tomographic volume. Scale bars: 50 nm.

4.2.2. EHD2-decorated lipid tubules are heterogenous

The diverse EHD2 oligomeric assemblies that are found in the *in vitro* reconstituted samples may have a biological significance since EHD2 has been localized to both flat and highly curved caveolae (Matthaeus et al., 2022). However, due to the fact that the formation of caveolae and the transition from one degree of membrane curvature to another is a dynamic process (Matthaeus et al., 2022), this study mainly focused on the ring-like structures around lipid tubules, which resemble the proposed stable assembly of EHD2 around the neck of highly invaginated caveolae (Section 1.3.2).

EHD2-decorated lipid tubules are considerably heterogenous in terms of diameter, length, curvature, and branching. Inevitably, this variety of shapes entails diverse oligomeric

configurations: EHD2 filaments are irregularly spaced, there is an uneven number of EHD2 molecules per turn around the tubule, and EHD2 oligomers rest in erratic orientations relative to the axis of the tubule. These sources of heterogeneity are indicated on a representative tomogram in Figure 33, panel A. The differences in orientation and arrangement of EHD2 filaments become even more evident in the subtomogram class averages (Figure 34).

Despite the heterogeneity, it is worth noting that, in comparison to EHD4ΔN tubules, EHD2 tubules are thinner, and their luminal diameters lay within a much narrower range of 18 to 44 nm (Figure 33, panels B and C). These results are in agreement with the model predicted based on the EHD2 crystal structure (Daumke et al., 2007).

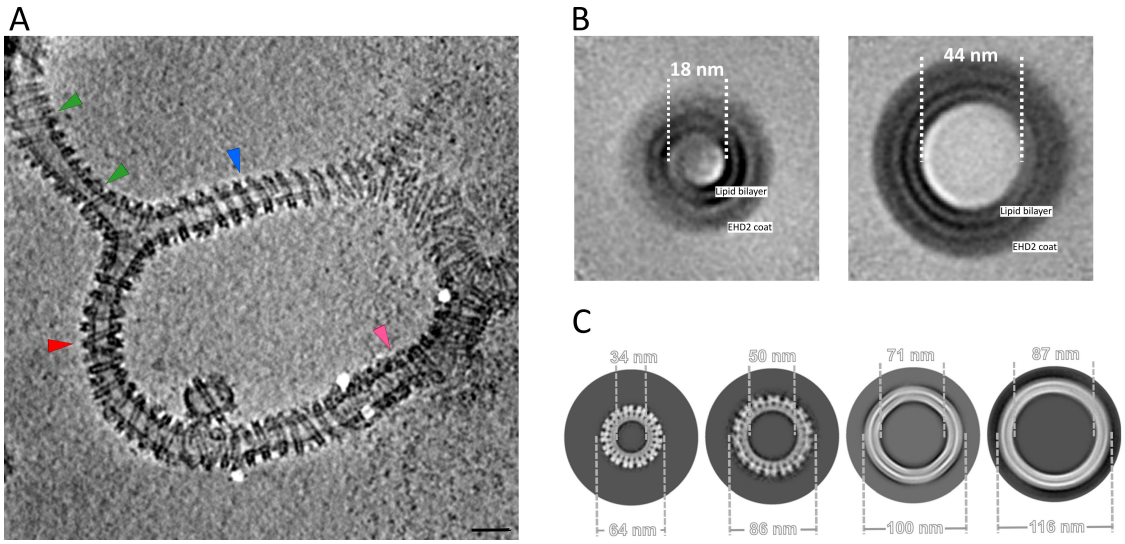

Figure 33. EHD2-coated lipid tubules are heterogenous, but their luminal diameter lies within a narrow range. A) Central Z-slice of a representative tomogram showing different sources of heterogeneity. Tubules can be more or less curved (red versus blue arrowheads) and differ in diameter (green arrowheads). This directly impacts the oligomeric assembly: there is a different number of EHD2 molecules per turn around the tubule (green arrowheads), ring-like structures are positioned in different angles with respect to the axis of the tubule (red versus blue arrowheads) and the spacing between oligomers also varies (blue versus pink arrowheads). Scale bar: 50 nm. B) Cross sections of the projection of all subtomogram averages of EHD2 tubules. The subtomogram classes corresponding to the narrowest and the widest tubules are shown. The luminal diameter range of all tubes is between 18 and 44 nm. C) Cross sections of the projection of subtomogram averages of EHD4ΔN tubules with different diameters. Modified from (Melo et al., 2022).

Taken together with the results presented in the previous section, these results show that EHD2 can assemble into organized filaments and adapt the oligomeric architecture to different degrees of membrane curvature. Moreover, in comparison to EHD4ΔN, EHD2 generates narrower tubules, the diameter of which is very similar to that of the caveolar neck, as reported in the

literature (Matthaeus et al., 2022; Parton, McMahon, et al., 2020; Sotodosos-Alonso et al., 2023) and also in this study (Section 4.6).

4.3. The 6.7 Å cryo-ET structure of oligomeric EHD2

4.3.1. The subtomogram averaging structure

To obtain a subnanometer structure of oligomeric EHD2, an initial set of 14,491 particles were picked along the axis of the lipid tubules found in 95 reconstructed cryo tomograms (See section 3.2.5.3). These subtomograms had a size of 100^3 voxels and could accommodate a full cross-section of the tube. Consequently, between one to three EHD2 ring-like structures (depending on the spacing between them) were included in each subtomogram. As stated in Section 4.2.2., the architecture of the assembly was highly heterogenous, and these big particles yielded noisy averages, despite thorough classification rounds (Figure 34).

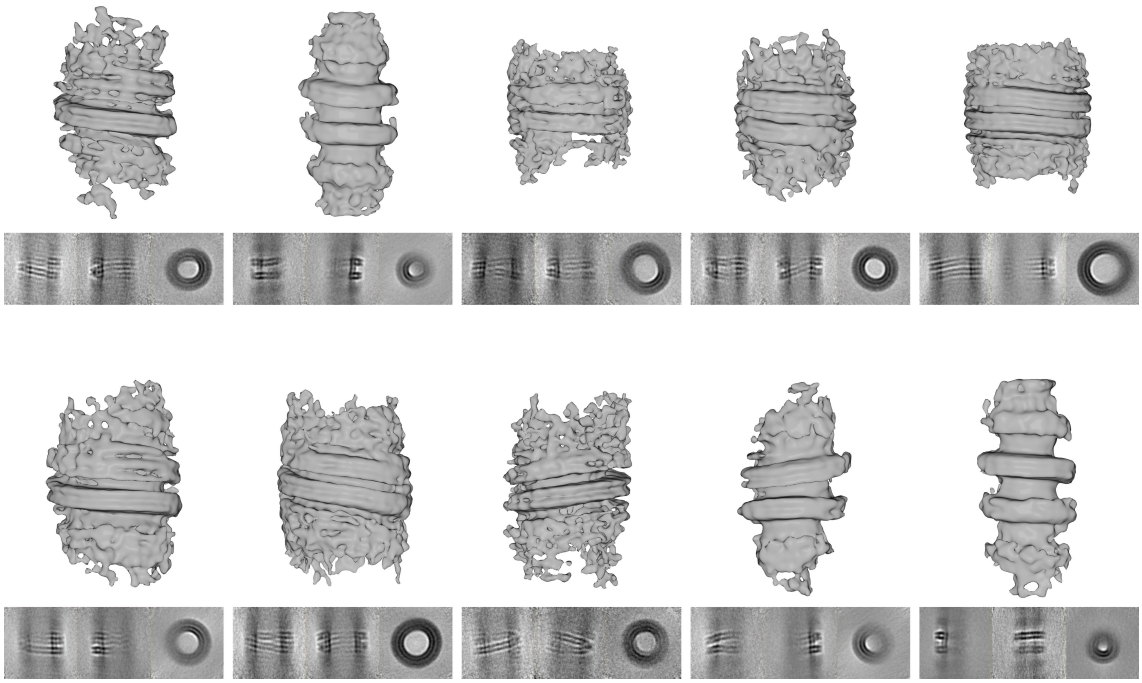

Figure 34. EHD2 subtomograms are too heterogenous and cannot be averaged. An initial set of 14745 100^3 voxel subtomograms were averaged and classified. The results of a multireference alignment using ten references are shown as full projections in x, y, and z views (left, middle and right panels, respectively). A 3D representation of each class

(X-view plane) is shown on top of the corresponding projection. Particles yielded poorly defined averages as a result of the data heterogeneity.

The use of different alignment and classification parameters, as well as applying diverse masks did not improve the average of these subtomograms. Subboxing, a commonly used subtomogram averaging strategy, was employed to overcome sample heterogeneity. Subboxing consists of redefining the area of interest by deriving new particle positions from the initial ones. The new particles are smaller and contain structures which are homogenous throughout the dataset.

This part of the work was carried out by my collaboration partner Vasilii Mikirtumov (Kudryashev Lab, MDC, Berlin), as described in Section 3.2.5.3. A detailed description of the subtomogram averaging workflow for structure determination can be found in Appendix F. A table summarizing data collection parameters and processing values can be found in Appendix G. Briefly, the initial 14,491 particles were subjected to 3D classification but, due to data heterogeneity, only some parts of the full ring-like structures could be aligned. Based on this alignment, four classes representing 6,932 particles were selected for further processing (Figure 35, panel A). A subbox including 14 EHD2 monomers was selected to redefine the size of the particles and a total of 44,095 particles was obtained. Consecutive rounds of auto-refinement, duplicate removal, and polishing with C2 symmetry led to a 9 Å resolution map. Local refinement and further subboxing generated a dataset of 75,439 particles, each including 6 EHD2 monomers (Figure 35, panel B).

The final result of subtomogram averaging is a cryo-EM density map of an asymmetric unit (AU) of six monomers of membrane bound EHD2 at an average resolution of 6.7 Å (Figure 35, panels C and D). Two dimers are formed in the AU (Figure 35, panel C), and the other two monomers included correspond to neighboring dimers within the filament. The core of the protein, and especially the G domains, were solved at a resolution of 6.5 Å, but more flexible areas such as the peripheral helices of the helical domains and the EH domains were solved at lower resolutions, ranging 7 - 7.5 Å. In general, secondary structure corresponding to helices and sheets could clearly be discerned in the density (Figure 35, panel C).

The map revealed that the overall structure is similar to the closed conformation of the EHD2 dimer, represented by two crystal structures (PDB: 2QPT and 4CID, references (Daumke et al., 2007; Shah et al., 2014), respectively) and to the EHD4ΔN membrane-bound oligomer (PDB: 7SOX, (Melo et al., 2022)).

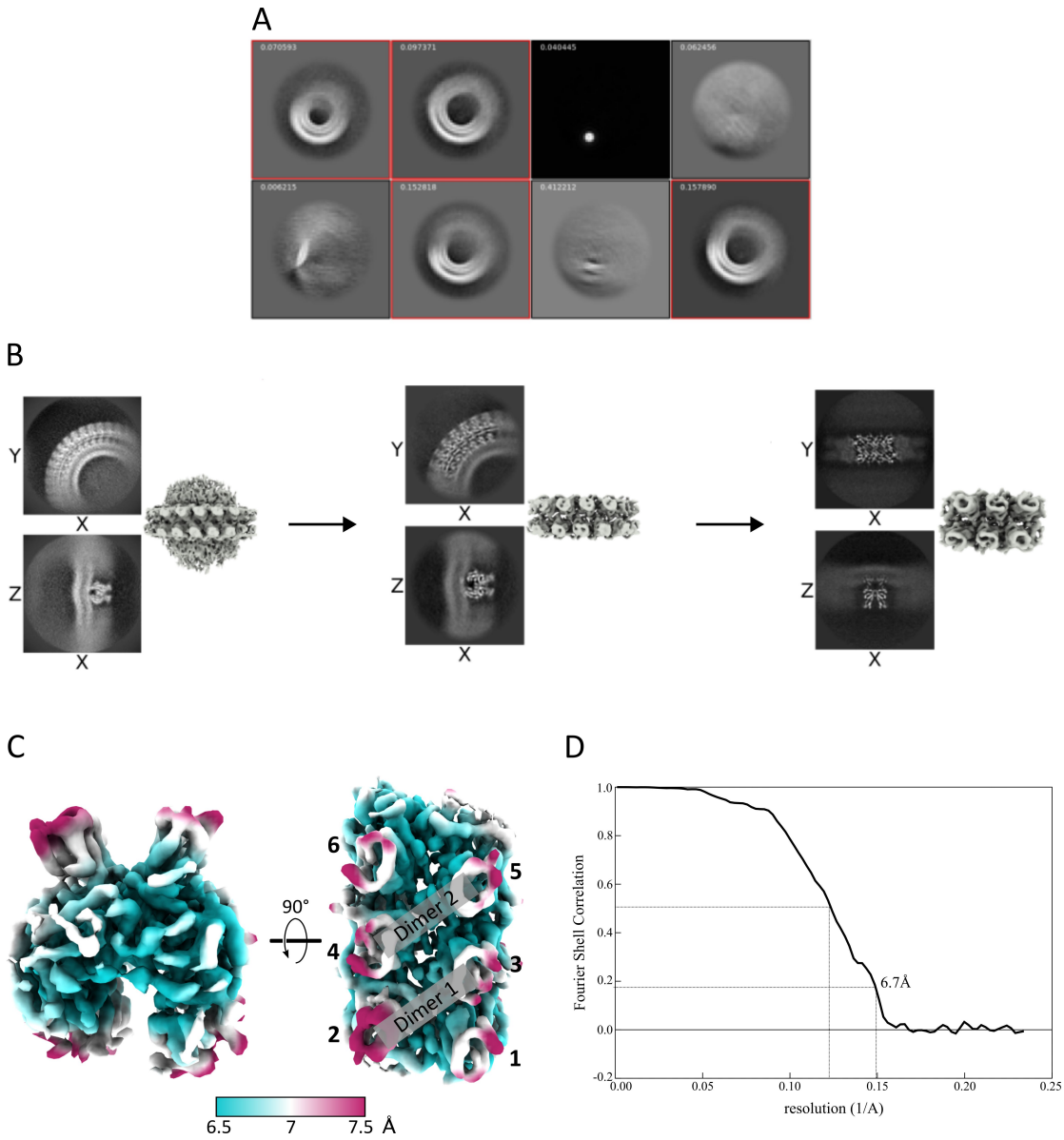

Figure 35. The 6.7 Å cryo-ET structure of membrane bound EHD2. A) The initial 14,491 particles were 3D classified. Four classes (marked in red) were selected for further processing. B) An initial subbox including 14 EHD2 monomers was defined (left panel). Consecutive auto-refinement, duplicate removal and polishing with C2 symmetry generated a 9 Å resolution map (middle panel). To improve resolution, six monomers were subboxed to generate 75,439 particles which were locally refined and postprocessed to obtain a final 6.7 Å resolution map (right panel). C) Front and top views of the AU resulting from subtomogram averaging and subboxing. Six monomers (numbered) are included in the AU; two dimers are formed and the other two monomers correspond to neighboring dimers within the filament. The density is colored according to local resolution values. D) Fourier Shell Correlation curve.

4.3.2. Flexible fitting and refinement

To generate a model, a flexible fitting approach was carried out by my collaborator Dr. Jeffrey K. Noel (Daumke Lab, MDC, Berlin), as described in Section 3.2.5.4. Briefly, the crystal structure of EHD2 (PDB: 4CID, (Shah et al., 2014)) was used for fitting. Since the KPF loop (residues 110 – 135) are missing in this structure, these residues were modeled based on the EHD4ΔN crystal structure (PDB: 5MTV, (Melo et al., 2017)). Furthermore, the EH domains were assigned to the same molecule (*in cis*) in the model used for fitting, instead of to opposite monomers (*in trans*), as it had been done for the cryo-ET EHD4ΔN structure (PDB: 7SOX, (Melo et al., 2022)). However, since the long linker between the helical and the EH domains is disordered (residues 400 – 439), the *in cis* configuration cannot be excluded. The density corresponding to the central two dimers within the cryo-EM map was chosen as the constraint for the fit, since this region has the best resolution. This tetramer is in principle sufficient for the model, however the unfilled electron density could disrupt the fit. To prevent this, four additional copies of the EHD2 dimer were added to each side of the central tetramer and this six-dimer system served for molecular dynamics and accurate fitting (Figure 36).

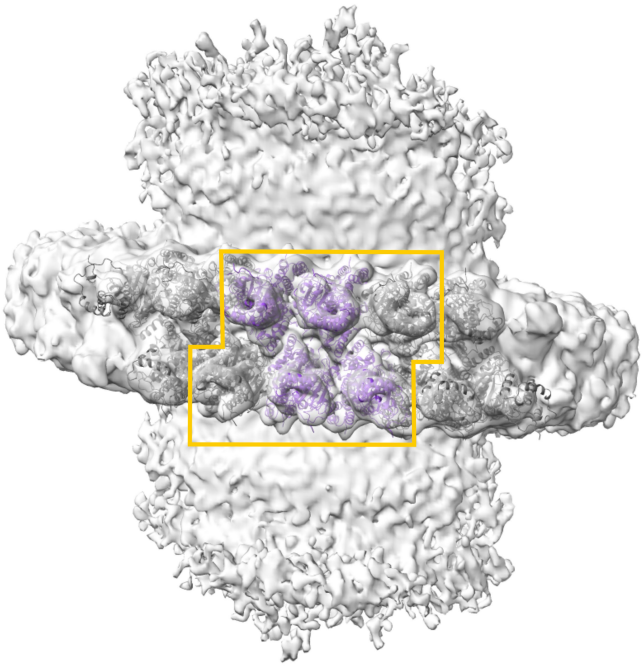

Figure 36. Flexible fitting strategy. The full unmasked cryo-ET map is shown as a 3D surface. The six monomers that correspond to the 6.7 Å asymmetric unit are shown inside the yellow box. The central tetramer of the AU was used for flexible fitting of two EHD2 dimers (purple cartoons). To fill the density for accurate molecular dynamics, four additional EHD2 dimers were added to the side of the central tetramer (gray cartoons).

Because the central tetramer highlighted in Figure 36 includes all interfaces required for oligomeric assembly, it will be used to report the results and conclusions obtained in this work and for visualization in figures, unless stated otherwise.

After flexible fitting, the model was further refined in real space to improve the geometry, reduce molecular clashes, and validate the statistics (Table 1 and Appendix G).

Table 1. Statistics after real-space refinement.

Initial model used (PDB code)	4CID
Map sharpening *B* factor (Å^2)	-200
Model composition	
Non-hydrogen atoms	16576
Protein residues	2084
Ligands	0
R.m.s. deviations	
Bond lengths (Å)	0.004
Bond angles (°)	0.856
Validation	
MolProbity score	2.16
Clashcore	21.26
Poor rotamers (%)	0.00
Ramachandran plot	
Favored (%)	95.18
Allowed (%)	4.82
Disallowed (%)	0.00

4.3.3. Structure of the membrane-bound EHD2 oligomer

The final model of membrane-bound EHD2 is shown in Figure 37. When oligomerized and bound to membranes, EHD2 is in the closed conformation (for comparison see Figure 12). The core G domains are involved in dimerization and in oligomerization by establishing contacts with adjacent dimers. The helical domain points towards the membrane and its proximity to adjacent dimers suggest that it is also involved in oligomerization, as it has been suggested for EHD4ΔN (Melo et al., 2022). As stated in the previous section, the density was interpreted in such way that the KPF loop was occupying the hydrophobic pocket of the G domain, a conformation that is required to establish one of the oligomerization interfaces (see Section 4.3.5). Consequently, the N-terminus must not be present in the pocket in the oligomeric conformation. The hydrophobic pocket of the G domain occupied either with the KPF loop or with the N-terminus can be observed in Figure 37, panels C and D. The N-terminal residues could not be modeled in the cryo-ET

structure, likely due to the disordered nature of this stretch. Because of the reported relevance of the N-terminus in membrane binding (see sections 1.5.2.3 and 1.5.3.2 and (Shah et al., 2014)), its potential location in the cryo-ET reconstruction was further analyzed in Section 4.3.6.

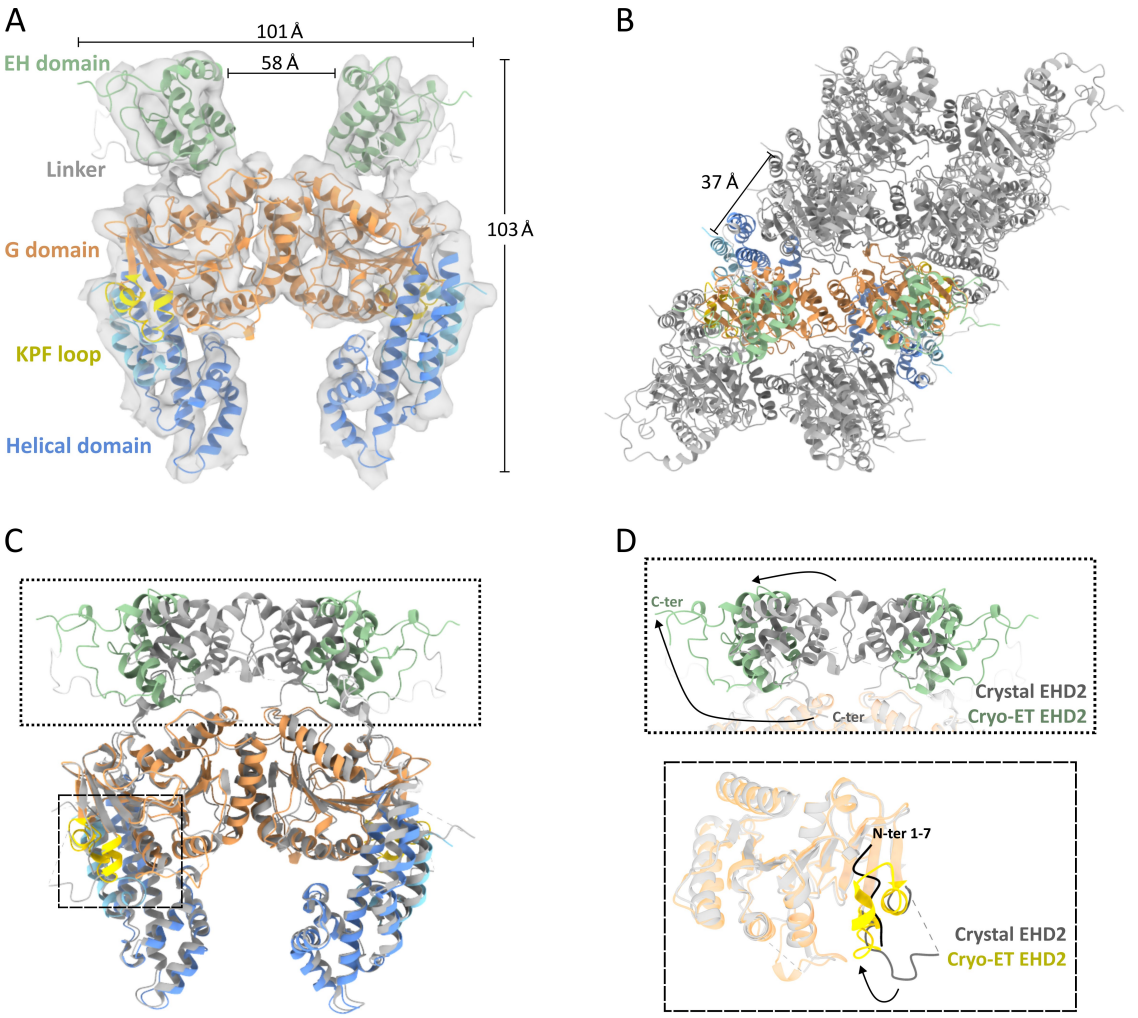

Figure 37. EHD2 model after flexible fitting and real space refinement. A) A dimer of the resulting model is shown overlaid with the density map. B) The top view of an EHD2 octamer is depicted to visualize how EHD2 dimers assemble into a filament. One dimer is colored according to the domain architecture and the rest are shown in gray. C) Overlay of the cryo-ET EHD2 structure and the crystal EHD2 structure (PDB: 4CID). Structural differences are highlighted inside the dashed squares and magnified in D. D) Top: the EH domain undergoes a sliding movement to the periphery and an 80° rotation (black arrows). Bottom: The KPF loop occupies the hydrophobic pocket in the G domain when EHD2 is oligomerized (colored cartoons). In the crystal structure (gray cartoons), the first residues of the N-terminus occupy this pocket (black cartoons). The black arrow indicates the movement of the KPF loop towards the G domain.

The disordered linker between the helical and the EH domains could not be accurately modeled either. Because of this, although the EH domains were assigned to the same molecule in the cryo-ET structure (*in cis*), it cannot be excluded that they might extend to the opposing monomer within one dimer, as modeled in the EHD2 crystal structures (PDB: 2QPT and 4CID, (Daumke et al., 2007; Shah et al., 2014), respectively), adopting an *in trans* configuration, meaning that the EH domain of one monomer sits on above the G domain of the opposing monomer. Regardless of this, a superposition of the cryo-ET structure with the crystal structure of EHD2 shows that the EH domain undergoes a large-scale movement upon oligomerization that consists of a shift towards the side of the filament and an 80º rotation (Figure 37, panels C and D). A more detailed description about the reconfiguration of the EH domain is provided in the next section.

4.3.4. The EH domains undergo a large-scale movement

In the membrane-bound oligomeric configuration of EHD2, the EH domains are shifted towards the periphery of the filament, thereby adopting a conformation in which the distance between the EH domains of one dimer is increased. Moreover, the EH domains undergo an 80º rotation (Figure 37, panels C and D). This results in the repositioning of the C-terminal tail, which no longer folds back towards the G domain, as in the EHD2 crystal structure, but it is pointing to the outside of the filament. Figure 38 shows a detailed illustration of the reorientation of the EH domain in comparison to the position described in the crystal structure of EHD2.

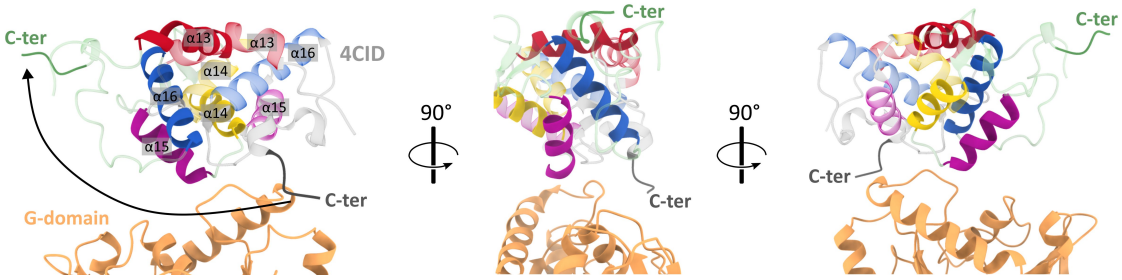

Figure 38. Movement of the EH domain. Overlay of the EH domains of one monomer of the EHD2 cryo-ET structure (green) and one monomer of the EHD2 crystal structure (gray, PDB: 4CID). The movement of the EH domain is indicated by an arrow. To illustrate the rearrangement, helices are colored. Solid colors correspond to the cryo-ET structure and transparent colors to the crystal structure. Front, side, and back views are shown in the left, middle and right panels, respectively. The G domain is shown for orientation and corresponds to the cryo-ET structure. For a better visualization, the linker is not shown.

To confidently ensure that the new configuration of the EH domain is correct, a central excised EH domain density was used to guide the flexible fitting of the EH domain crystal structure starting from 70 rotations equally distributed around a sphere. The four best scoring rotations, based on the correlation coefficient (CC) between the density map and the model (correlation coefficient = 1 = perfect fit), are in the new rotated configuration and have CCs > 0.71. These conformations fit quite accurately in the secondary structure features that are visible in the EH domain density (Figure 39, panel A). The fifth best scoring rotation corresponds to the crystal structure configuration (C-terminus towards the G domain), but its CC is <0.7 and it barely fits in the density (Figure 39, panel B).

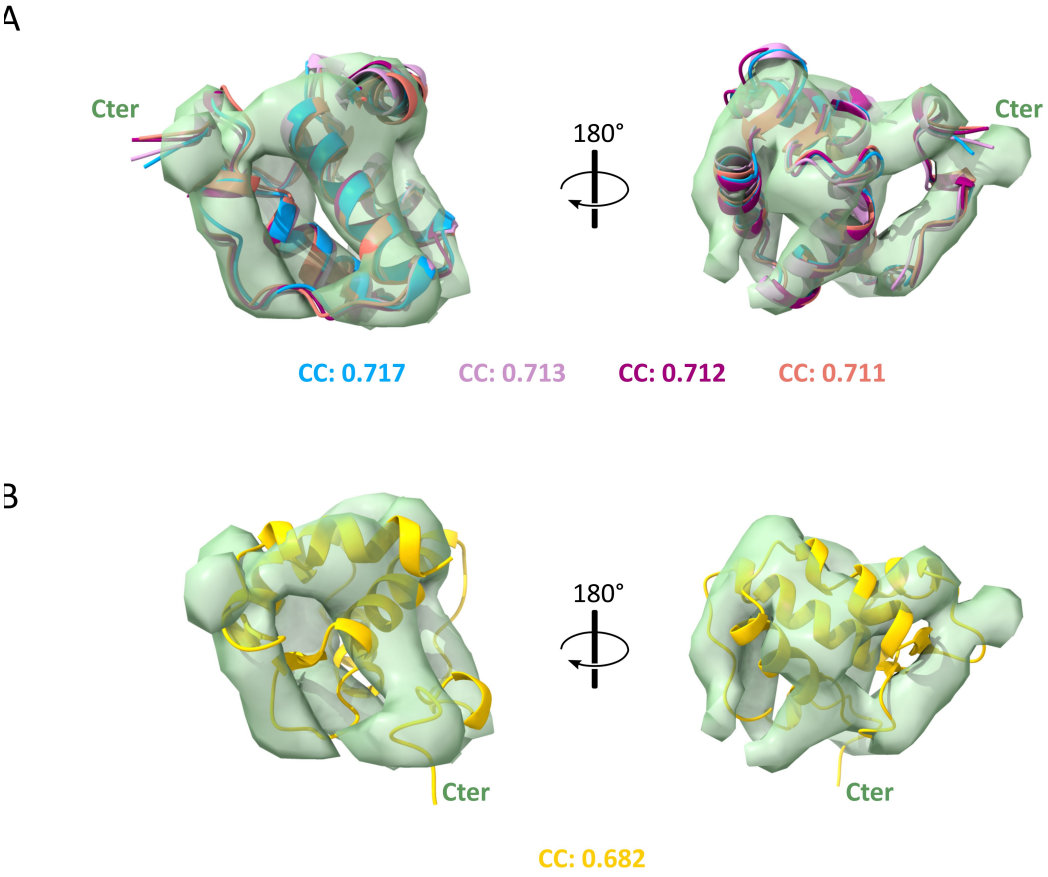

Figure 39. Flexible fitting of the EH domain. Seventy different rotations of the EH domain crystal structure were fitted in the electron density. A) The best four scoring results, based on the correlation coefficient (CC) between the map and model, are in the rotated configuration with the C-terminal tail pointing upwards and to the outside of the filament. B) The crystal structure configuration (C-terminal tail folding back to the G domain) does not fit well in the cryo-ET density. Front views are shown on the left and back views, on the right.

In addition, the new conformation of the EH domain exposes negatively charged residues to the outside (Figure 40). The surface of the EHD2 oligomeric filament is rich in negative charges at the top of the structure. These patches may now be available for electrostatic bonding with other proteins and may represent a new site of interactions between EHDs and the environment.

Another important aspect of the EH domain is the NPF-binding pocket, which has been suggested to mediate the interaction between EHD proteins and their binding partners. The reorientation of the EH domain in the cryo-ET EHD2 structure positions this pocket towards the inside of the filament, in between adjacent dimers, and is almost completely buried (Figure 41).

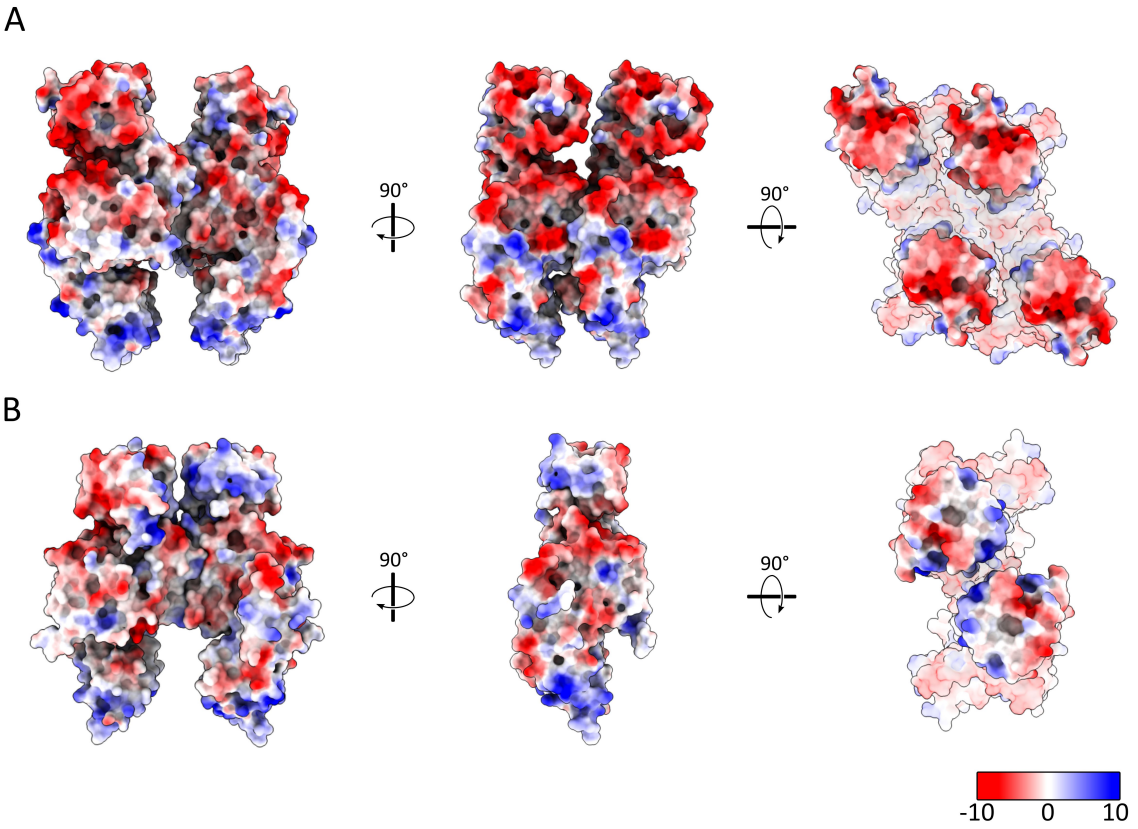

Figure 40. The reorientation of the EH domain exposes negatively charged patches. A) Electrostatic surface representation of an EHD2 tetramer (central tetramer in the filament). The new configuration of the EH domain results in a highly negatively charged surface at the top of the structure. B) The negatively charged residues from the EH domain are buried in the crystal structure of EHD2 (PDB: 4CID). Front, side, and top views are shown in the left, middle and right panels, respectively. Negative surface potential is shown in red, and positive in blue.

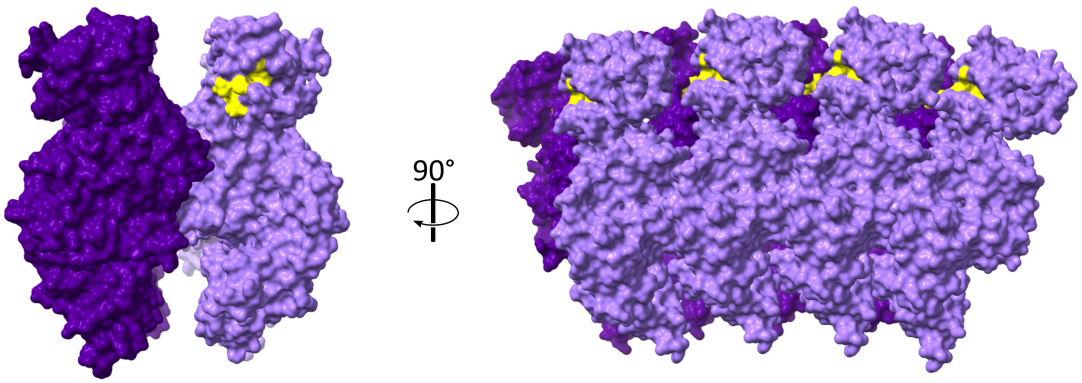

Figure 41. The NPF-binding pocket of the EH domain is facing inwards. In the new orientation of the EH domain, the pocket (in yellow) used by EHDs to interact with binding partners is facing adjacent dimers within the filament.

4.3.5. Architectural determinants of the oligomeric EHD2 assembly

Three assembly interfaces have been defined in the EHD4ΔN oligomeric structure: interface-1, which mediates dimerization, and interface-2 (KPF loop – helical domain) and interface-3 (G interface), which mediate oligomerization ((Melo et al., 2022) and see 1.5.3). These interfaces are apparent in the EHD2 oligomers, together with other contact sites which had not been described previously.

Although the resolution of the structure does not allow the accurate assignment of side chains to define interactions, favored rotamers of highly conserved residues (see Appendix E) have been chosen to promote contacts, as long as clashes were prevented (hydrogen bonds and clashes were calculated using ChimeraX and Coot). These residues and contact sites are shown in Figure 42 and described in the following.

Six different contact sites can be identified in the EHD2 filament. One of them is the dimerization interface (interface-1, according to (Melo et al., 2022)). The other five only exist in the oligomeric assembly (Figure 42). There are two potential contact sites between the G domain of one dimer and the opposing G domain of the adjacent dimer: 1) the canonical G-interface formed between the nucleotide binding pockets (Figure 42, panel A), which had already been described in the EHD4ΔN filament (Melo et al., 2022); and 2) electrostatic interactions between the switch II regions at the bottom of the G domains (Figure 42, panel B). Because the switch II regions are involved in nucleotide binding, these two contact sites define the G interface (interface-3, according to (Melo et al., 2022)). Interestingly, in the new rotated configuration, the EH and G domains of one monomer establish contacts (Figure 42, panel C). Furthermore, based on the

model used for flexible fitting (see Section 4.3.2), the KPF loop of one monomer could interact with the helical domain of the adjacent monomer forming an interface that drives oligomerization (Figure 42, panel E). This interface corresponds to interface-2 according to (Melo et al., 2022). In addition, it is likely that other contacts are formed right on top of this interface, involving the KPF loop and the G domain (Figure 42, panel D). These contacts were not described before and could represent a fourth assembly interface.

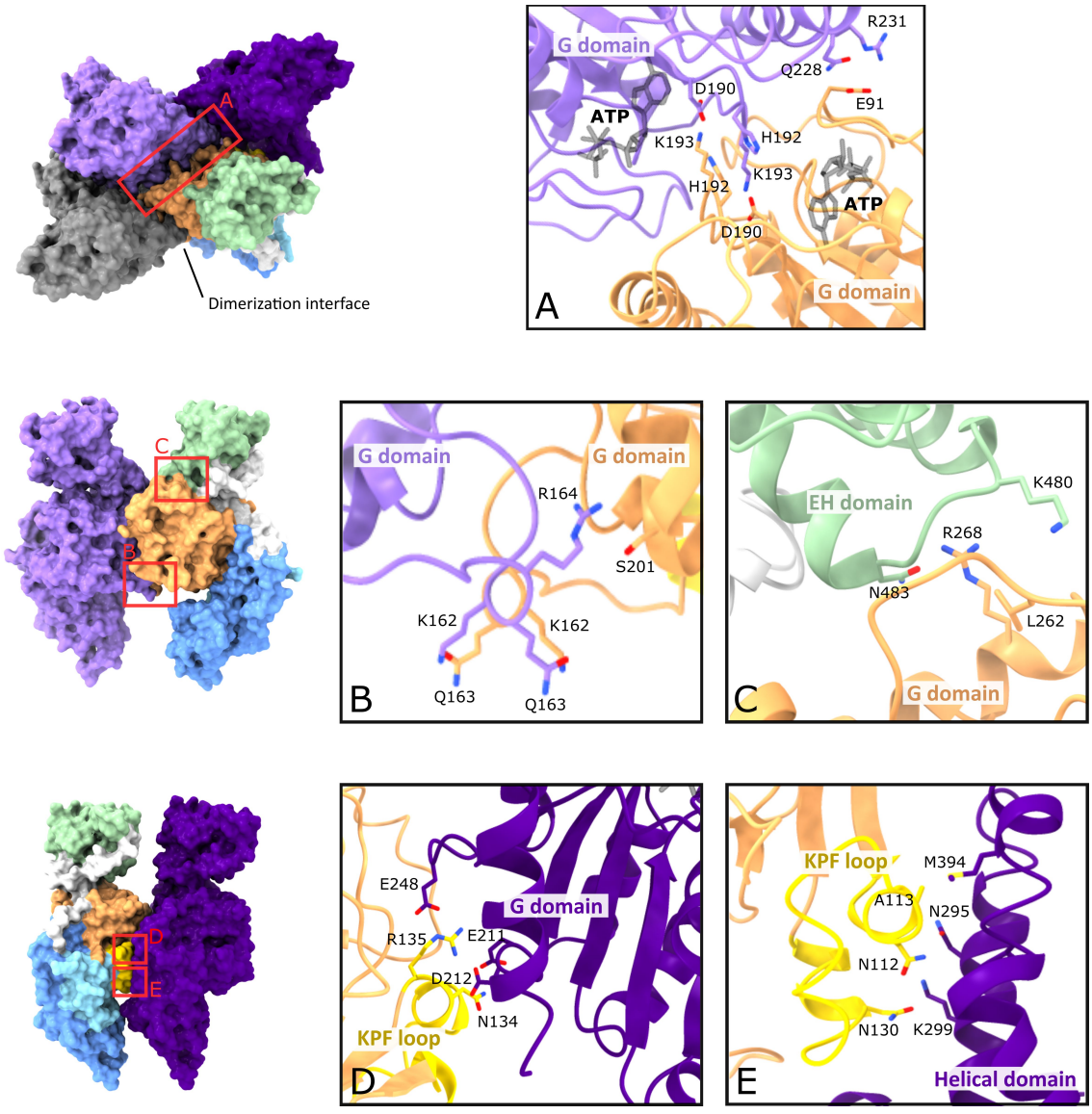

Figure 42. Architecture of the EHD2 filament. The central tetramer of the filament is displayed. In the first dimer, one monomer is colored according to the domains and the other monomer is shown in gray. The second dimer is shown in two shades of purple. There are six contact sites, including the dimerization interface (interface-1, [71]). The rotamers of highly conserved residues that might be involved in interactions have been chosen and are highlighted. A) The canonical G-interface (interface-3, [71]) between nucleotide binding pockets drives assembly. B) The switch II regions of two opposing G domains might establish electrostatic interactions (part of interface-3, [71]). C) The new configuration of the EH domain might generate contacts with the G domain directly below. D) The KPF loop could interact with the G domain of the adjacent monomer. E) Oligomerization might also be driven by contacts between the KPF loop and the helical domain of the adjacent monomer (interface-2, [71]).

4.3.6. Interaction with the lipid bilayer and generation of membrane curvature

The binding of EHD2 to membranes is mainly driven by interactions between the phospholipids and hydrophobic and positively charged residues at the tip of the helical domain (see Section 1.5.2.2). Additionally, it has been proposed that the N-terminal residues might act as a secondary membrane binding site by inserting into the lipid bilayer (Shah et al., 2014). The cryo-ET structure of full-length EHD2 reveals how the residues at the tip of the helical domain penetrate into the outer leaflet of the lipid bilayer (Figure 43). This interaction is reminiscent of a wedging mechanism which may promote the membrane remodelling activity of EHD2, resulting in the generation of both positive and negative curvature (Figure 43, panel A).

When analyzing the membrane geometry of the EHD2-coated tubules, both positive and negative membrane curvatures were evident. Positive membrane curvature was observed perpendicular to the tubule's axis and corresponds to the curvature of the membrane tubule (Figure 43, panels B and D). In addition, the membrane surface showed undulations along the tubule's axis, with the EHD2 filament sitting in the throughs of the undulations (Figure 43, panels C and E).

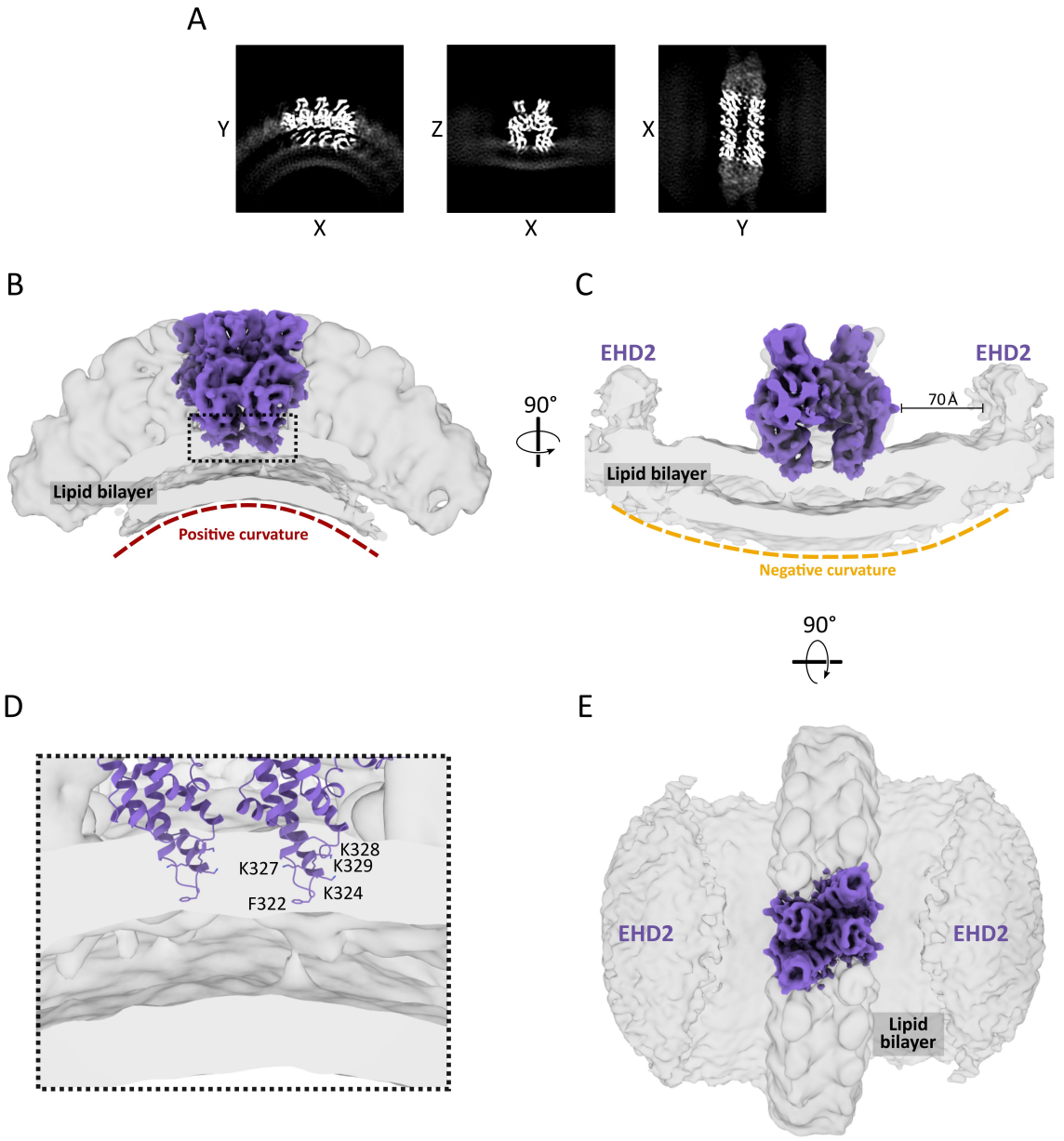

Figure 43. EHD2-coated tubules feature both positive and negative membrane curvature. A) Full 2D projections of the StA map, including the lipid bilayer. B, C, and E show 3D surface representations of the left, middle and right panels shown in A, respectively. The central tetramer is highlighted in purple. B) Side view showing the positive curvature. This curvature corresponds to the perimeter of the tubule. C) Front view showing the negative curvature of the lipid bilayer. The adjacent EHD2 filaments are indicated. D) Magnified view of the inlet highlighted in A. The tip of the helical domain inserts in the outer leaflet of the lipid bilayer. Key residues for this interaction are highlighted in one monomer. E) Top view of the EHD2 filament. The adjacent EHD2 filaments are indicated.

Altogether, EHD2 binds to liposomes *in vitro*, forms oligomers and is able to form lipid tubules, thereby generating positive curvature. EHD2 filaments constrict the membrane tubules locally – where the oligomers sit – and this results in a tubule with undulations and bulged areas in between EHD2 oligomers (Figure 44).

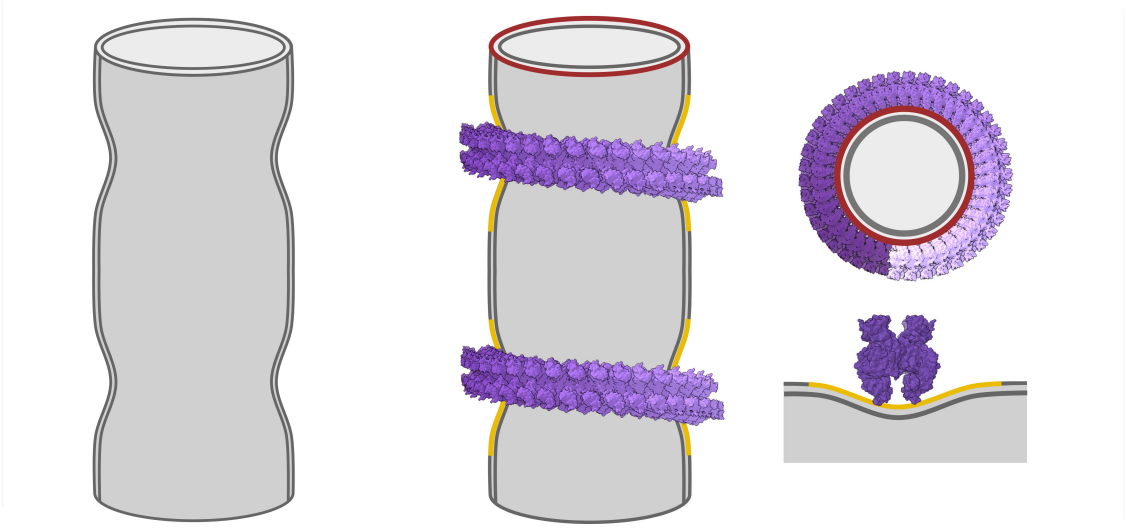

Figure 44. The *in vitro* membrane remodelling activity of EHD2 results in a lipid tubule with constrictions. Schematic representation of the lipid tubule that EHD2 generates. The positive curvature is indicated in red and the negative one in yellow. In between two EHD2 filaments, the lipid bilayer undergoes bulging.

The N-terminal residues have been proposed to constitute a secondary membrane-binding site (Shah et al., 2014). These residues could not be modeled in the cryo-ET density, indicating that they are not well defined and possibly disordered. However, when the cryo-ET map is unsharpened to highlight low-resolution features, it is possible to observe a pattern of densities that emerge directly next to the first modeled residue (Arg19) and reach towards the lipid bilayer (Figure 45). The location of this density supports that it might correspond to the N-terminal sequence stretch. Moreover, the distance of this density (measured between Arg19 and the lipid bilayer) is 28 Å, and an 18-residue peptide is long enough to cover that distance. This finding backs the hypothesis that the N-terminal region could insert into the lipid bilayer and contribute to membrane interaction.

Nevertheless, the resolution of these densities is too low to accurately model the disordered N-terminal stretch. Consequently, in an effort to better understand the role of the N-terminus in membrane binding and in oligomeric assembly, an N-terminally truncated EHD2 was used for subsequent structural investigations (see next section).

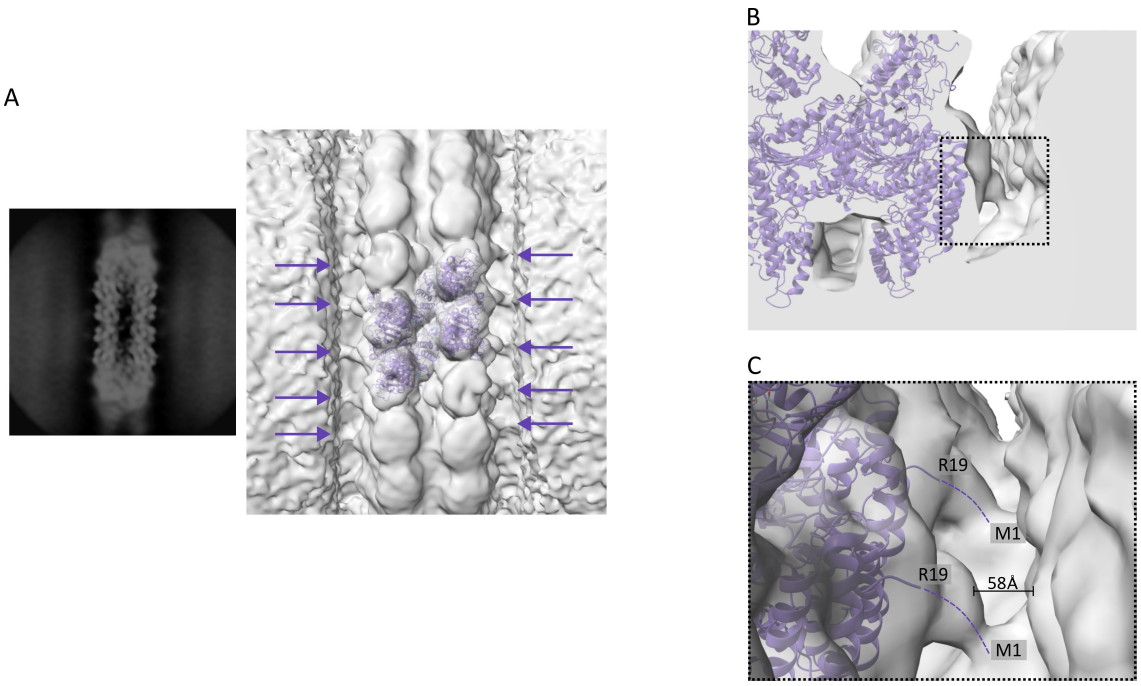

Figure 45. The N-terminal stretch might reach into the lipid bilayer. A) Top: Full 2-D projection of the Z view of the STA map, unsharpened and filtered to highlight low resolution features. Bottom: 3D surface representation, the central tetramer is overlaid. The arrows indicate the pattern of empty low-resolution densities that can be observed in an unsharpened map. B) These densities are positioned on the sides of the EHD2 filament and reach the lipid bilayer. C) Inlet highlighted in B. The dashed purple lines indicate the possible location of the disordered N-terminal residues.

4.4. The cryo-ET structure of N-terminally truncated EHD2

As extensively outlined in Section 1.5.2., the relevance of the N-terminal stretch (residues 1 – 18) of EHD2 has been previously investigated (Daumke et al., 2007; Hoernke et al., 2017; Shah et al., 2014). These residues are conserved (Figure 17, panel A and Appendix E) among different EHDs. Several studies have suggested that the N-terminal stretch is essential for membrane interaction, conformational rearrangement, and oligomeric assembly. The recently published cryo-ET structure of EHD4ΔN confirmed that, in the oligomerized membrane-bound conformation, the hydrophobic pocket of the G domain is occupied by the KPF loop and that the G domain is close towards the membrane so that the N-terminus may switch into the membrane bilayer (Melo et al., 2022). However, this study left some questions unanswered since the effect of the N-terminal truncation could not be fully assessed due to the unsuccessful expression of full-length EHD4 for comparison.

4.4.1. The absence of the N-terminus alters the overall architecture

To gain further insights into the specific role of the N-terminus in the EHD assembly and in membrane binding, an N-terminally truncated EHD2 construct (EHD2ΔN) was expressed and purified as described in Section 3.2.1 and was used for the acquisition of cryo-ET tilt series and for StA, as described in Section 3.2.5. A total of 110 tomograms were acquired and reconstructed. An initial set of 30,449 particles were manually picked along the axis of the lipid tubules and subjected to 3D alignment and averaging.

The tomograms show that EHD2ΔN can bind to liposomes and remodel them into lipid tubules forming a coat around them (Figure 46, panel A). The oligomeric arrangement noticeably differs from that of full-length EHD2. EHD2ΔN filaments seem to form helices rather than ring-like structures and they are tightly packed and in very close proximity (Figure 46, panels B and C). It is evident that the deletion of the N-terminal residues has a drastic effect in the overall oligomerization architecture, supporting the suggested role of this stretch in guaranteeing the correct assembly of EHD2.

The initial averages of the subtomograms indicate that the lipid tubules formed by EHD2ΔN are similar to the ones produced by EHD2 in terms of diameter. The luminal diameter of the tubes found in all the reconstructed tomograms falls within a range of 22 to 33 nm (Figure 46, panel C). Strikingly, EHD2ΔN can arrange into both right- and left-handed helices (Figure 46, panel C).

Due to particle heterogeneity, a subtomogram averaging workflow including a subboxing strategy was employed for structure determination.

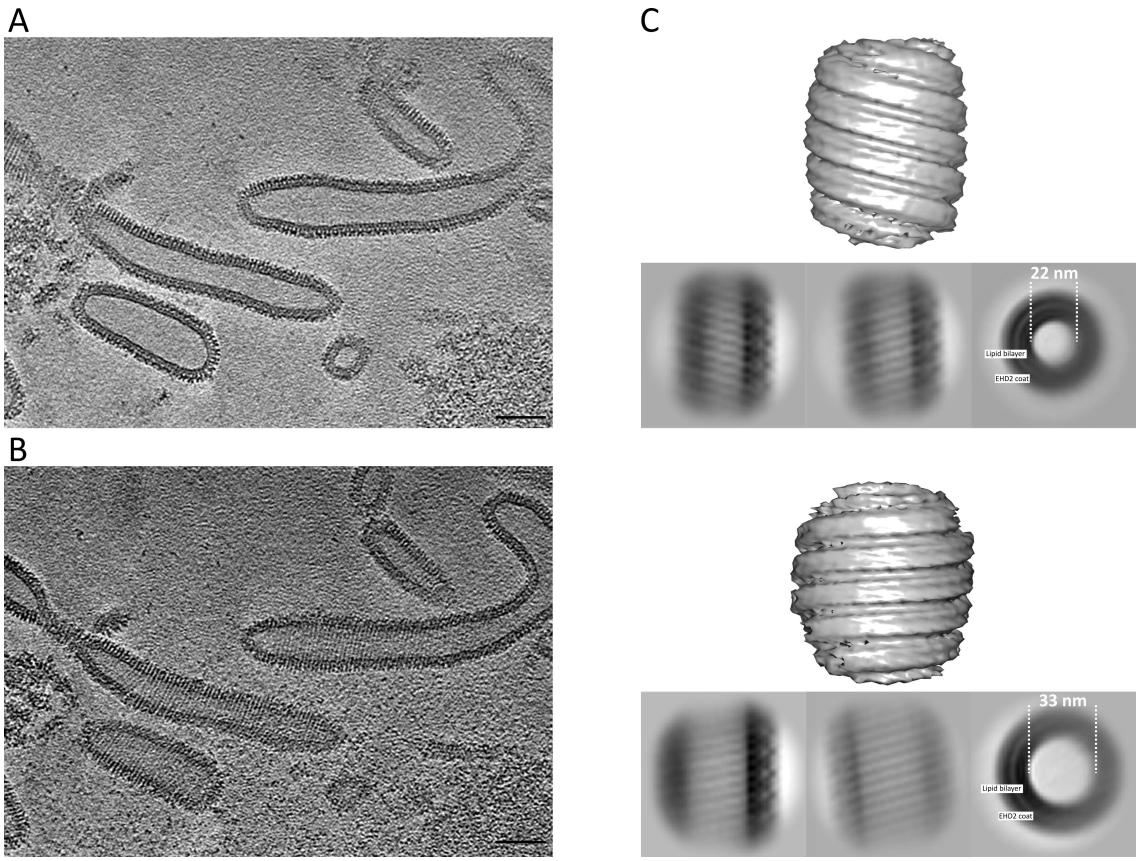

Figure 46. The deletion of the N-terminal stretch drastically affects the overall oligomeric arrangement. A) Central Z-slice of a representative tomogram showing the lumen of lipid tubules and the oligomeric EHD2ΔN coat on their surface. B) Fifteen Z-slices towards the top of the same tomogram shown in A. EHD2ΔN filaments are tightly packed. C) Full 2D projections in x, y, and z views (left, middle and right, respectively) of two different subtomogram classes. The luminal diameter range of all tubes was between 22 and 33 nm. A 3D representation of each class (X-view plane) is shown on top of the corresponding projection. EHD2ΔN filaments form both right- and left-handed helices around the lipid tubules. Scale bars: 50 nm.

4.4.2. Subtomogram averaging and flexible fitting

My collaborators Vasilii Mikirtumov and Dr. Jeffrey K. Noel carried out subtomogram averaging and flexible fitting, respectively, as described in Sections 3.2.5.3 and 3.2.5.4. A detailed description of the subtomogram averaging workflow for structure determination can be found in Appendix F. A table summarizing data collection parameters and processing values can be found in Appendix G. Briefly, after 3D classification, only one class including particles in which a full cross-section was considerably well-aligned was selected for further processing (Figure 47, panel A). Subboxing of the particles included in this class generated a set of 17,204 subtomograms containing 12 monomers. Consecutive rounds of auto-refinement, duplicate removal, and

polishing with C2 symmetry led to a 13 Å resolution map containing 8 central monomers. Local refinement and postprocessing generated a final map at an average resolution of 11 Å (Figure 47, panels B, C and D). The final result of subtomogram averaging is a cryo-EM density map of an asymmetric unit (AU) of eight monomers, forming four dimers of membrane bound EHD2ΔN (Figure 47, panels C and D). Similar to full-length EHD2, the core of the protein was solved at a higher resolution (8 – 9 Å), but more flexible areas such as the peripheral helices of the helical domains and the EH domains were solved at lower resolutions, ranging 11 - 14 Å.

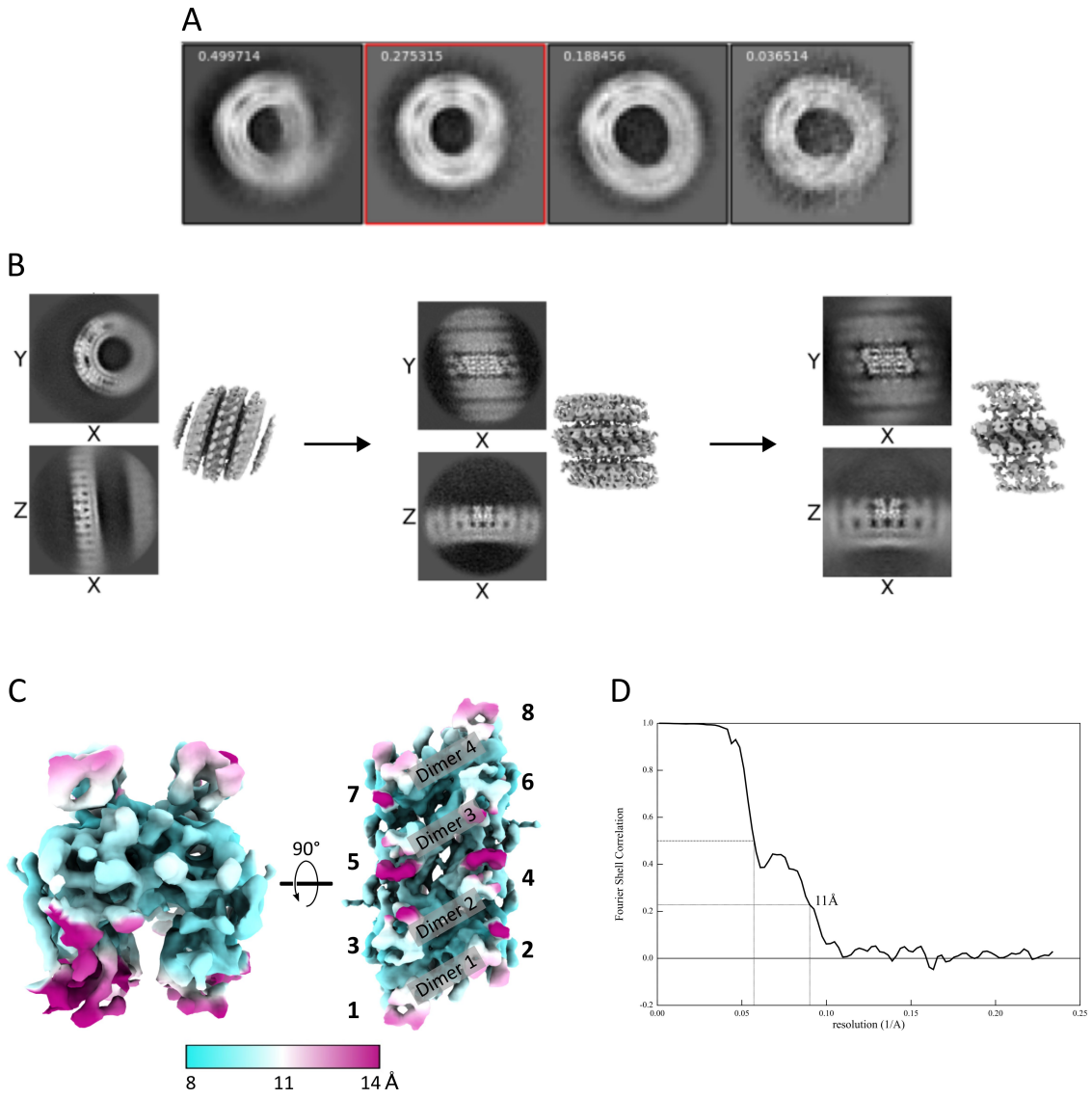

Figure 47. The 11 Å cryo-ET structure of membrane bound EHD2ΔN. A) The initial 30,449 particles were 3D classified. One class displaying a full cross-section of the lipid tubule (marked in red) was selected for further processing. B) An initial subbox including 12 EHD2 monomers was defined (left panel). Consecutive auto-refinement, duplicate removal and polishing with C2 symmetry generated a 13 Å resolution map (middle panel). Local refinement and postprocessing led to a final 11 Å resolution map (right panel). C) Front and top views of the AU resulting from subtomogram averaging and subboxing. Eight monomers (numbered) are included in the AU; four dimers are formed. The density is colored according to local resolution values. D) Fourier Shell Correlation curve.

The same flexible fitting approach as for full-length EHD2 was applied (see Section 3.2.5.4 and Section 4.3.2). After flexible fitting, the model was further refined in real space to improve the geometry, reduce molecular clashes, and validate the statistics (Table 2 and Appendix G).

Table 2. Statistics after real-space refinement.

Initial model used (PDB code)	4CID
Map sharpening *B* factor (Å^2)	-200
Model composition	
Non-hydrogen atoms	16576
Protein residues	2084
Ligands	0
R.m.s. deviations	
Bond lengths (Å)	0.002
Bond angles (°)	0.638
Validation	
MolProbity score	1.89
Clashcore	12.01
Poor rotamers (%)	0.00
Ramachandran plot	
Favored (%)	95.76
Allowed (%)	4.05
Disallowed (%)	0.19

4.4.3. Structure of the membrane-bound EHD2ΔN oligomer

The structure of N-terminally truncated EHD2 was solved at an average resolution of 11 Å. The reason behind the poorer resolution, compared to that of full-length EHD2, is the heterogeneity of the data, since not only do the tubule diameters vary, but also EHD2ΔN forms helices of different handedness. Moreover, EHD2ΔN filaments are in close proximity to each other, and this creates challenges for masking out their densities to obtain more homogenous particles. Nevertheless, the resulting density was sufficient to fit the model of N-terminally truncated EHD2 (Figure 48).

The low resolution of the structure did not allow a side-chain comparison, and overall, in the absence of the N-terminus, no major conformational changes were observed in comparison to the full-length model (Figure 48 and Figure 49, panel A). Discernible differences are in a range of 3 – 6 Å (for comparison see measured distances in panels A from Figure 37 and Figure 48).

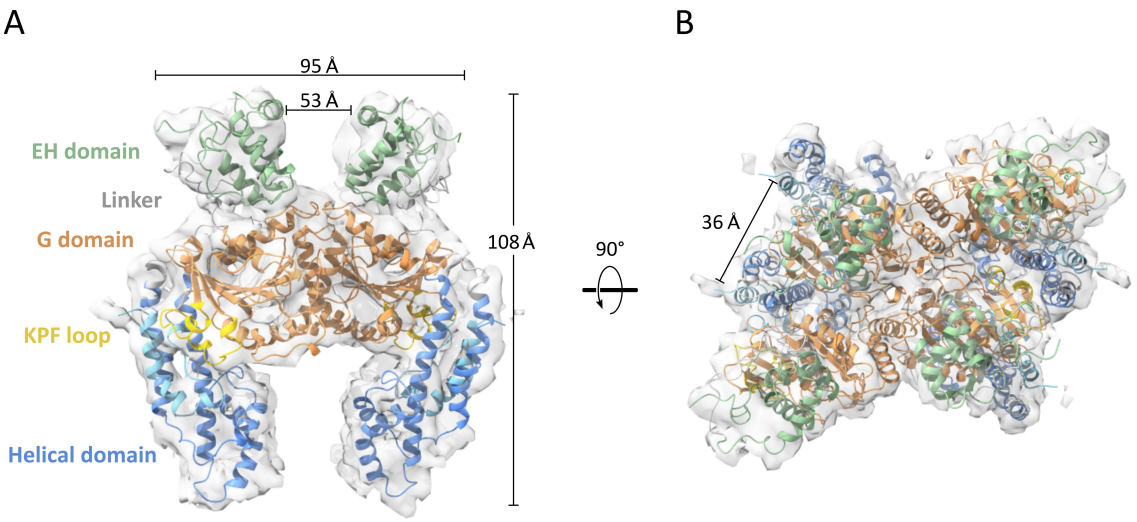

Figure 48. EHD2ΔN model after flexible fitting and real space refinement. A) A dimer of the resulting model is shown overlaid with the density map. B) Top view of the central EHD2ΔN tetramer overlaid with the density map.

In general, it seems that the EHD2ΔN filament is slightly higher than the full-length filament and that the EH domains move moderately closer to each other. This might result from the proximity of the neighboring filaments, which may be pushing the EH domains towards the inside, emphasizing the role of the N-terminus in guaranteeing proper spacing for correct architecture. Furthermore, the EHD2ΔN dimers within one filament are more tightly packed but are as curved as full-length EHD2 (Figure 49, panel B).

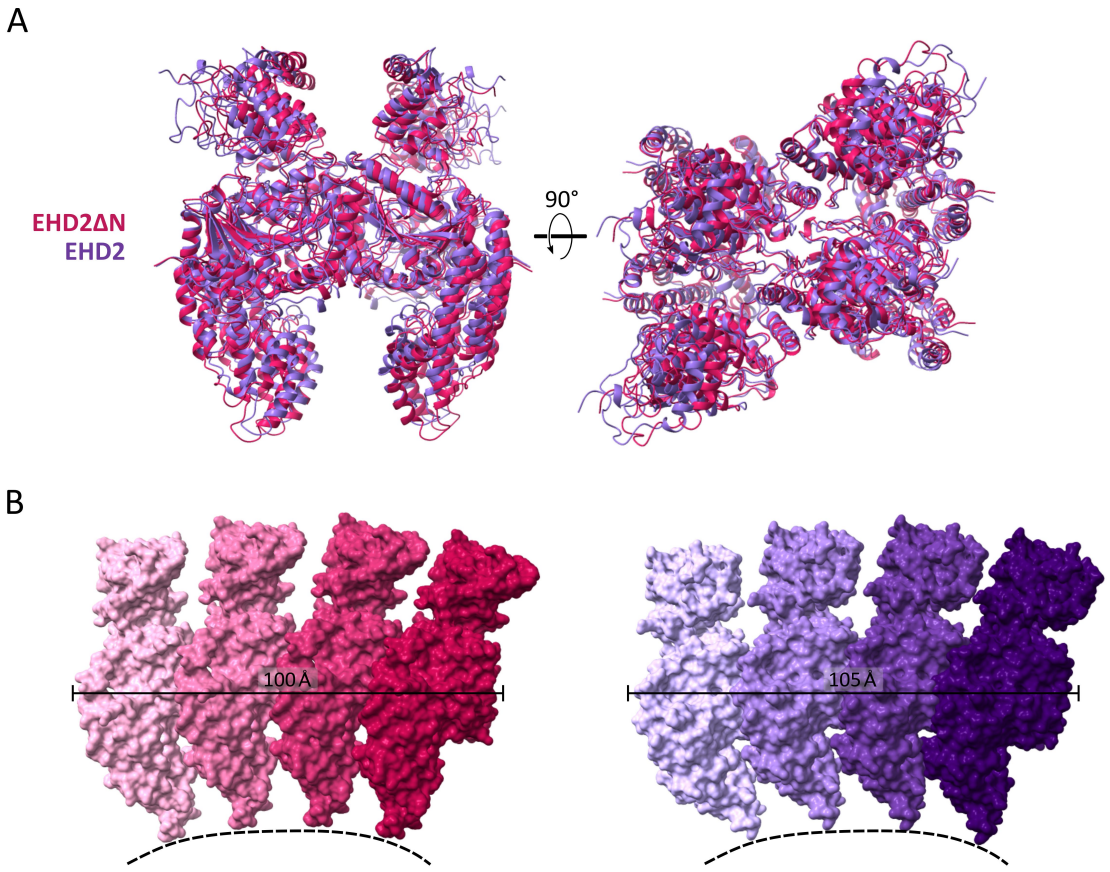

Figure 49. The deletion of the N-terminus does not alter the structure. A) Overlay of full-length EHD2 and EHD2ΔN. The structures are almost identical, observable differences are below 6 Å. B) The EHD2ΔN filament is tighter but shows the same curvature as full-length.

4.4.4. The N-terminus is responsible for negative membrane curvature

Apart from the overall arrangement around the lipid tubules, one important difference between full-length and N-terminally truncated EHD2 is the environment of the first modeled residue, Arg19. As shown in previous sections, in the full-length EHD2 filament, Arg19 is pointing down and densities where the N-terminus could potentially fit emerge from it. However, in the EHD2ΔN filament, Arg19 comes into close proximity with the neighboring filament (Figure 50).

The deletion of the N-terminal residues does not affect the tubulation activity of EHD2 and, therefore, positive membrane curvature is generated (Figure 50, panels A and B). However, the undulations observed in the lipid tubules remodeled by full-length EHD2, could not be observed in the case of EHD2ΔN tubules. In the absence of the N-terminus, the surface of the lipid tubule is flat and negative membrane curvature is not generated (Figure 50, panels A and C).

Furthermore, In the absence of the N-terminus, as shown in previous sections, EHD2ΔN filaments are in close vicinity (Figure 50, panels C, D, and E and Figure 46). EHD2ΔN, like EHD2 full-length, inserts the tip of the helical domain in the outer leaflet of the lipid bilayer (Figure 50). However, no extra density was found emerging from residue Arg19 (Figure 50, panel E). In fact, as stated above, this residue extends towards the neighboring filament (Figure 50, panels C and E). This supports the hypothesis that the densities found between Arg19 and the lipid bilayer in the EHD2 full-length map (Figure 45) must indeed correspond to the N-terminal residues.

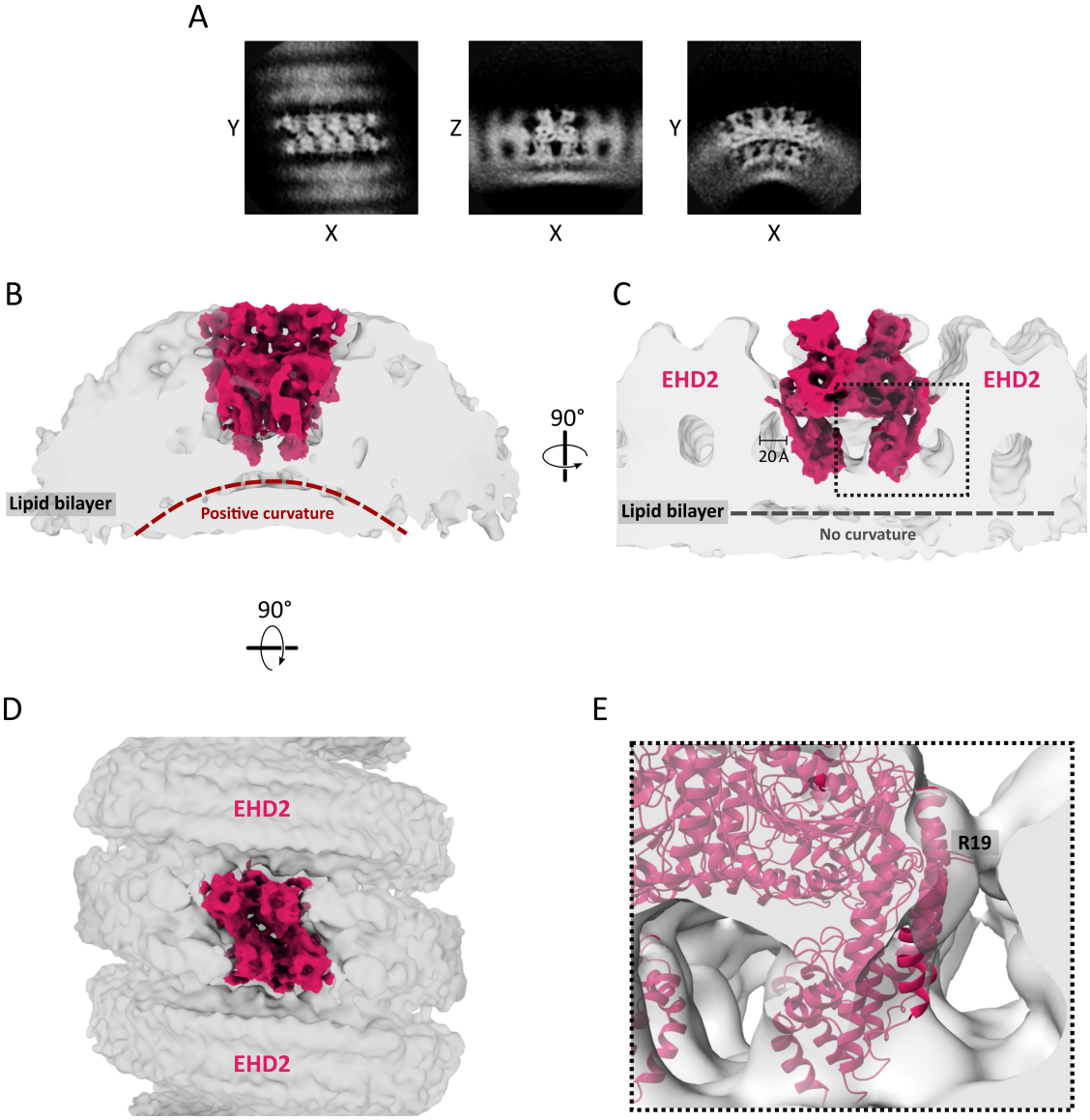

Figure 50. EHD2ΔN does not generate negative membrane curvature. A) Full 2D projections of the StA map, including the lipid bilayer. B, C, and D show 3D surface representations of the right, middle and left panels shown in A, respectively. The central tetramer is highlighted in magenta. B) Side view showing the positive curvature. This curvature corresponds to the perimeter of the tubule. C) Front view showing the absence of negative curvature. The lipid bilayer is flat and EHD2ΔN filaments are in close proximity. The adjacent EHD2 filaments are indicated. D) Top view of the EHD2ΔN filaments. E) Magnified view of the inlet highlighted in B. The tip of the helical domain inserts in the membrane and residue Arg19 is in close proximity to the neighboring filament. No extra densities were found.

In contrast to full-length EHD2, the *in vitro* remodelling activity of N-terminally truncated EHD2 results in a lipid tubule without constrictions. The surface of the tubule is flat, and the membrane does not undergo bulging. These findings are in accordance with the EHD4ΔN structure, in which negative membrane curvature as a result of constriction was not observed and filaments were close to each other (Melo et al., 2022). It can be concluded that the correct spacing of adjacent EHD2 filaments mediated by the N-terminal sequence stretch is required to generate undulations along the axis of the membrane bilayer.

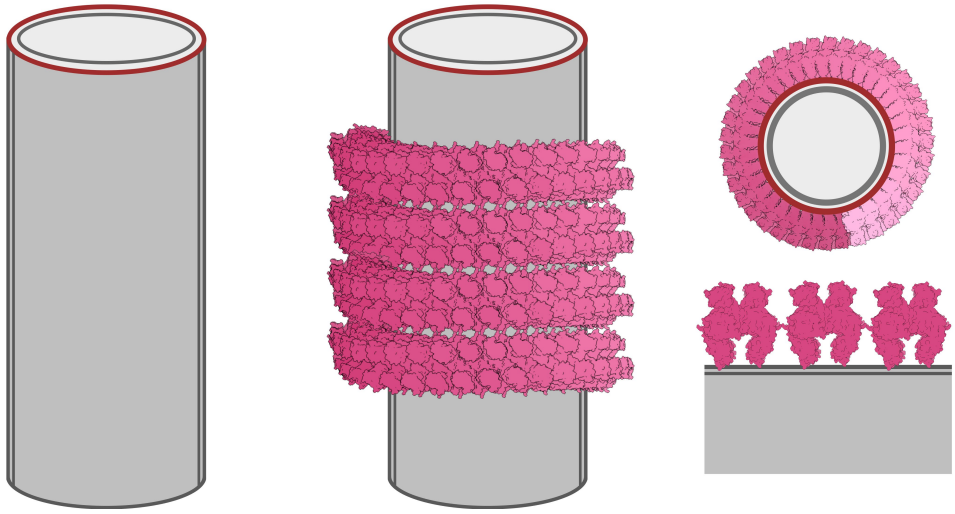

Figure 51. The membrane remodelling activity of EHD2ΔN results in a lipid tubule with a flat surface. Schematic representation of the lipid tubule that EHD2ΔN generates. The positive curvature is indicated in red. The remodelling activity of N-terminally truncated EHD2 does not generate constrictions nor bulging.

These experiments demonstrate that the N-terminus has a crucial role in guaranteeing the proper spacing of adjacent filaments. The amphipathic nature of the N-terminus may allow its interaction with the lipid bilayer, as previously reported (Shah et al., 2014), and this would result in a steric constraint for neighboring filaments to approach each other. By providing certain distancing between EHD2 oligomers, the N-terminus is indirectly responsible for the observed negative membrane curvature. In its absence, EHD2ΔN filaments are so close to each other that constriction is hindered and the undulations observed for full-length EHD2 are not formed.

4.5. New insights into the ATP hydrolysis cycle

As introduced in section 1.5.4, like other dynamin-related proteins, EHDs show a stimulated ATP hydrolysis activity in the presence of liposomes (Daumke et al., 2007; Melo et al., 2017). Previous studies have suggested that ATP binding is essential for the formation of regular EHD1, EHD2 and EHD4 oligomers since it stabilizes the G-interface thereby promoting assembly (Deo et al., 2018; Melo et al., 2017, 2022; Morén et al., 2012; Shah et al., 2014). Moreover, it is believed that membrane tubulation happens in an ATP-dependent manner (Daumke et al., 2007; Melo et al., 2017, 2022; Shah et al., 2014). Also, several authors have hypothesized that ATP hydrolysis might be required for the disassembly of the protein filament because the interfaces that drive oligomerization would weaken in the ADP-bound state (Hoernke et al., 2017; Melo et al., 2022). Nonetheless, the cycle of ATP hydrolysis in EHD proteins is still not completely understood since these studies do not provide full evidence to support the suggested models. Furthermore, different studies have demonstrated that the ATPase rates of EHD2, EHD1 and EHD4 vary considerably, pointing to mechanistic and functional differences (Daumke et al., 2007; Deo et al., 2018; Melo et al., 2017).

Consequently, the role of ATP hydrolysis was investigated to ensure a thorough understanding of the process in specific regard to EHD2 tubulation activity and oligomerization.

4.5.1. ATP hydrolysis is not required for membrane binding and remodelling

Firstly, to understand how EHD2 behaves in the nucleotide-free state, cryo-electron tomograms were acquired as described in Section 3.2.5.1 in the absence of ATP and using both the full-length and the N-terminally truncated proteins.

Strikingly, and contrary to EHD4ΔN (Melo et al., 2022), both EHD2 and EHD2ΔN in the apo state could form tight coats on the surface of liposomes and exhibit membrane tubulation activity (Figure 52). However, both constructs failed to arrange into the regular oligomeric filaments that can be observed when ATP is included in the sample (Figure 32).

Despite having undeniable effects in the oligomeric architecture and membrane interaction in the presence of ATP (see section 4.4), the truncation of the N-terminal residues in the nucleotide-free state did not result in any differences in comparison to the full-length protein.

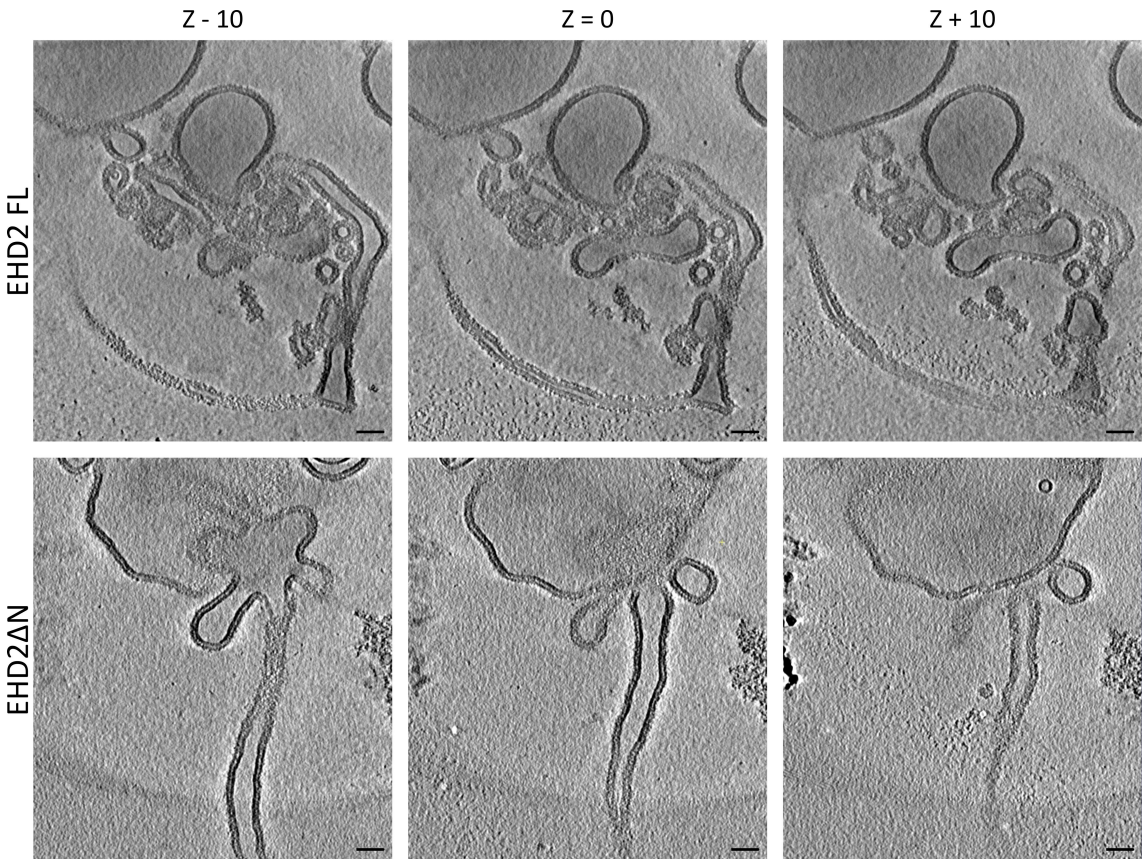

Figure 52. EHD2 and EHD2ΔN tubulates liposomes and forms coats on them in the apo state. Representative tomograms of reconstituted nucleotide-free EHD2 FL (top panels) and EHD2ΔN (bottom panels) in liposomes. The central panels show a tomographic slice (Z = 0) in which the lumen of the lipid tubule can be observed. To show that EHD2 and EHD2ΔN could not organize into regular and well-assembled filaments, other Z slices (-10 and +10) showing the surface of the lipid tubule are displayed on the left and right panels, respectively. Scale bars: 50 nm.

These data demonstrate that EHD2 can remodel membranes in the nucleotide-free state and that, in contrast to EHD4ΔN and previous models, EHD2 membrane tubulation is not ATP-dependent. Notwithstanding, as proposed for EHD4ΔN and EHD1, ATP binding appears to be fundamental for the formation of regularly organized oligomeric structures, most likely because it allows the formation of the G-interface, essential for oligomerization (see Section 4.3.5). Moreover, the idea that EHDs do not use the energy of ATP hydrolysis to remodel membranes is now further supported.

4.5.2. ATP hydrolysis is necessary for the disassembly of the protein coat

No differences were found between EHD2 and EHD2ΔN in the nucleotide-free state. To determine if these two constructs differ in terms of ATP binding and hydrolysis, the ATPase activities of EHD2 and EHD2ΔN were measured in the presence and absence of liposomes, as described in Section 3.2.2.2.

EHD2 shows a 5.5-fold stimulated ATPase activity in the presence of liposomes, as reported previously (Daumke et al., 2007). EHD2ΔN did not show stimulated ATP hydrolysis activity (Figure 53), as observed before (Shah, 2013). These results promote the idea that the N-terminal stretch is required, not only for the proper oligomerization of EHD2, but also for its correct function.

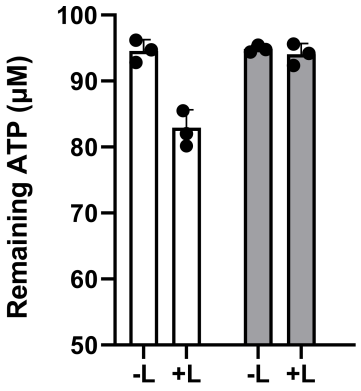

Figure 53. EHD2ΔN does not hydrolyze ATP. Bar graph showing hydrolyzed ATP after 120 min in the absence (-L) and in the presence (+L) of liposomes. Full-length EHD2 (white bars) shows a 5.5-fold stimulated ATPase activity. EHD2ΔN (gray bars) cannot hydrolyze ATP.

Taking advantage of the fact that EHD2ΔN cannot hydrolyze ATP, and to further investigate the hypothesis that ATP hydrolysis might be required for disassembly of the oligomers, cryo-electron tomograms were acquired using samples prepared as described in Section 3.2.5.1, but vitrified after a 120 min incubation.

In the case of EHD2, a large number of tubules or parts of them were found to be significantly thinner, with inner diameters ranging from 5 to 12 nm (typical diameters after 15 min incubation are 18 – 44 nm; see Section 4.2.2) or had simply collapsed (Figure 54, panel A). Moreover, many tubules either showed interrupted protein coats (increased space between EHD2 filaments) or were almost naked (Figure 54, panel A). It is worth noting that this type of lipid tubules had not been previously observed in any condition and were remarkably obvious in these sample

conditions (for comparison, see Figure 33). However, typical EHD2-coated tubules were also found, probably due to the fact that after 120 min, ATP is still present in the sample (Figure 54, panel B). As for EHD2ΔN, the lipid tubules and the protein coat remained unaltered after 120 min (Figure 54, panel C). These observations indicate that the incapacity of EHD2ΔN to hydrolyze ATP prevents the detachment of the protein coat from the surface of the lipid tubules.

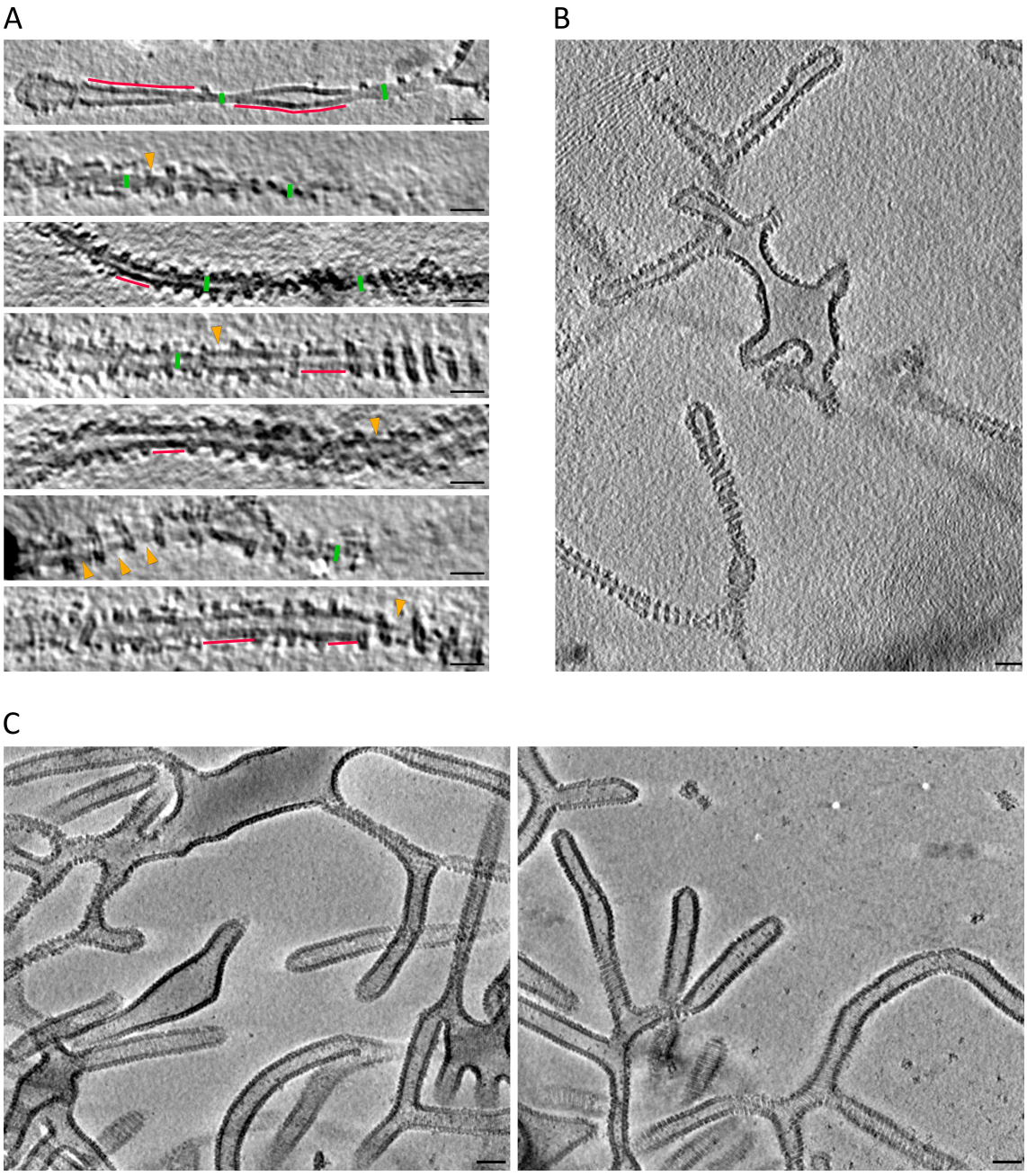

Figure 54. ATP hydrolysis may drive the disassembly of the EHD2 coat. A) Gallery of representative lipid tubules found in tomograms after incubating EHD2 with ATP and liposomes for 120 min. Central slices of the tomograms are shown so that the lumen of the tubules is visible. Many tubules were found to be much thinner or to have collapsed (a few examples are indicated by the green lines). Sometimes, increased spacing between the EHD2 oligomers was observed (a few examples are indicated by the yellow arrowheads). In some tubules, the protein coat appeared interrupted or was almost entirely absent (a few examples are indicated by the red lines). B) Central Z-slice of a

tomogram showing that typically EHD2-coated lipid tubules (like those used for cryo-ET and STA structure determination) were as well found after 120 min, as plenty of ATP still remains in the sample. C) Central Z-slices of two different tomograms acquired after incubating EHD2ΔN with ATP and liposomes for 120 min. The morphology of the lipid tubules and the architecture of the tightly packed protein coat around them remained unaltered. Scale bars: 50 nm.

These findings bolster the idea that ATP hydrolysis is necessary for the disassembly of the EHD2 coat. While EHD2 can bind to membranes and remodel them in the absence of nucleotide, the ATP-loaded state promotes appropriate oligomerization and generates stable assemblies until ATP hydrolysis, which might ultimately result in the disassembly of the oligomers.

4.6. The role of EHD2 in caveolar neck morphology

As previously outlined in Sections 1.3.2 and 1.5.1, EHD2 localizes to caveolae. Several studies have proposed that the specific localization of EHD2 at caveolae is the neck of these plasma membrane invaginations (Ludwig et al., 2013; Matthaeus et al., 2022; Morén et al., 2012; Stoeber et al., 2012). The depletion of EHD2 has been shown to result in less stable and more detached caveolae (Hubert et al., 2020; Matthaeus et al., 2020; Morén et al., 2012; Stoeber et al., 2012). Collectively, the current consensus is that the function of EHD2 is to stabilize membrane curvature, generating a restraining force that maintains caveolae at the plasma membrane, until their internalization is required. Nonetheless, mechanistic details about how EHD2 stabilizes membrane curvature and how its absence increases caveolae mobility are missing.

With the purpose of filling the gap between these structure biology findings and the published cell biology and physiology studies, caveolar morphology was examined in the presence and absence of EHD2. To accurately measure the shape of caveolae in 3D, HUVEC cells were embedded in an epoxy resin and semi-thin sections were used to collect room-temperature electron tomograms, as described in Sections 3.2.4.2 and 3.2.4.3.

Four parameters were considered to analyze caveolar morphology: 1) the width of the bulb was considered as the largest distance existing from one side to the other, 2) the width of the neck was measured at the inflection point between the neck and the bulb, 3) the length of the bulb was measured between the imaginary line where neck width was measured and the end of the bulb, and 4) the length of the neck was measured from the imaginary line where neck width was

measured to the plasma membrane, as if it was continuous and there were no invaginations. The way these distances were obtained is schematically represented in Figure 55, panel A.

In agreement with already published data, the deletion of EHD2 resulted in increased caveolae detachment since 1.5 attached caveolae were found per micrometer of plasma membrane in wild-type cells, in contrast to 0.8 attached caveolae per micrometer of plasma membrane in EHD2 knock-down cells. The amount of caveolae at the plasma membrane is reduced almost by half in the absence of EHD2.

Regarding the morphology of caveolae, the knock-down of EHD2 did not affect the shape of the bulbs since bulb length and width were not significantly different. However, the necks of caveolae in EHD2 knock-down cells were significantly narrower and vertically elongated (Figure 55, panel B).

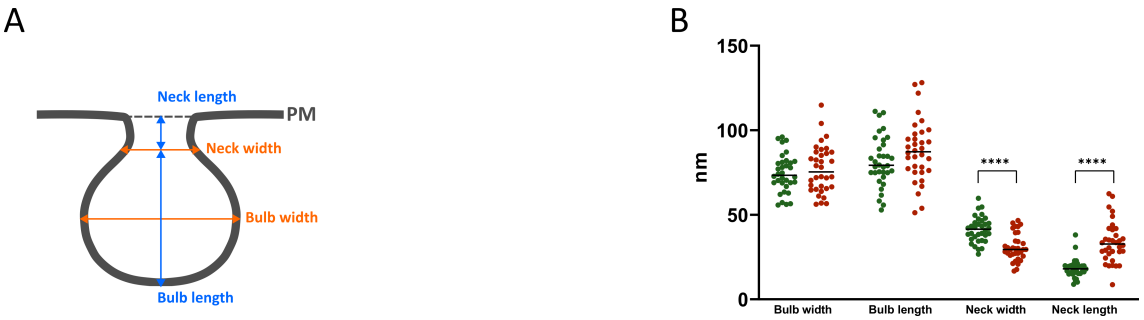

Figure 55. Analysis of caveolae morphology in the presence and absence of EHD2. A) Schematic representation of the four parameters which were measured. B) Plotted results of the measured distances shown in A. The deletion of EHD2 results in narrower and vertically elongated caveolar necks. In contrast, the bulbs of caveolae remain unaffected. Green: EHD2 wild-type cells, red: EHD2 knock-down cells. $p \leq 0.0001$****.

For a better visualization, one representative caveola, displaying average neck length and width values, was segmented in tomograms of WT and EHD2 KO cells (Figure 56). The absence of EHD2 results in an abnormal neck morphology. As proposed, these results support the idea that EHD2 serves as a scaffold that stabilizes the neck of caveolae.

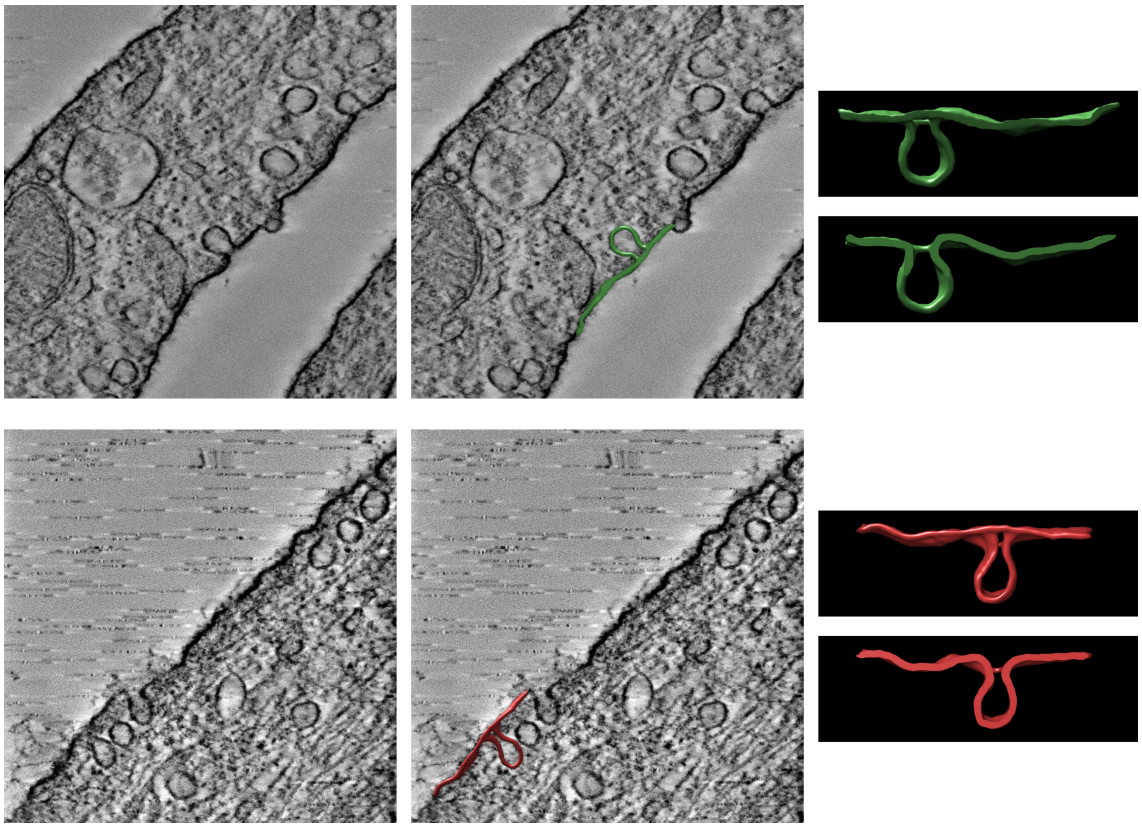

Figure 56. The absence of EHD2 results in abnormal caveolar neck morphology. For visualization purposes, an average caveola was segmented from tomograms of wild-type (green) and knock-down (red) cells. Average wild-type caveola: 41 nm neck width, 18 nm neck length. Average knock-down caveola: 30 nm neck width, 33 nm neck length.

5. Discussion

This study provides new structural and mechanistic insights about oligomerization, membrane binding and membrane remodelling in EHD proteins. Using cryo-Electron Tomography and Subtomogram Averaging, structures of membrane-bound full-length EHD2 and N-terminally truncated EHD2 were solved. The structure of EHD2 full-length at subnanometer resolution has allowed a detailed description of the molecular interfaces that drive oligomerization, as well as the architectural determinants that are required for the assembly. The comparison of this structure with that of EHD2 lacking the N-terminus, has provided a comprehensive characterization of the membrane binding mechanism of EHD2, as well as of its membrane remodelling activity. Additionally, biochemical and microscopy investigations about the ATPase activity of EHD2 support the role of ATP hydrolysis in the disassembly of the oligomer. The analysis of caveolar morphology in the absence of EHD2 highlights the important role that EHD2 plays in maintaining and stabilizing membrane curvature. Together, the findings reported in this work have deepened the structural characterization of EHD2 as a prerequisite to understand its cellular function on the neck of caveolae. These aspects are discussed in the following sections.

5.1. Oligomerization of EHD proteins

To understand the impact of the oligomeric EHD2 model described in this work, it is helpful to recapitulate structural findings obtained in the past: The first X-ray crystallography structure of EHD2 already suggested a model of how a closed EHD2 dimer assembles into oligomeric ring-like structures on membranes (Daumke et al., 2007). Although several disordered stretches, such as the N-terminal residues, the KPF loop, and the linker between the helical domain and the EH domain, could not be modeled in this structure, Daumke and colleagues proposed that oligomerization is dependent on ATP binding and that EHD2 dimers could interact with each other via the G-interface. A few years later, Morén and colleagues showed that the EH domain is not necessary for oligomerization (Morén et al., 2012). Another crystal structure of EHD2 was solved in which the first seven residues of the N-terminus were localized to a hydrophobic pocket in the G domain (Shah et al., 2014). In the same study, EPR experiments demonstrated that the N-terminal sequence stretch could insert into the lipid bilayer and serve as a secondary membrane binding site. The crystal structure of N-terminally truncated EHD4 showed that instead of the N-terminus, the hydrophobic pocket of the G domain was occupied by the KPF loop, further

supporting the idea that the N-terminus may be released from the pocket to allow membrane insertion (Melo et al., 2017). Importantly, this structure showed that EHDs can also exist in an open conformation, which was suggested to represent the active and membrane-bound configuration, while the closed conformation may represent an autoinhibited structure (Melo et al., 2017). Using infrared reflection-absorption spectroscopy, Hoernke and colleagues supported this hypothesis by showing that EHD2 oligomerizes in the open conformation on flat membranes (Hoernke et al., 2017). Briefly, the oligomerization model of EHDs at the time was based on two events: 1) EHD proteins exist in an autoinhibited and closed conformation in solution, and 2) EHD proteins adopt an active and open conformation to oligomerize on the surface of membranes (Melo et al., 2017).

Recently, the cryo-ET structure of N-terminally truncated EHD4 led to modifications of this model. Melo and colleagues found that EHD4ΔN is in the closed conformation in its oligomeric bound to membrane tubules (Melo et al., 2022). They proposed that EHD4 is recruited in the open conformation to flat membranes, where it initially oligomerizes in the open conformation, while membrane tubulation would allow the transition towards the closed conformation. This could be mediated by the insertion of a phenylalanine at the tip of the helical domain, which would promote membrane curvature via a wedging mechanism. Furthermore, the EH domains were found on top of the G domains and more distant from each other, in comparison to their position in the EHD2 crystal structures. Despite revealing these functional differences, two of the oligomerization interfaces previously proposed were corroborated: 1) the nucleotide binding pockets of two opposing G domains in adjacent dimers were facing each other, allowing the formation of the canonical G interface, and 2) the KPF loop was modeled into the hydrophobic pocket of the G domain and formed an oligomerization interface with the helical domain of the adjacent dimer. However, the low resolution of the cryo-EM map in this structure did not allow to accurately model the position of the EH domains. Moreover, because of the N-terminal truncation in the EHD4ΔN structure, it remained unclear whether the N-terminal stretch would insert into the bilayer.

In this study, cryo-ET structures of full-length and N-terminally truncated EHD2 were obtained, studied, and compared. Membrane-bound EHD2 is in the closed conformation, with the EH domains sitting on top of the G domains and assembled into oligomeric filaments via interfaces which had been previously described, namely the dimerization interface (interface-1), the interface between adjacent dimers formed between the KPF loop and the helical domain (interface-2), and the G-interface (interface-3). However, two important findings regarding the EH domain and the N-terminus have provided new insights and allowed a better understanding of oligomeric EHD2.

5.1.1. The EH domain may regulate oligomeric assembly

The subnanometer resolution of the cryo-ET map around the EH domains allowed an accurate positioning in the cryo-EM density. Compared to the closed EHD2 conformation found in the crystal structures, the EH domains undergo a shift towards the side of the oligomer, which increases the distance between them, and a rotation of 80°, which repositions the C-terminal tail towards the outside of the filament. Thus, for the first time, it is possible to deduce the displacement of the C-terminal tail in the oligomer, which in the modeled position would not be able to block the formation of the G interface. The regulatory role of the EH domain is therefore validated in the sense that its displacement upon membrane recruitment enables oligomerization via the G interface (Figure 57).

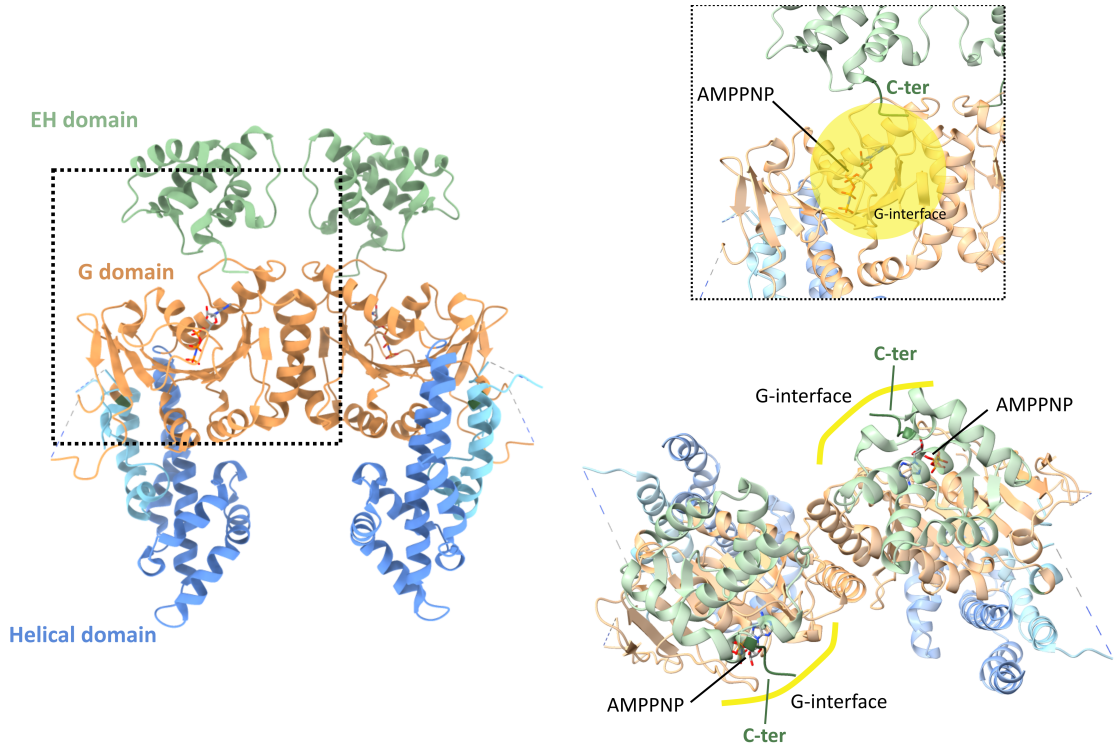

Figure 57. The crystal structure of EHD2 represents an autoinhibited conformation. The C-terminal tail of the EH domains folds back to the nucleotide pocket of the G domain in the EHD2 crystal structure (PDB: 4CID). It is likely that this orientation prevents the G-interface formation, the formation of which is fundamental in oligomerization.

In fact, in this new configuration, the EH domain may also strengthen the assembly by forming interactions with the G domain directly below. Furthermore, since the disordered loop that connects the EH domain to the helical domain is unresolved in the cryo-ET structure, the possibility that they could reach the neighboring oligomer to stabilize the overall assembly cannot be excluded. It is likely that these are essential contacts for proper architecture since the absence of the EH domain hinders the tubulation and the ATPase activities of EHD2 (Daumke et al., 2007). The EH domain might be necessary for prompting a conformation in which ATP binding and the subsequent formation of the G interface is favored and stabilized. Only in this conformation EHD2 can form organized oligomers which are, at the same time, favored by membrane curvature. This configuration allows tubulation.

Although present in the crystallized construct, the EH domains remained unresolved in the open crystal structure of EHD4ΔN and it was proposed that they are disordered (Melo et al., 2017). However, they could be resolved on top of the G domains in the closed cryo-ET structure of EHD4ΔN (Melo et al., 2022). It is possible that when EHDs are in solution (conformation represented by the crystal structure of EHD4ΔN), the EH domain adopts a (yet unknown) position that prevents oligomerization until EHDs reach the membranes, at which point the EH domain would move to the position on top of the G domains to allow assembly (conformation represented by the cryo-ET structures of EHD2, EHD2ΔN and EHD4ΔN).

Collectively, these findings confirm that the EH domain, by allowing the closed conformation and the formation of oligomerization interfaces, plays a major role in granting the assembly of EHD2 into ring-like structures capable of membrane tubulation. Although unique to EHD proteins, it appears that the EH domain could regulate oligomerization in a similar way as the PH domain in dynamin, which blocks the further assembly of tetramers in the absence of membranes (Hoernke et al., 2017; Reubold et al., 2015). A similar role in preventing oligomerization has been described for the substrate binding loop L4 of MxA (which corresponds in sequence position to the PH domain of dynamin) (Faelber et al., 2013).

Additionally, the EH domain has been proposed as the major site for interaction of EHDs partner proteins, such as EHBP1, Pacsin2, or MICAL-L1 (Giridharan et al., 2013; Guilherme et al., 2004; Senju et al., 2011). In the oligomeric filament of EHD2, the new configuration of the EH domain results in an increased negatively charged surface, which may allow EHD2 to establish electrostatic interactions in its cellular environment. To date, however, these potential interactions have not been described. The proposed binding partners of EHDs would interact merely via their NPF-motifs and the NPF-binding pocket of the EH domain (Giridharan et al., 2013; Guilherme et al., 2004; Senju et al., 2011). In the cryo-ET structure, this motif is buried within the filament, although it still may be accessible. Structural information about how EHDs and partner proteins

form complexes is lacking, and it can be speculated that when these interactions are formed, the EH domain adopts another conformation that exposes the NPF-binding pocket for binding.

5.1.2. The N-terminus may stretch to the lipid bilayer in the EHD2 oligomer

The cryo-ET structure of EHD4ΔN demonstrated that in the oligomeric membrane-bound conformation, the G domains are positioned close enough towards the membrane so that the N-terminal sequence stretch may interact with the lipid bilayer (Melo et al., 2022). However, the truncation of the N-terminal residues in this structure hindered a full understanding of how this interaction may be established. The N-terminus (residues 1 – 18) could not be accurately modeled in the cryo-ET structure of membrane-bound full-length EHD2 presented in this study, indicating that it is possibly disordered. However, a pattern of densities that emerge directly next to the first modeled residue (Arg19) and reach towards the lipid bilayer were observed in the unsharpened cryo-ET map. The location of these densities, their length, and the fact that they were not present in the cryo-ET map of N-terminally truncated EHD2, support the idea that they might correspond to the N-terminal sequence stretch, in accordance with the hypothesis that this region contributes to membrane binding. Due to the relevance found for the N-terminus in membrane interaction and remodelling, the main findings concerning these residues are discussed below, in Section 5.2.

In the context of the oligomerization mechanism discussed in this section, it is important to point out that these results corroborate that, upon membrane binding and recruitment, the N-terminus of EHD2 may be released from the hydrophobic pocket of the G domain, which in turn would become occupied by the KPF loop, and stretch towards the lipid bilayer, as proposed by Melo and colleagues for EHD4ΔN (Melo et al., 2017, 2022). To date, there is no information about the open structure of EHD2. Assuming that in the open conformation in solution, EHD2 would closely resemble the open crystal structure of ATPγS-bound EHD4ΔN (PDB: 5MTV and 5MVF (ADP-bound, identical), (Melo et al., 2017)), the KPF loop would be found in the hydrophobic pocket of the G domain both in the open EHD2 dimer and in the closed EHD2 oligomer. If this were the case, it would be important to determine when the N-terminal stretch is occupying the hydrophobic pocket of the G domain. As proposed, it is likely that the crystal open crystal structure of EHD4ΔN represents a close-to-oligomeric state, favored and stabilized by the crystal contacts (Melo et al., 2017). The N-terminus might occupy the hydrophobic pocket of the G domain in yet another state in solution, one that is previous to the open oligomeric-prone conformation (represented by the crystal structure of EHD4ΔN), and that might be achieved again after hydrolysis and disengagement from membranes. Further investigations using X-ray crystallography and/or cryo-Electron Microscopy and Single Particle Analysis (SPA) to determine

the open structure of EHD2 are necessary to fully characterize the domain rearrangements that lead to the open and closed conformations.

Apart from the structural characterization of the open conformation of EHD2, another remaining question to be answered is understanding at which stage EHD2 undergoes the conformational change and whether it arrives to the membrane as open dimers and rapidly closes to start oligomerizing, or whether its architecture is modified in solution. The first hypothesis is in accordance with previously published data (Hoernke et al., 2017; Melo et al., 2017, 2022), but in the tomograms presented in this work, EHD2 was always found forming short oligomeric filaments on lipid bilayers, regardless of their curvature degree. In all types of oligomeric filaments, EHD2 is in a clear closed conformation, resembling the shape of the letter H (for an example see Figure 32). It is likely that the movement from the open to the closed conformation happens rapidly and, therefore, it cannot be captured in the tomograms. Other experimental techniques that allow addressing this type of dynamic rearrangements are required to fully understand this mechanism and place it in spatial and temporal context.

5.1.3. Comparison to oligomerization in other dynamin-related proteins

One common feature of members from the dynamin family of proteins is their ability to oligomerize by forming regular assemblies in the form of helical or ring-like structures. Similarities but also fundamental differences in the oligomerization mechanism of EHDs and other dynamins have been described previously (Daumke & Praefcke, 2016; Faelber et al., 2013; Melo et al., 2022), and have become more evident in this study. The formation of oligomeric filaments in dynamin, Drp1, MxA and Mgm1 is mediated by three interfaces which involve the stalk (within dimers and between neighboring dimers). Additionally, the G domain contributes as by mediating contacts between adjacent filaments (Daumke & Praefcke, 2016; Faelber et al., 2013; Melo et al., 2022). In contrast, the nucleotide-dependent interface in EHDs is oriented along the filament. In fact, the G domain of EHDs is the main structural element for assembly: it mediates dimerization and oligomerization via two interfaces, the G interface formed between the nucleotide binding pockets of adjacent dimers, and the interface between the KPF loop and the helical between dimers. Moreover, this study has postulated new potential interactions mediated by the G domain: 1) contacts between the G domain and the EH domain from the same monomer, 2) contacts between the switch II regions of two opposing G domains, and 3) contacts between the KPF loop and the G domain of the neighboring dimer. However, these interactions cannot be demonstrated without structural studies at higher resolution that allow an accurate modelling of side chains.

Another fundamental difference is that, while the pitch in dynamin-related protein is fixed, the architecture of EHDs allows reorientation and adaptation of the filament depending on the curvature of the underlying membrane, as shown for EHD4ΔN and in this study.

In this work, the regulatory function of the EH domain has been demonstrated. Its position in the membrane-bound assembly is crucial to allow the formation of the aforementioned interfaces, and it sems it may work as an autoinhibitory element by preventing oligomerization when EHDs are in solution. A similar regulatory mechanism has been described for dynamin and MxA (discussed above in Section 5.1.1).

Importantly, although members of the dynamin family undergo conformational changes that result in open or closed configurations, it seems that in EHDs, this rearrangement is driven by the interaction with curved membranes, whereas it is GTP hydrolysis (the power stroke) what drives the transition between the two states in dynamin and related proteins.

5.2. Membrane binding and remodelling in EHDs

Cellular membranes are highly dynamic, and they adopt a large spectrum of various shapes. Membrane shaping can derive from simple deformations of existing shapes or from membrane remodelling activities, which involve fission or fusion (Campelo et al., 2010). Shape transitions, membrane compartmentalization, and the recruitment and participation of proteins in these events are highly regulated processes (Campelo et al., 2010; Kozlov & Taraska, 2023).

Earlier studies showed that EHDs interact with the lipid bilayer by electrostatic and hydrophobic interactions between the residues at the tip of the helical domain and the phospholipids of the membrane (Daumke et al., 2007; Melo et al., 2017; Morén et al., 2012; Shah et al., 2014). The N-terminal stretch was proposed to act as a secondary membrane binding site (Melo et al., 2017, 2022; Shah et al., 2014). Although their cellular localizations vary, all four mammalian EHDs have been shown to remodel membranes and generate tubules (Bahl et al., 2016; Daumke et al., 2007; Deo et al., 2018; Melo et al., 2017).

Here, the cryo-ET structure of full-length EHD2 has provided a better understanding of membrane binding and remodelling in EHDs. EHD2 tubulates liposomes *in vitro* and forms ring-like oligomers around them. The tubulation activity implies that EHD2 has the ability to generate positive membrane curvature. Additionally, it was shown that EHD2 oligomers constrict the lipid tubule and, in consequence, induce undulations of the membrane surface along the tubule's axis.

This results in local negative membrane curvature and membrane bulging between EHD2 filaments (Figure 58, panel A). Indeed, the coexistence of negative and positive membrane curvature resembles the membrane shape found at the neck of caveolae (Kozlov & Taraska, 2023; Parton, Kozlov, et al., 2020) (Figure 58, panel A and Figure 60). The model suggested by Daumke and colleagues, based on their crystallographic and biochemical analysis, already predicted that EHD2 would induce local curvature on the lipid tubule (Daumke et al., 2007). This model was corroborated by Campelo *et al.* using physical and computational models of the cell membranes (Campelo et al., 2010). However, the model was likely incorrect regarding the position of EHD2 oligomers, as they were proposed to sit on the positively bent side of the bilayer undulations (Figure 58, panel B). The membrane-bound structure presented in this thesis contradicts the previous model by showing that EHD2 rests on the negatively bent areas.

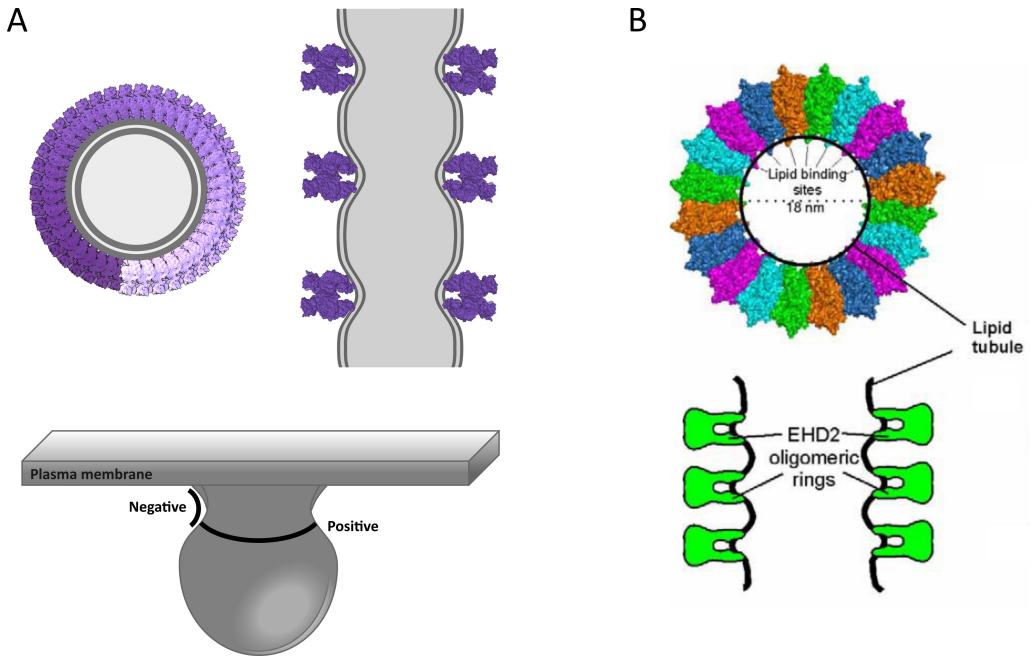

Figure 58. Comparison between the model proposed in this thesis and the previous one. A) The cryo-ET structure of EHD2 revealed that it generates positive and negative membrane curvature. EHD2 oligomers rest at negatively bent areas. The membrane may undergo bulging between EHD2 filaments. The shape of the caveolar neck, where EHD2 localizes, possesses both types of curvatures. B) Previous model describing EHD2 membrane remodelling. Figure modified from (Daumke et al., 2007).

Membrane buckling and undulations on the outer membrane layer were observed in the cryo-ET reconstruction of EHD4ΔN. These undulations appeared between filaments and between the helical domains of one dimer (Melo et al., 2022). Furthermore, in contrast to the cryo-ET structure of full-length EHD2, no constriction was observed in the cryo-ET reconstruction of EHD4ΔN (Melo et al., 2022). The cryo-ET structure of N-terminally truncated EHD2 shows that the deletion of this stretch hinders constriction and bulging, and the resulting negative membrane curvature. The work presented in this thesis, taken together with the observations withdrawn from the cryo-ET structure of EHD4ΔN, corroborate that the N-terminus may be directly involved in membrane binding and, indirectly, in membrane remodelling.

The involvement of the N-terminus in membrane binding had been previously proposed (Melo et al., 2017, 2022; Shah et al., 2014) but due to its disordered nature, there was no structural evidence to prove this hypothesis. Here, the comparison between the cryo-ET maps of full-length and N-terminally truncated EHD2 called attention to low-resolution densities, only present in the EHD2 FL map, which emerge from Arg19 and reach the lipid bilayer. Although the disordered N-terminus cannot be modeled in these densities, it is likely localized there, supporting its proposed insertion in the bilayer and implication in membrane remodelling. Moreover, the N-terminus plays a role in the overall oligomeric architecture of EHD2. Its absence, as already seen previously (Shah et al., 2014), allows EHD2 filaments to be tightly packed and in very close proximity. Based on the structures presented in this study, it is possible to postulate the N-terminal stretch as a spacer that maintains adequate distancing between filaments and a correct organization that allows constriction, maybe also by establishing contacts with the neighboring EHD2 oligomer. In its absence, EHD2 filaments are so close to each other that constriction is prevented and negative membrane curvature cannot occur. The role of the N-terminus in the overall architecture appears to be crucial since, moreover, its deletion hinders the ATPase activity of EHD2, probably due to an unfavored conformation for hydrolysis (see Section 5.3).

Local curvature on the surface of lipid tubules based on constriction and bulging was also described for EHD1 using membrane templates and fluorescence microscopy, together with molecular dynamics (Deo et al., 2018). Deo and colleagues proposed that EHD1 filaments are positioned on the dome of the bulged membrane, opposite to the EHD2 model suggested in this work. While this may be true for EHD1, due to the different cellular localizations and functions of EHD paralogs, the position of the EHD1 oligomer with regard to membrane curvature can only be evaluated with structural investigations, and this information is still lacking. Nevertheless, this study is in agreement with the relevance of the N-terminus in EHD architecture stated above. The authors found residues 2-9 to confer stability to the protein scaffold and to be involved in the remodelling activity of EHD1. Moreover, the deletion of these residues prevented the phenotype rescue in endocytic recycling defects in EHD1 knock-out experiments (Deo et al., 2018).

This proposed mechanism is not unique to EHDs, as it is well-known that the insertion of amphipathic residues in the lipid bilayer drives membrane reshaping (Bhatia et al., 2010; Kozlov & Taraska, 2023). Cases of amphipathic N-terminal helices or stretches involved in membrane remodelling are widely documented in the literature. For example, amphipathic N-terminal stretches known to induce curvature in membranes were described for the small GTPases Sar1 (Hutchings et al., 2018; Joiner & Fromme, 2021) and Arf1 (Antonny et al., 1997; Hooy et al., 2022). Moreover, the N-terminus of EHD2 could also work in a similar way as ALPS motifs (Amphipathic Lipid Packing Sensor motifs), which sense defects in lipid packing that arise from membrane bending and produce minor insertions (Vanni et al., 2013). According to the findings presented here, the membrane binding and remodelling activity of EHD proteins results from the synergy between two events on the lipid bilayer: the insertion of the tip of the helical domain and the insertion of the N-terminal stretch.

Furthermore, it was described that the result of EHD1 bulging are thinned membrane regions which may ultimately undergo scission. In comparison to EHD2, the stimulated ATPase activity of EHD1 was found to be 40-fold higher than that of EHD2, which exhibited a significant delay in membrane remodelling, under the same experimental conditions (Deo et al., 2018). EHD2 activity did not result in fission in any case (Deo et al., 2018). These results highlight fundamental differences between EHD paralogs, probably resulting from their different cellular localizations. In fact, the cryo-ET structure of EHD4ΔN, and the structures of EHD2 and EHD2ΔN presented in this study demonstrate how EHD filaments can adapt to different degrees of curvature (Figure 59).

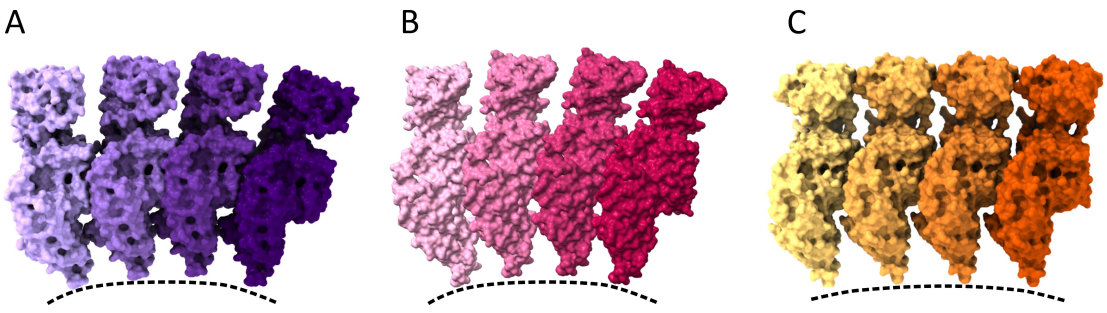

Figure 59. EHD2 and EHD2ΔN filaments are more curved than EHD4ΔN. A) Side view of an EHD2 octamer. B) Side view of an EHD2ΔN octamer. C) Side view of an EHD4ΔN octamer (PDB: 7SOX, (Melo et al., 2022)). The oligomers are shown as surface representations. The dashed lines indicate the curvature of the filaments.

This flexibility, together with differences in the ATP hydrolysis activity and the specificity for certain lipids, might explain how different EHDs are recruited to cellular membranes of varying curvature and how they have evolved to carry out specialized functions. *In situ* structural studies, in combination with co-localization and super-resolution fluorescence microscopy experiments, are necessary to fully comprehend the architecture of EHDs in their cellular context.

5.2.1. A comparison to mechanisms of membrane remodelling

As introduced in Section 1.1.1, in general, shape transformations of membranes can be divided into two classes: 1) reshaping is due to distortions of the membrane continuity and reconnections of its surface, and 2) the change in membrane shape results from bending and does not require disruptions nor re-connections of the membrane (Campelo et al., 2010).

The first class refers to fission and fusion activities, which topologically transform the membrane. Several proteins of the dynamin family belong to this class and they achieve membrane reshaping via different mechanisms. The PH domain drives membrane binding in dynamin by inserting a variable loop (Faelber et al., 2011; Kong et al., 2018) and the paddle domain in Mgm1/OPA1 has been described to function in a similar manner (Faelber et al., 2019). MxA possesses an unstructured loop at the same position as the PH domain in dynamin. This loop mediates membrane interaction (Von Der Malsburg et al., 2011). BDLP inserts a hydrophobic region at the tip of the helical domain as a hairpin (Low et al., 2009). Atlastins achieve remodelling using transmembrane regions (Byrnes et al., 2013). Membrane deformation carried out by these proteins results mainly in fusion or fission. The membrane remodelling activity of EHDs is fundamentally different and they seem to rather bend membranes and stabilize the generated curvature.

Consequently, EHDs may belong to the second class of membrane deformation mentioned above, which includes activities like flattening, tubulating, or squeezing. Despite exhibiting different configurations, modes of action and localization, the deforming activity of proteins that belong to this class results in common bending geometries. For example, the tubules of the peripheral ER, T-tubular extensions of plasma membranes, elongated fragments of transport intermediates, and protrusions of the plasma membrane, have cylindrical shapes of 30-100 nm cross-sectional radii (Kozlov & Taraska, 2023). These values are similar to those found for EHD4, in accordance to its proposed localization to large endosomes and low curved membranes (Melo et al., 2022). The radii of the tubules generated by EHD2 (this study and (Daumke et al., 2007)) and EHD1 (Deo et al., 2018) are smaller, like in the case of the sheets of rough ER, the thylakoidal membranes, phagophore structures or the mitochondrial cristae, which range 10-50 nm (Kozlov & Taraska, 2023).

The reason why such different membranes, deformed by very diverse and distant proteins, end up sharing a common geometry is due to the fact that membrane bending mechanisms are only a few and are conserved (Campelo et al., 2010; Kozlov & Taraska, 2023) (see Section 1.1.1). To summarize, EHD2 remodels the membrane by employing two of the universal mechanisms of membrane bending: it functions as a scaffolding protein by establishing electrostatic interactions between the positively charged residues at the tip of the helical domain and the phospholipids, and the amphipathic N-terminal residues of EHD2, together with the hydrophobic Phe322 at the tip of the helical domain mediate hydrophobic insertion.

5.3. ATP binding and hydrolysis in EHD proteins

EHD proteins bind and hydrolyze ATP to ADP. Like for other dynamin-related proteins, ATP hydrolysis is stimulated by membrane binding. The ATPase activity in EHDs is fundamental for their function. For example, ATP binding and hydrolysis is essential for the role of EHD1 in mediating cargo recycling from the endocytic recycling compartment (Deo et al., 2018). A hydrolysis deficient EHD2 generates distorted caveolae and an ATP-binding mutation renders EHD2 completely cytoplasmatic (Morén et al., 2012; Stoeber et al., 2012).

For a while, it remained uncertain whether EHDs use the energy from ATP hydrolysis for shaping membranes, akin to the GTP hydrolysis power stroke used by other dynamin family members. Nonetheless, to date, it is clear that EHD proteins function in a different manner (Daumke et al., 2007; Melo et al., 2022). The proposed roles of ATP binding and hydrolysis in oligomerization, membrane deformation and filament disassembly are discussed below.

This study confirms that oligomerization is dependent on ATP binding. In the nucleotide-free state, EHD2 bound to lipid bilayers but failed to form organized ring-like structures. The ATP-loaded state is probably required for the formation of the G-interface and the stabilization of the KPF loop in the hydrophobic pocket of the G domain, two events necessary for stable self-assembly. Studies performed with EHD1 (Deo et al., 2018) and EHD4 (Melo et al., 2022) reached the same conclusion. However, EHD2 in the apo state did not lose its ability to deform liposomes into tubules, an observation which had already been made, as well as for ADP-bound EHD2 (Daumke et al., 2007). In contrast, in the recently published study about the cryo-ET structure of EHD4ΔN, Melo and colleagues claim that EHD4ΔN cannot tubulate liposomes in the apo state. The findings presented here demonstrate for EHD2 that this is not due to the absence of the N-terminal residues since nucleotide-free EHD2ΔN exhibits tubulation capacity. The work carried

out for EHD1 is not conclusive about an ATP-dependent membrane tubulation activity since the authors used tubular model membranes instead of liposomes for their investigations (Deo et al., 2018). The fact that apo EHD2 tubulates and EHD4ΔN does not may be simply explained by the different curvature preferences of the two EHD paralogs, with EHD2 filaments preferring higher and EHD4 filaments lower membrane curvature. In fact, EHDs hydrolyze ATP at markedly different rates. The stimulated ATPase activity of EHD1 is 40-fold higher than that of EHD2 under the same experimental conditions (Deo et al., 2018). Although there is no data for full-length EHD4, EHD4ΔN shows stimulated ATP hydrolysis at a seven-fold higher rate than that of EHD2 (Melo et al., 2017). The different ATPase rates highlight that EHD2 is a very slow ATPase compared to its paralogs. Indeed, the stimulated ATP hydrolysis activity of EHD2 is only 8-fold higher compared to its basal activity. This is probably due to the different membrane shaping activities that EHDs have. For instance, EHD1 has been proposed to remodel the membrane causing scission (Deo et al., 2018), whereas membrane fission was not found in the same study for EHD2 and has not been described for EHD4.

The work presented here shows that the deletion of the N-terminal residues from EHD2 prevents ATP hydrolysis; however full-length EHD2 exhibits normal ATPase activity. This may be explained by the relevant role of the N-terminus of EHD2 in guaranteeing the correct architecture of the filaments. It is likely that ATP hydrolysis is unfavored in the flexible and distorted assembly caused by the absence of the N-terminal residues. In a similar way, the deletion of the EH domain, which is also an important regulatory element in assembly, prevents organized oligomerization, tubulation, and hydrolysis (Daumke et al., 2007). It seems that only full-length EHD2 guarantees the correct assembly in which hydrolysis is favored. In comparison to other EHDs, the deletion of the N-terminus in EHD4 did not prevent the stimulated hydrolysis of this construct (Melo et al., 2017). In EHD1, a shorter N-terminal truncation (residues 2-9) resulted in the same stimulated ATPase rates than full-length (Deo et al., 2018). Again, this might be explained by the different activity rates these proteins have. EHD2 is a very slow ATPase, even in the presence of lipids, and the structural alteration of removing the N-terminal stretch results in an even slower ATPase rate. These disparities may explain the specialized and distinct functions and localizations of EHDs. The slow ATPase activity of EHD2 is in accordance with its proposed role in stabilizing caveolae at the plasma membrane. In contrast, the potential roles of EHD1 and EHD4 in endocytic recycling may require faster hydrolysis.

Several studies have hypothesized that ATP hydrolysis would result in the disassembly of EHD oligomers (Deo et al., 2018; Hoernke et al., 2017; Melo et al., 2022). This idea is based on the fact that the switch regions and the KPF loop are destabilized in the ADP-bound state (Melo et al., 2017). This implies that the oligomerization interfaces in which the KPF loop is involved, namely the G interface and the KPF loop – helical domain interface, are weakened when ADP is

bound. The destabilization of the oligomer would lead to disassembly and probably to the conversion to the open conformation in solution (Melo et al., 2022). The investigations reported in this thesis corroborate this concept. It was shown by cryo-ET reconstructions, that EHD2 disengaged from the lipid bilayer when ATP was hydrolyzed, and many lipid tubules lost their shape and curvature. However, when EHD2ΔN was used in these experiments, the oligomeric decoration remains unaltered. This may be explained by the loss of ATPase activity or the greater stability of the densely packed oligomers.

Although more proof supporting an ATPase-driven disassembly has been provided, many questions remain open regarding the nucleotide-loading states of EHD proteins. There is little information about how exactly nucleotide-binding relates to the conformational changes and how hydrolysis is triggered. Many studies with dynamin and dynamin-related proteins were carried out using transition state analogs and non-hydrolysable or slow-hydrolysable analogs of GTP (Daumke & Praefcke, 2016). The use of these nucleotides for structural studies was key for a thorough understanding of the GTPase cycle in these proteins. These investigations are still lacking for EHDs. What is the EHD arrangement in the transition state and in which nucleotide-loading state the opening and the closing of the structure happens, are questions that remain to be answered.

5.4. The cellular function of EHD2 at caveolae

EHD2 was first linked to caveolae in a proteomics study using isolated caveolae from human adipocytes (Aboulaich et al., 2004). Some years later, EHD proteins were found to associate with tubular and vesicular compartments (Blume et al., 2006) and EHD2 was shown to have a peripheral distribution in HeLa cells and the ability to deform membranes EHD2 (Daumke et al., 2007). In later studies, EHD2 was found colocalizing with Cavin1 (Hansen et al., 2011). The specific localization of EHD2 to the neck of caveolae instead of to the bulb was shown using immune-electron microscopy (Ludwig et al., 2013) and, consequently, it was speculated that EHD2 would correspond to the neck structures observed in electron micrographs of caveolae, which had remained unidentified (Richter et al., 2008). Two studies published in the same year shed some light into the function of EHD2 and pointed to a role of EHD2 in the stabilization of caveolae at the plasma membrane, since the depletion of EHD2 increased the mobility of caveolae, but its overexpression confined caveolae to the plasma membrane (Morén et al., 2012; Stoeber et al., 2012). Apart from other functions, caveolae are implicated in cellular lipid and fatty

acid uptake (Briand et al., 2014; Pilch & Liu, 2011), and in the regulation of the endothelial nitric oxide synthase (eNOS) (Förstermann & Sessa, 2012). The physiological consequences of EHD2 loss, which results in more mobile caveolae, have to do with these two mechanisms. EHD2 knock-out mice displayed enlarged lipid droplets in white and brown adipose tissue and in cell types in which caveolae are abundant, such as adipocytes or fibroblasts. Moreover, caveolae were frequently detached from the plasma membrane and displayed elevated mobility (Matthaeus et al., 2020). Additionally, the loss of EHD2 in endothelium resulted in inhibition of eNOS and mice lacking EHD2 showed reduced vessel relaxation due to impaired nitric oxide production (Matthaeus et al., 2019). These studies demonstrate that the absence of EHD2 results in increased caveolar mobility, leading to the current consensus that the function of EHD2 is to keep caveolae confined at the plasma membrane by forming oligomeric ring-like structures around the neck which stabilize membrane curvature. Nonetheless, mechanistic and structural details about how this is achieved were missing.

The EHD2 structures presented in the results from this study provide new insights for a better understanding of this mechanism. First, the diameter range of the lipid tubules that oligomeric EHD2 decorates is similar to the diameter range of the caveolar neck. Second, by means of hydrophobic insertion and scaffolding, EHD2 deforms the lipid bilayer by generating positive and, indirectly, negative curvature. As already discussed above, whereas around the bulb of caveolae there is only positive curvature, negative and positive curvature are present at the neck (Figure 60) (McMahon & Gallop, 2005). These two structural findings support the proposed localization of EHD2 at the neck of caveolae, more specifically at the inflection point between the neck and the bulb, where these two curvatures co-exist.

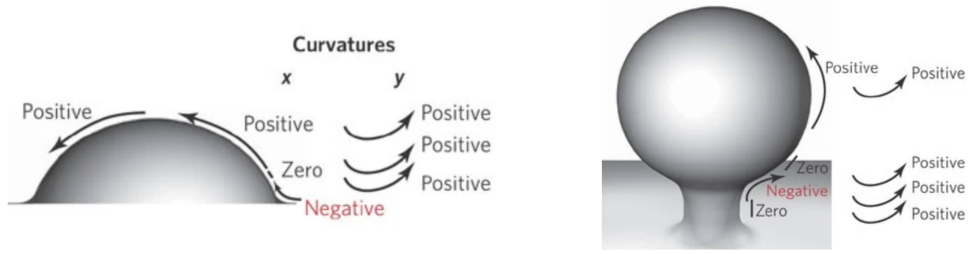

Figure 60. Vesicle budding and the corresponding membrane curvatures. Given that the membrane surface is two-dimensional, curvature must be described in perpendicular directions. The curvature of the initial stage of budding (left panel) is positive in both directions. The curvature of the late stage (right panel) is more complex. There is bidirectional positive curvature around the body of the vesicle, and negative plus positive curvature in perpendicular directions at the interface between the neck and the body. Figure and legend modified from (McMahon & Gallop, 2005).

Moreover, another set of results from this work further validate the precise position of EHD2 at the neck. When the morphology of caveolae was evaluated in wild-type and in EHD2 knock-down endothelial cells, significant alterations were only observed for the necks and not for the bulbs. This means that although the absence of EHD2 affects overall caveolae mobility, the effects of its loss can be locally assessed at the neck. As expected, the depletion of EHD2 resulted in less caveolae confined to the plasma membrane, but those which remained attached exhibited narrower and more elongated necks in comparison to those of wild-type cells. This morphology is consistent with the increased internalization of vesicles, but it also corroborates the idea that EHD2 serves as a membrane-stabilizing scaffold at the neck.

Taken together, these findings reinforce the role of EHD2 in the stabilization of membrane curvature in caveolae, as its absence leads to abnormal curvature at the neck of caveolae. Since EHD2 is also found at flat caveolae (Matthaeus et al., 2022), it is likely that EHD2 participates as well in the generation of curvature, based on the *in vitro* reshaping activity presented here, aiding the cavin-caveolin protein coat in the budding process. When caveolae are curved enough, ATP-bound EHD2 forms stable oligomers around the neck that sustain membrane curvature and secure caveolae at the plasma membrane. Probably, the stabilization is reinforced by interactions with other proteins, such as Pacsin2, which is proposed to bend the membrane in the interface between the plasma membrane and the neck, or with EHBP1, also shown to localize to caveolae. Additionally, it is well known that the contacts between caveolar proteins and the actin cytoskeleton are as well important for the stabilization of the vesicles. The results from this thesis, together with what has been reported in the literature, allow to speculate that internalization of caveolae is only possible when the EHD2 scaffold is disassembled, an event that may happen after ATP hydrolysis. A schematic representation of the proposed model is shown in Figure 61.

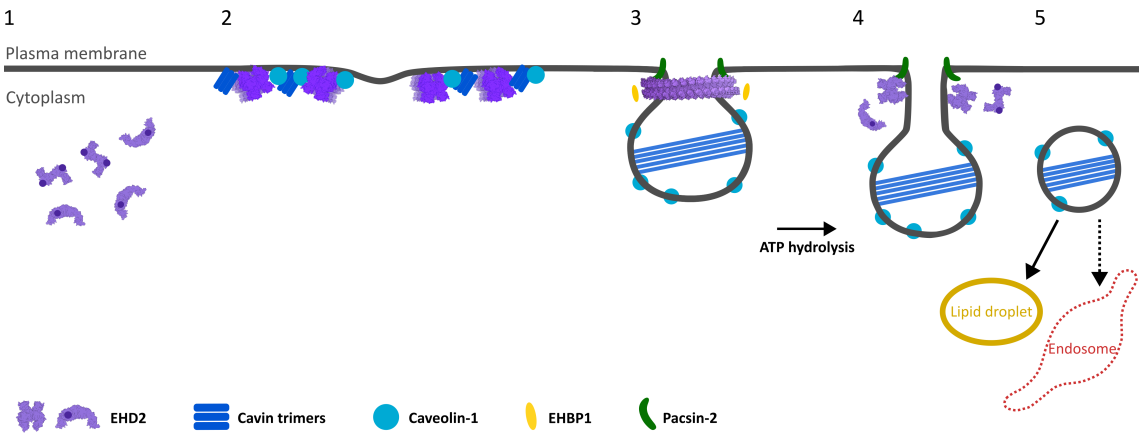

Figure 61. The proposed function of EHD2 at caveolae. 1) EHD2 exists as an open dimer in solution. It is possible that the EH domains adopt a lateral conformation (dark purple dots) which prevents oligomerization. 2) EHD2 is recruited to flat caveolae at the plasma membrane, where caveolins and cavins are also found. On flat membranes, EHD2 is in the closed conformation, which allows oligomerization. Cavins and caveolins are responsible for the initial budding of the membrane. The generation of this curvature might be further assisted by EHD2. 3) In highly curved caveolae, EHD2 forms ring-like oligomeric structures. By generating and stabilizing both positive and negative curvature, EHD2 oligomers accommodate at the neck of caveolae. The curvature of the neck is further stabilized by the F-BAR domain protein Pacsin2. EHBP1, a binding partner of EHD2, has also been localized to highly curved caveolae. 4) After ATP hydrolysis is triggered, EHD2 may disassemble and detach from the membrane. It is possible that in the ADP-bound form EHD2 converts back to the open conformation. When the neck of caveolae loses the EHD2 scaffold, the curvature of the membrane becomes unstable, leading to complete internalization. 5) Caveolae participate in vesicular trafficking of fatty acids to lipid droplets. Although without specific cargo, they may also reach the endosomes.

There are several open questions that need to be addressed in the future. One first aspect to consider is the recruitment of EHD2 to the plasma membrane, how it finds the flat caveolar surfaces and whether it arrives there in the open or in the closed conformation. Second, more research is necessary to understand how ATP hydrolysis is triggered: is it self-regulated based on the intrinsic slow ATPase activity of EHD2, or is it prompted or accelerated by extrinsic factors such as membrane curvature and morphology or interaction with other proteins? Lastly, the information about how EHD2 forms complexes with the predicted interaction partners is scarce. Structural investigations are needed for a deeper understanding. The reconstitution of these proteins together with EHD2 in liposomes for *in vitro* cryo-electron microscopy or tomography may help in deciphering binding contacts and ratios. Ideally, investigations using the state-of-the-art *in situ* cryo-electron tomography could provide exceptional insights to better comprehend the structure of EHD2 in the cellular context and gain a more holistic view of its role in the regulation of caveolae dynamics.

Appendix A – List of instruments

Instrument	Manufacturer
Agarose Gel Electrophoresis System	OLS, Bremen, D
Äkta Purifier	GE Healthcare, Piscataway, USA
Amersham Protran western blotting membranes, nitrocellulose	Sigma-Aldrich, Steinheim, D
Amicon centrifugal filter devices	Millipore, Billerica, USA
Benchtop Centrifuge 5415 D	Eppendorf, Hamburg, D
Benchtop Centrifuge 5415 R	Eppendorf, Hamburg, D
Benchtop Centrifuge 5804 R	Eppendorf, Hamburg, D
Cell culture incubator CB 170	Binder GmbH, Tuttlingen, D
Cell culture plates, dishes and flasks	Sarstedt AG, Nümbrecht, D
Centrifuge Avanti J-26 XP	Beckman Coulter, Krefeld, D
Chromatography column material GSH Sepharose 4B	GE Healthcare, Piscataway, USA
Chromatography column material Ni Sepharose HP	GE Healthcare, Piscataway, USA
Chromatography columns Superdex 200 10/300, GL	GE Healthcare, Piscataway, USA
Chromatography columns Superdex 200 16/60, 26/60	GE Healthcare, Piscataway, USA
Colloidal gold beads (5 and 10 nm)	Sigma-Aldrich, Steinheim, D
Cryo-Electron tomography grids	Quantifoil Micro Tools GmbH, Jena, D
Electron microscopy grids	Plano GmbH, Wetzlar, D
Extruder	Sigma-Aldrich, Steinheim, D
Fluidizer M-110L	Pneumatic Microfluidics, Newton, USA
Glass coverslips	Gerhard Menzel GmbH, Braunschweig, D
High Pressure Freezer - Leica EM ICE	Leica Camera AG, Wetzlar, D
HPLC Infinity 1260	Agilent Technologies, Santa Clara, USA
Hypersil ODS guard column	Agilent Technologies, Santa Clara, USA
Laminar flow safety cabinet Herasafe	Thermo Scientific, Dreieich, D
LUNA-FL dual fluorescence cell counter	Logos Biosystems, Anyang, KR
Microscopy glass slides	Gerhard Menzel GmbH, Braunschweig, D
Microtome and diamond knives	Leica Camera AG, Wetzlar, D
Nikon Eclipse Ts2 Microscope	Nikon Corporation, JP
Peristaltic Pump Reglo Analog ISM827B	Ismatec, Glattbrugg, CH
pH-Meter	Mettler-Toledo, Gießen, D
Photometer BioPhotometer	Eppendorf, Hamburg, D
Photometer NanoDrop 2000	Thermo Scientific, Dreieich, D
Reversed-phase ODS-2 Hypersil HPLC column	Thermo Scientific, Dreieich, D
SDS PAGE System Xcell Sure Lock	SDS PAGE System Xcell Sure Lock
Shaker Incubator Innova44	New Brunswick Scientific, Edison, USA
Thermocycler TGradient	Thermocycler TGradient
Thermocycler TPersonal	Thermocycler TGradient
Thermomixer Comfort	Eppendorf, Hamburg, D
Transmission Electron Microscope Talos L120C	Thermo Fisher Scientific, Waltham, USA
Transmission Electron Microscope Titan Krios G3i	Thermo Fisher Scientific, Waltham, USA
Ultracentrifuge Optima L-100K	Beckman Coulter, Krefeld, D
Ultracentrifuge Optima TLX	Beckman Coulter, Krefeld, D
Vitrobot Mark IV	Thermo Fisher Scientific, Waltham, USA
Western Blot Module Xcell II	SDS PAGE System Xcell Sure Lock
Zeiss LSM700 scanning confocal microscope	Carl Zeiss AG, Jena, D

Appendix B – List of chemicals

Chemicals	Cat. No.	Manufacturer
Acetonitrile	CN20.2	Roth, Karlsruhe, D
ADP	NU-1198	Jena Bioscience, Jena, D
AEBSF Protease Inhibitor	78431	Thermo Scientific, Dreieich, D
Agarose	2267.3	Roth, Karlsruhe, D
ATP	NU-1049	Jena Bioscience, Jena, D
Beta-mercaptoethanol	4227.1	Roth, Karlsruhe, D
Calcium chloride	A119.1	Roth, Karlsruhe, D
Chloramphenicol	3886.3	Roth, Karlsruhe, D
Chloroform	C2432-1L	Sigma-Aldrich, Steinheim, D
Coomassie brilliant blue R 250	3862.2	Roth, Karlsruhe, D
di-Potassium hydrogen phosphate anhydrous	P749.2	Roth, Karlsruhe, D
DTT	6908.2	Roth, Karlsruhe, D
EDTA	8040.2	Roth, Karlsruhe, D
Ethanol	5054.2	Roth, Karlsruhe, D
Fetal bovine serum	A11-211	PAA laboratories, Pasching, A
Fibronectin bovine plasma solution	33010018	Thermo Scientific, Dreieich, D
Folch brain lipid extract from bovine brain	B1502-1G	Sigma-Aldrich, Steinheim, D
Gibco DPBS	14190144	Thermo Scientific, Dreieich, D
Glutaraldehyde	4157.2	Roth, Karlsruhe, D
Glycerol	3783.1	Roth, Karlsruhe, D
HEPES	9105.4	Roth, Karlsruhe, D
Imidazole	3899.3	Roth, Karlsruhe, D
Isopropanol	9866.5	Roth, Karlsruhe, D
Kanamycinsulfate	T823.4	Roth, Karlsruhe, D
Magnesium chloride Hexahydrate	63065	Sigma-Aldrich, Steinheim, D
Mark12TM unstained standard	LC5677	Life Techologies, Karlsruhe, D
Methanol	4627.5	Roth, Karlsruhe, D
Ni Sepharose HP	71-5027-67	GE Healthcare, München, D
NuPAGE© LDS Sample Buffer (4x)	NP0007	Life Techologies, Karlsruhe, D
NuPAGE© MES SDS Buffer Kit	NP0060	Life Techologies, Karlsruhe, D
Osmium tetroxide	8371.1	Roth, Karlsruhe, D
Paraformaldehyde	0335.2	Roth, Karlsruhe, D
Penicillin-Streptomycin	15140-122	Life Techologies, Karlsruhe, D
Potassium chloride	6781.3	Roth, Karlsruhe, D
Potassium dihydrogen phosphate	3904.1	Roth, Karlsruhe, D
Potassium phosphate dibasic	450200	Sigma-Aldrich, Steinheim, D
Sodium chloride	9265.2	Roth, Karlsruhe, D
Sodium phosphate dibasic	71640-M	Sigma-Aldrich, Steinheim, D
Tetrabutylammonium bromide	86860	Sigma-Aldrich, Steinheim, D
TRIS	A411.3	Roth, Karlsruhe, D
Trypsin-EDTA (0.25%)	25200056	Thermo Scientific, Dreieich, D
Uranyl acetate dihydrate	73943	Sigma-Aldrich, Steinheim, D

Appendix C – List of buffers

Buffer	Components
ATPase buffer	25 mM HEPES pH 7.5 300 mM NaCl 1 mM DTT 0.5 mM MgCl2
Cryo-EM buffer	20 mM HEPES pH 7.5 300 mM NaCl 0.5 mM $MgCl_2$
HPLC buffer	100 mM potassium phosphate buffer pH 6.5 10 mM tetrabutylammonium bromide 7.5% acetonitrile
Liposome buffer	25 mM HEPES pH 7.5 300 mM NaCl 1 mM DTT
PBS (10X)	1.37 M NaCl 27 mM KCl 100 mM Na_2HPO_4 18 mM KH_2PO4
Protein purification buffers	
Resuspension buffer	50 mM HEPES pH 7.5 400 mM NaCl 25 mM imidazole 2.5 mM β-mercaptoethanol 250 µM Pefabloc 1 µg/ml DNase I
Equilibration buffer	50 mM HEPES pH 7.5 400 mM NaCl 25 mM imidazole 2.5 mM β-mercaptoethanol
Washing buffer 1	20 mM HEPES pH 7.5 700 mM NaCl 30 mM imidazole 2.5 mM β-mercaptoethanol 1 mM ATP 10 mM KCl
Washing buffer 2	20 mM HEPES pH 7.5 300 mM NaCl 25 mM imidazole 2.5 mM β-mercaptoethanol
Elution buffer 1	20 mM HEPES pH 7.5 300 mM NaCl 300 mM imidazole 2.5 mM β-mercaptoethanol
Dialysis buffer	20 mM HEPES pH 7.5 300 mM NaCl 2.5 mM β-mercaptoethanol

Washing buffer 3	20 mM HEPES pH 7.5 300 mM NaCl 2.5 mM β-mercaptoethanol
Elution buffer 2	20 mM HEPES pH 7.5 300 mM NaCl 25 mM imidazole 2.5 mM β-mercaptoethanol
Elution buffer 2	20 mM HEPES pH 7.5 300 mM NaCl 50 mM imidazole 2.5 mM β-mercaptoethanol
SEC buffer	20 mM HEPES pH 7.5 300 mM NaCl 2.5 mM β-mercaptoethanol 2.5 mM $MgCl_2$

Appendix D – List of software

Software	Developer or Reference
Amira 2020	Thermo Fisher Scientific, Waltham, USA
Ccp4 v.7.1	Winn M. D., 2011 (Winn et al., 2011)
Chimera v.1.16	UCSF Resource for Biocomputing, Visualization, and Informatics
ChimeraX v.1.5	UCSF Resource for Biocomputing, Visualization, and Informatics
Coot v.0.8	Emsley P., 2010 (Emsley et al., 2010)
Dynamo	Castaño-Díez D., 2012 (Castaño-Díez et al., 2012)
Phenix v.1.20	Liebschner D., 2019 (Liebschner et al., 2019)
GraphPad Prism v.7.05	GraphPad Software, San Diego, USA
ImageJ v.1.52a	Schneider, C.A. et al., 2012 (Schneider et al., 2012)
IMOD v.4.11	Kremer J.R., Mastronarde D.N. and McIntosh J.R., 1996 (Kremer et al., 1996)
Microscopy Imagae Browser	Belevich I., 2016 (Belevich et al., 2016)
SerialEM	Mastronarde D.N., 2003 (Mastronarde, 2005)
SMOG v2.3	Noel J. K., 2016 (Noel et al., 2016)
SUSAN	https://github.com/rkms86/SUSAN
TomoBEAR	https://github.com/KudryashevLab/TomoBEAR
ZEN	Carl Zeiss AG, Jena, D

Appendix E – Sequence alignment

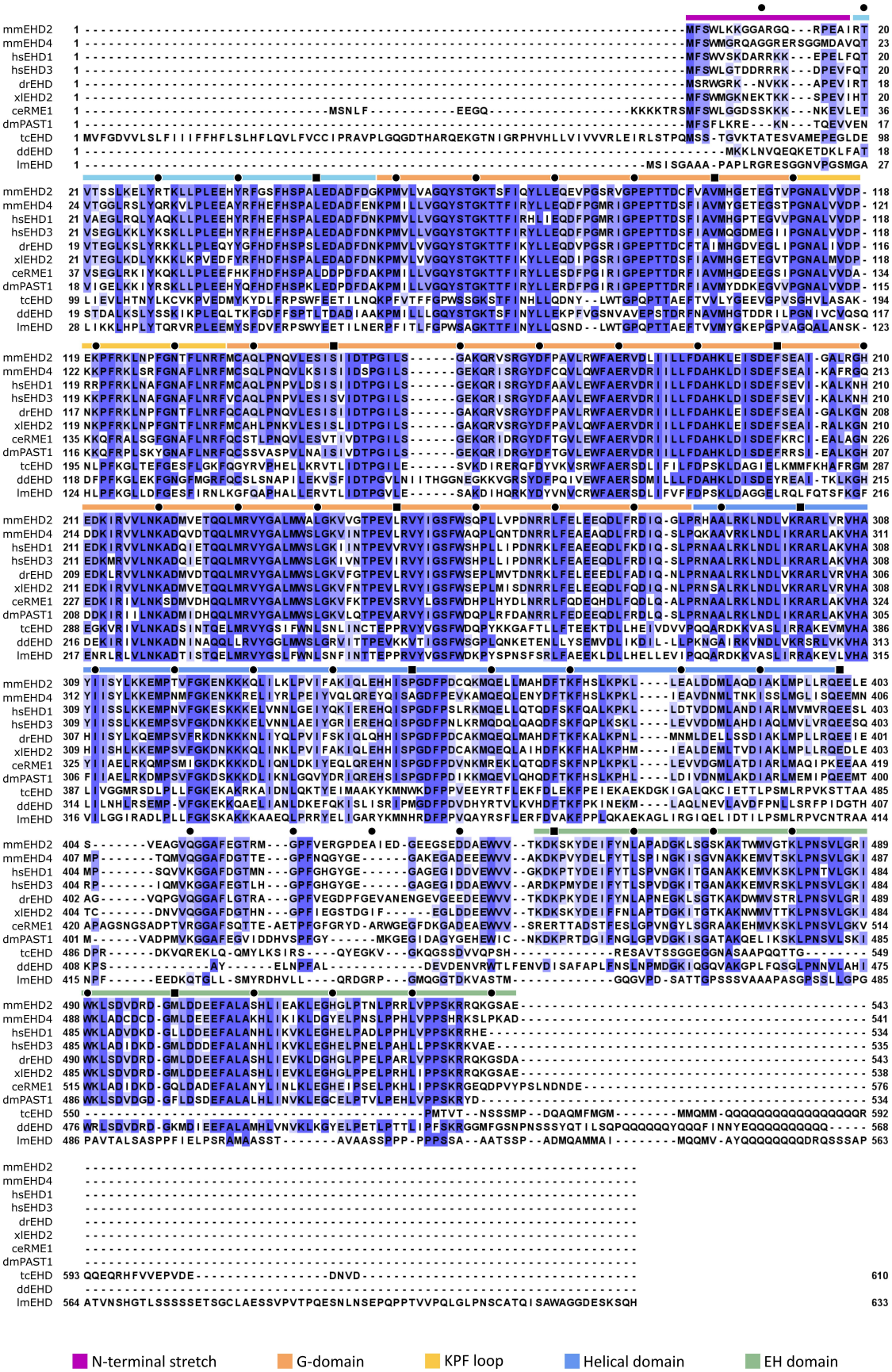

***See next page for details**

Multiple sequence alignment of EHD proteins. Using *Mus musculus* (mm) EHD2 (Q8BH64) as a reference, the following sequences were aligned using Clustal W: *Mus musculus* (mm) EHD4 (Q9EQP29, *Homo sapiens* (hs) EHD1 (Q9H4M9) and EHD3 (Q9NZN3), *Danio rerio* (dr) EHD (Q6P3J7), *Xenopus laevis* (xl) EHD1 (Q32NW7), *Caenorhabditis elegans* (ce) RME-1 (G5ECC3), *Drosophila melanogaster* (dm) PAST-1 (Q8IGN0), *Trypanosoma cruzi* (tc) EHD (Q4DYK9), *Dictyostelium discoideum* (dd) EHD (Q54ST5), *Leishmania major* (lm) EHD (Q4QDJ3). Residues with more than 60% identity are shaded in blue (the darker the shade, the more conserved). Domains are indicated on top of the sequence. Black dots are positioned every 10 residues, and black squares every 50.

Appendix F – Subtomogram Averaging Workflows

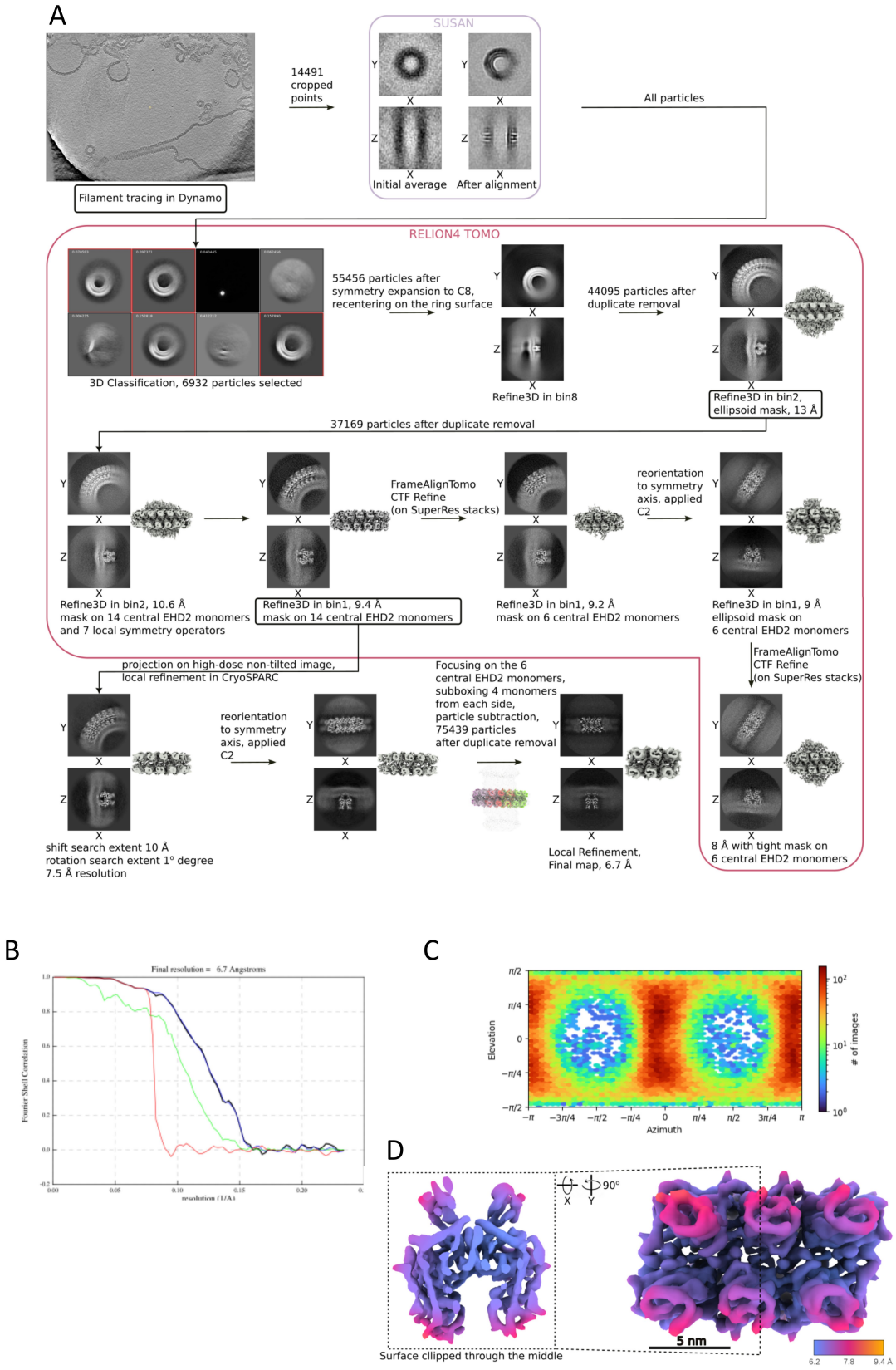

Structure determination of full-length EHD2. A) Schematic representation of the subtomogram averaging workflow and obtained results. B) Gold standard Fourier Shell Correlation. C) Angular distribution of particles. D) Final map colored by local resolution. Figure by Vasilii Mikirtumov.

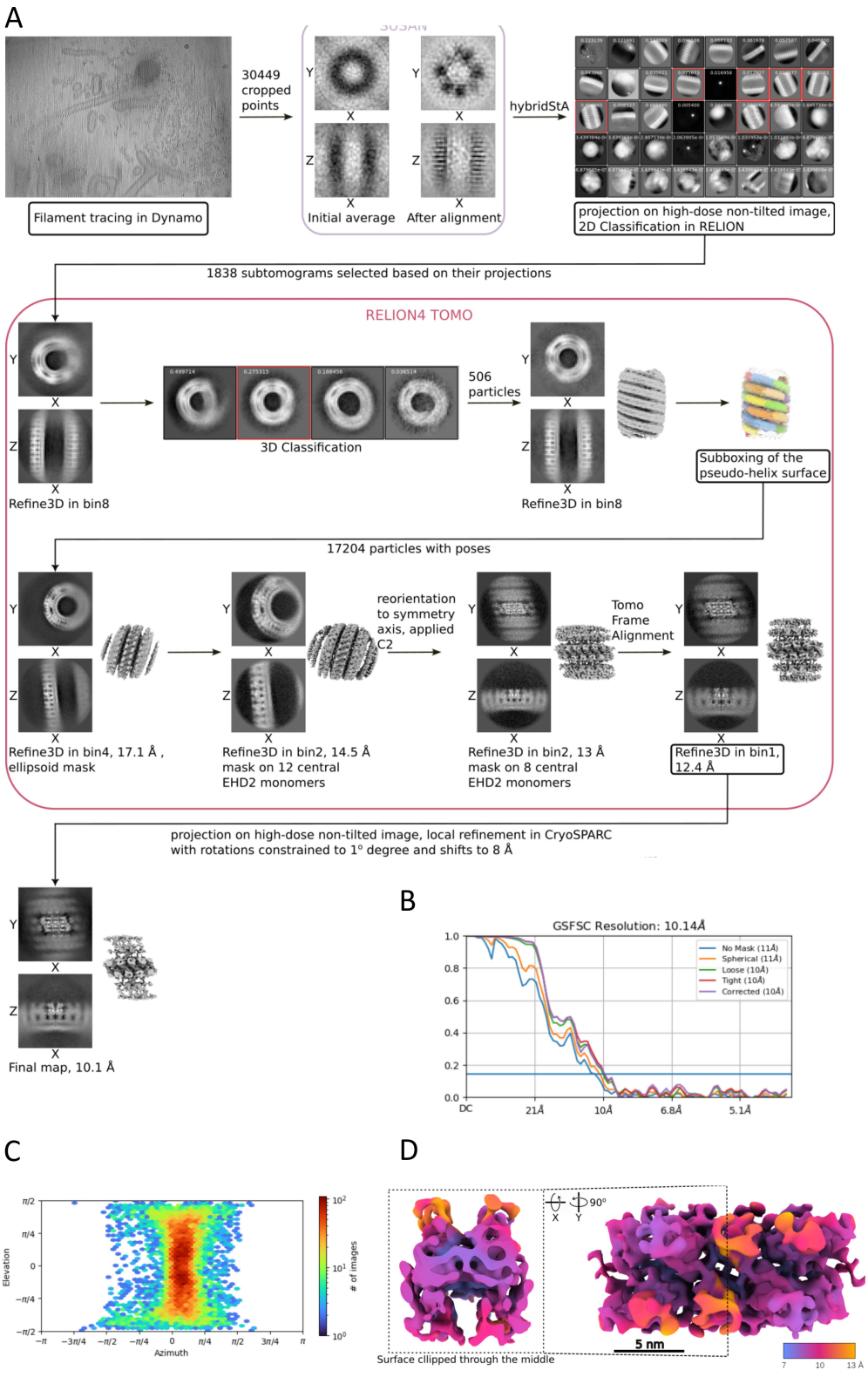

Structure determination of N-terminally truncated EHD2. A) Schematic representation of the subtomogram averaging workflow and obtained results. B) Gold standard Fourier Shell Correlation. C) Angular distribution of particles. D) Final map colored by local resolution. Figure by Vasilii Mikirtumov.

Appendix G – Data collection, refinement, and validation

	EHD2	EHD2ΔN
Data collection and processing		
Magnification	42,000	42,000
Voltage (kV)	300	300
Electron exposure ($e^-/Å^2$)	100	158
Defocus range (μm)	-2 – -7	-1.5 – -5
Pixel size (Å)	1.069	1.069
Symmetry imposed	C2	C2
Initial particle images (no.)	14,491	30,449
Final particle images (no.)	6,932	17,204
Map resolution (Å)	6.7	11
FSC threshold	0.143	0.143
Map resolution range (Å)	6.2 – 9.4	6.3 – 16.6
Refinement		
Initial model used (PDB code)	4CID	4CID
Map sharpening *B* factor ($Å^2$)	-200	-200
Model composition		
Non-hydrogen atoms	16576	16576
Protein residues	2084	2084
Ligands	0	0
R.m.s. deviations		
Bond lengths (Å)	0.004	0.002
Bond angles (°)	0.856	0.638
Validation		
MolProbity score	2.16	1.89
Clashcore	21.26	12.01
Poor rotamers (%)	0.00	0.00
Ramachandran plot		
Favored (%)	95.18	95.76
Allowed (%)	4.82	4.05
Disallowed (%)	0.00	0.19

Abbreviations

ADP	Adenosine diphosphate
AEBSF	4-(2-aminoethyl)benzenesulfonyl fluoride ATP
ATP	Adenosine triphosphate
Cryo-EM	Cryo-electron microscopy
Cryo-EM/T	Cryo-electron microscopy/tomography
Cryo-ET	Cryo-electron tomography
C-terminus	Carboxy-terminus
DAPI	4′,6-diamidino-2-phenylindole
DMEM	Dulbecco's Modified Eagle Medium
DMSO	Dimethyl sulfoxide
DNA	Deoxyribonucleic acid
DPBS	Dulbecco's phosphate buffer saline
DTT	Dithiothreitol
E. coli	*Escherichia coli*
EDTA	Ethylenediaminetetraacetic acid
EHD	Eps15 homology domain containing protein
EM	Electron microscopy
FL	Full-length
GA	Glutaraldehyde
GDP	Guanosine diphosphate
GTP	Guanosine triphosphate
HEPES	4-(2-hydroxyethyl)-1-piperazineethanesulfonic acid
HPLC	High-performance liquid chromatography
HRP	Horseradish peroxidase
HUVEC	Human umbilical vein endothelial cells
IPTG	Isopropyl β-D-1-thiogalactopyranoside
KD	Knock-down
KO	Knock-out
MCS	Multicloning site
MDC	Max-Delbrück Center for Molecular Medicine, Berlin
MEF	Mouse embryionic fibroblasts
MWCO	Molecular weight cut-off
Ni-NTA	Nickel-nitrilotriacetic acid (nickel-charged resin)
N-terminus	Amino-terminus
PBS	Phosphate buffer saline
PCR	Polymerase chain reaction
PFA	Paraformaldehyde
PtdIns	Phosphatidyl inositol
SDS-PAGE	Sodium dodecyl sulfate polyacrylamide gel electrophoresis
SEC	Size exclusion chromatography
SIRT	Simultaneous Iterative Reconstruction Technique
SPA	Single particle analysis
STA	Subtomogram averaging
TB	Terrific broth
TBS	Tris-buffered saline
TBS-T	Tris-buffered saline with Tween20

v/v	Volume per volume
WT	Wild-type
ΔEH	EH domain truncation
ΔN	N-terminally truncated

References

Aboulaich, N., Vainonen, J. P., Strålfors, P., & Vener, A. V. (2004). Vectorial proteomics reveal targeting, phosphorylation and specific fragmentation of polymerase I and transcript release factor (PTRF) at the surface of caveolae in human adipocytes. *Biochemical Journal*, *383*(2), 237–248. https://doi.org/10.1042/BJ20040647

Antonny, B., Beraud-Dufour, S., Chardin, P., & Chabre, M. (1997). N-terminal hydrophobic residues of the G-protein ADP-ribosylation factor-1 insert into membrane phospholipids upon GDP to GTP exchange. *Biochemistry*, *36*(15), 4675–4684. https://doi.org/10.1021/bi962252b

Antonny, B., Burd, C., Camilli, P. De, Chen, E., Daumke, O., Ford, M., Frolov, V. A., Frost, A., Hinshaw, J. E., Kirchhausen, T., Kozlov, M. M., Lenz, M., Low, H. H., Mcmahon, H. T., & Merrifield, C. (2016). Membrane fission by dynamin : what we know and what we need to know. *The EMBO Journal*, *35*(21), 2270–2284. https://doi.org/10.15252/embj.201694613

Bahl, K., Xie, S., Spagnol, G., Sorgen, P. L., Naslavsky, N., & Caplan, S. (2016). EHD3 protein is required for tubular recycling endosome stabilization, and an asparagine-glutamic acid residue pair within its Eps15 Homology (EH) domain dictates its selective binding to NPF peptides. *Journal of Biological Chemistry*, *291*(26), 13465–13478. https://doi.org/10.1074/jbc.M116.716407

Belevich, I., Joensuu, M., Kumar, D., Vihinen, H., & Jokitalo, E. (2016). Microscopy Image Browser: A Platform for Segmentation and Analysis of Multidimensional Datasets. *PLoS Biology*, *14*(1), 1–13. https://doi.org/10.1371/journal.pbio.1002340

Bhatia, V. K., Hatzakis, N. S., & Stamou, D. (2010). A unifying mechanism accounts for sensing of membrane curvature by BAR domains, amphipathic helices and membrane-anchored proteins. *Seminars in Cell and Developmental Biology*, *21*(4), 381–390. https://doi.org/10.1016/j.semcdb.2009.12.004

Bhattacharyya, S., & Pucadyil, T. J. (2020). Cellular functions and intrinsic attributes of the ATP-binding Eps15 homology domain-containing proteins. *Protein Science*, *29*(6), 1321–1330. https://doi.org/10.1002/pro.3860

Bhattacharyya, S., Rainey, M. A., Arya, P., Dutta, S., George, M., Storck, M. D., McComb, R. D., Muirhead, D., Todd, G. L., Gould, K., Datta, K., Waes, J. G. Van, Band, V., & Band, H. (2016). Endocytic recycling protein EHD1 regulates primary cilia morphogenesis and SHH signaling during neural tube development. *Scientific Reports*, *6*(February). https://doi.org/10.1038/srep20727

Blume, J. J., Halbach, A., Behrendt, D., Paulsson, M., & Plomann, M. (2006). *EHD proteins are associated with tubular and vesicular compartments and interact with specific phospholipids*. *13*. https://doi.org/10.1016/j.yexcr.2006.10.006

Bonifacino, J. S., & Glick, B. S. (2004). The Mechanisms of Vesicle Budding and Fusion. *Cell*, *116*, 153–166. https://doi.org/10.1016/s0092-8674(03)01079-1

Briand, N., Prado, C., Mabilleau, G., Lasnier, F., Le Lièpvre, X., Covington, J. D., Ravussin, E., Le Lay, S., & Dugail, I. (2014). Caveolin-1 expression and cavin stability regulate caveolae dynamics in adipocyte lipid store fluctuation. *Diabetes*, *63*(12), 4032–4044. https://doi.org/10.2337/db13-1961

Byrnes, L. J., Singh, A., Szeto, K., Benvin, N. M., Donnell, J. P. O., Zipfel, W. R., & Sondermann, H. (2013). Structural basis for conformational switching and GTP loading of the large G protein atlastin. *The EMBO Journal*, *32*(3), 369–384. https://doi.org/10.1038/emboj.2012.353

Byrnes, L. J., & Sondermann, H. (2011). Structural basis for the nucleotide-dependent dimerization of the large G protein atlastin-1 / SPG3A. *PNAS*, *108*(6), 1–6. https://doi.org/10.1073/pnas.1012792108

Cai, B., Caplan, S., & Naslavsky, N. (2012). cPLA2α and EHD1 interact and regulate the vesiculation of cholesterol-rich, GPI-anchored, protein-containing endosomes. *Molecular Biology of the Cell*, *23*(10), 1874–1888. https://doi.org/10.1091/mbc.E11-10-0881

Cai, B., Giridharan, S. S. P., Zhang, J., Saxena, S., Bahl, K., Schmidt, J. A., Sorgen, P. L., Guo, W., Naslavsky, N., & Caplan, S. (2013). Differential roles of C-terminal eps15 homology domain proteins as vesiculators and tubulators of recycling endosomes. *Journal of Biological Chemistry*, *288*(42), 30172–30180. https://doi.org/10.1074/jbc.M113.488627

Campelo, F., Fabrikant, G., McMahon, H. T., & Kozlov, M. M. (2010). Modeling membrane shaping by proteins: Focus on EHD2 and N-BAR domains. *FEBS Letters*, *584*(9), 1830–1839. https://doi.org/10.1016/j.febslet.2009.10.023

Cao, Y., Meng, S., Chen, Y., Feng, J., Gu, D., Yu, B., Li, J., Yang, J., Liao, S., Chan, D. C., & Gao, S. (2017). Mfn1 structures reveal nucleotide-triggered dimerization critical for mitochondrial fusion. *Nature*, *542*(7641), 372–376. https://doi.org/10.1038/nature21077.Mfn1

Castaño-Díez, D., Kudryashev, M., Arheit, M., & Stahlberg, H. (2012). Dynamo: A flexible, user-friendly development tool for subtomogram averaging of cryo-EM data in high-performance computing environments. *Journal of Structural Biology*, *178*(2), 139–151.

https://doi.org/https://doi.org/10.1016/j.jsb.2011.12.017

Chappie, J. S., Acharya, S., Leonard, M., Schmid, S. L., & Dyda, F. (2010). G domain dimerization controls dynamin's assembly-stimulated GTPase activity. *Nature*, *465*(7297), 435–440. https://doi.org/10.1038/nature09032.G

Chappie, J. S., Mears, J. A., Fang, S., Leonard, M., Schmid, S. L., Milligan, R. A., Hinshaw, J. E., & Dyda, F. (2011). A pseudo-atomic model of the dynamin polymer identifies a hydrolysis-dependent powerstroke. *Cell*, *147*(1), 209–222. https://doi.org/10.1016/j.cell.2011.09.003.A

Chaudhary, N., Gomez, G. A., Howes, M. T., Lo, H. P., McMahon, K. A., Rae, J. A., Schieber, N. L., Hill, M. M., Gaus, K., Yap, A. S., & Parton, R. G. (2014). Endocytic Crosstalk: Cavins, Caveolins, and Caveolae Regulate Clathrin-Independent Endocytosis. *PLoS Biology*, *12*(4). https://doi.org/10.1371/journal.pbio.1001832

Cheng, X., & Smith, J. C. (2019). Biological Membrane Organization and Cellular Signaling. *Chemical Reviews*, *119*(9), 5849–5880. https://doi.org/10.1021/acs.chemrev.8b00439

Daumke, O., Lundmark, R., Vallis, Y., Martens, S., Butler, P. J. G., & McMahon, H. T. (2007). Architectural and mechanistic insights into an EHD ATPase involved in membrane remodelling. *Nature*, *449*(October), 923–927. https://doi.org/10.1038/nature06173

Daumke, O., & Praefcke, G. J. K. (2016). Mechanisms of GTP Hydrolysis and Conformational Transitions in the Dynamin Superfamily. *Biopolymers*, *105*(8), 580–593. https://doi.org/10.1002/bip.22855

Delivery, I., Gl, T., Hypothesis, L., & Johannes, L. (2021). The Cellular and Chemical Biology of Endocytic Trafficking and Intracellular Delivery—The GL–Lect Hypothesis. *Molecules*. https://doi.org/https://doi.org/10.3390/molecules26113299

Demonbreun, A. R., Swanson, K. E., Rossi, A. E., Deveaux, H. K., Earley, J. U., Allen, M. V., Arya, P., Bhattacharyya, S., Band, H., Pytel, P., & McNally, E. M. (2015). Eps 15 homology domain (EHD)-1 remodels transverse tubules in skeletal muscle. *PLoS ONE*, *10*(9), 1–17. https://doi.org/10.1371/journal.pone.0136679

Deo, R., Kushwah, M. S., Kamerkar, S. C., Kadam, N. Y., Dar, S., Babu, K., Srivastava, A., & Pucadyil, T. J. (2018). ATP-dependent membrane remodeling links EHD1 functions to endocytic recycling. *Nature Communications*, *9*(1). https://doi.org/10.1038/s41467-018-07586-z

Dodonova, S. O., Diestelkoetter-Bachert, P., von Appen, A., Hagen, W. J. H., Beck, R., Beck, M., Wieland, F., & Briggs, J. A. G. (2015). A structure of the COPI coat and the role of coat

proteins in membrane vesicle assembly. *Science*, *349*(6244), 195–198. https://doi.org/10.1126/science.aab1121

Doherty, G. J., & Mcmahon, H. T. (2009). Mechanisms of endocytosis. *Annual Review of Biochemistry*, *78*, 857–902. https://doi.org/10.1146/annurev.biochem.78.081307.110540

Doherty, K. R., Cave, A., Davis, D. B., Delmonte, A. J., Posey, A. D., Earley, J. U., Hadhazy, M., & McNally, E. M. (2005). Normal myoblast fusion requires myoferlin. *Development*, *132*(24), 5565–5575. https://doi.org/10.1242/dev.02155

Doherty, K. R., Demonbreun, A. R., Wallace, G. Q., Cave, A., Posey, A. D., Heretis, K., Pytel, P., & McNally, E. M. (2008). The endocytic recycling protein EHD2 interacts with myoferlin to regulate myoblast fusion. *Journal of Biological Chemistry*, *283*(29), 20252–20260. https://doi.org/10.1074/jbc.M802306200

Echarri, A., & Del Pozo, M. A. (2006). Caveolae internalization regulates integrin-dependent signaling pathways. *Cell Cycle*, *5*(19), 2179–2182. https://doi.org/10.4161/cc.5.19.3264

Echarri, A., & Del Pozo, M. A. (2015). Caveolae - mechanosensitive membrane invaginations linked to actin filaments. *Journal of Cell Science*, *128*(15), 2747–2758. https://doi.org/10.1242/jcs.153940

Emsley, P., Lohkamp, B., Scott, W. G., & Cowtan, K. (2010). Features and development of Coot. *Acta Crystallographica Section D: Biological Crystallography*, *66*(4), 486–501. https://doi.org/10.1107/S0907444910007493

Faelber, K., Dietrich, L., Noel, J. K., Wollweber, F., Pfitzner, A. K., Mühleip, A., Sánchez, R., Kudryashev, M., Chiaruttini, N., Lilie, H., Schlegel, J., Rosenbaum, E., Hessenberger, M., Matthaeus, C., Kunz, S., von der Malsburg, A., Noé, F., … Daumke, O. (2019). Structure and assembly of the mitochondrial membrane remodelling GTPase Mgm1. *Nature*, *571*(7765), 429–433. https://doi.org/10.1038/s41586-019-1372-3

Faelber, K., Gao, S., Held, M., Posor, Y., Haucke, V., Noé, F., & Daumke, O. (2013). Oligomerization of Dynamin Superfamily Proteins in Health. In *Prog Mol Biol Transl Sci* (1st ed., Vol. 117). Progress in Molecular Biology and Translational Science. https://doi.org/10.1016/B978-0-12-386931-9.00015-5

Faelber, K., Posor, Y., Gao, S., Held, M., Roske, Y., Schulze, D., Haucke, V., Noé, F., & Daumke, O. (2011). Crystal structure of nucleotide-free dynamin. *Nature*, *477*, 556–562. https://doi.org/10.1038/nature10369

Fernandez, I., Ying, Y., Albanesi, J., & Anderson, R. G. W. (2002). Mechanism of caveolin filament assembly. *Proceedings of the National Academy of Sciences of the United States of*

America, *99*(17), 11193–11198. https://doi.org/10.1073/pnas.172196599

Förstermann, U., & Sessa, W. C. (2012). Nitric oxide synthases: Regulation and function. *European Heart Journal*, *33*(7), 829–837. https://doi.org/10.1093/eurheartj/ehr304

Fröhlich, C., Grabiger, S., Schwefel, D., Faelber, K., Rosenbaum, E., Mears, J. A., Rocks, O., & Daumke, O. (2013). Structural insights into oligomerization and mitochondrial remodelling of dynamin 1-like. *The EMBO Journal*, *32*(9), 1280–1292. https://doi.org/10.1038/emboj.2013.74

Gallop, J. L., Jao, C. C., Kent, H. M., Butler, P. J. G., Evans, P. R., Langen, R., & Mcmahon, H. T. (2006). *Mechanism of endophilin N-BAR domain- mediated membrane curvature*. *25*(12), 2898–2910. https://doi.org/10.1038/sj.emboj.7601174

Ganichkin, O. M., Vancraenenbroeck, R., Rosenblum, G., Hofmann, H., Mikhailov, A. S., Daumke, O., & Noel, J. K. (2021). Quantification and demonstration of the collective constriction-by-ratchet mechanism in the dynamin molecular motor. *Proceedings of the National Academy of Sciences of the United States of America*, *118*(28), 1–11. https://doi.org/10.1073/PNAS.2101144118

Giridharan, S. S. P., Cai, B., Vitale, N., Naslavsky, N., & Caplan, S. (2013). Cooperation of MICAL-L1, syndapin2, and phosphatidic acid in tubular recycling endosome biogenesis. *Molecular Biology of the Cell*, *24*, 1776–1790. https://doi.org/10.1091/mbc.E13-01-0026

Grant, B. D., & Caplan, S. (2008). Mechanisms of EHD/RME-1 Protein Function in Endocytic Transport Barth. *Traffic*, *9*(12), 2043–2052. https://doi.org/10.1111/j.1600-0854.2008.00834.x.Mechanisms

Grant, B. D., Zhang, Y., Paupard, M. C., Lin, S. X., Hall, D. H., & Hirsh, D. (2001). Evidence that RME-1, a conserved C. elegans EH-domain protein, functions in endocytic recycling. *Nature Cell Biology*, *3*(6), 573–579. https://doi.org/10.1038/35078549

Gudmundsson, H., Curran, J., Kashef, F., Snyder, J. S., Smith, S. A., Vargas-Pinto, P., Bonilla, I. M., Weiss, R. M., Anderson, M. E., Binkley, P., Felder, R. B., Carnes, C. A., Band, H., Hund, T. J., & Mohler, P. J. (2012). Differential regulation of EHD3 in human and mammalian heart failure. *Journal of Molecular and Cellular Cardiology*, *52*(5), 1183–1190. https://doi.org/10.1016/j.yjmcc.2012.02.008

Guilherme, A., Soriano, N. A., Furcinitti, P. S., & Czech, M. P. (2004). Role of EHD1 and EHBP1 in Perinuclear Sorting and. *The Journal of Biological Chemistry*, *279*(38), 40062–40075. https://doi.org/10.1074/jbc.M401918200

Haller, O., Gao, S., Malsburg, A., Daumke, O., & Kochs, G. (2010). Dynamin-like MxA GTPase :

Structural Insights into Oligomerization and Implications for Antiviral Activity. *The Journal of Biological Chemistry*, *285*(37), 28419–28424. https://doi.org/10.1074/jbc.R110.145839

Han, B., Porta, J. C., Hanks, J. L., Peskova, Y., Binshtein, E., Dryden, K., Claxton, D. P., McHaourab, H. S., Karakas, E., Ohi, M. D., & Kenworthy, A. K. (2020). Structure and assembly of CAV1 8S complexes revealed by single particle electron microscopy. *Science Advances*, *6*(49), 1–11. https://doi.org/10.1126/sciadv.abc6185

Hansen, C. G., Howard, G., & Nichols, B. J. (2011). Pacsin 2 is recruited to caveolae and functions in caveolar biogenesis. *Journal of Cell Science*, *124*(16), 2777–2785. https://doi.org/10.1242/jcs.084319

Hayer, A., Stoeber, M., Bissig, C., & Helenius, A. (2010). Biogenesis of caveolae: Stepwise assembly of large caveolin and cavin complexes. *Traffic*, *11*(3), 361–382. https://doi.org/10.1111/j.1600-0854.2009.01023.x

Hoernke, M., Mohan, J., Larsson, E., Blomberg, J., Kahra, D., Westenhoff, S., Schwieger, C., & Lundmark, R. (2017). EHD2 restrains dynamics of caveolae by an ATP- dependent, membrane-bound, open conformation. *PN*, *114*, E4360–E4369. https://doi.org/10.1073/pnas.1614066114

Hooy, R. M., Iwamoto, Y., Tudorica, D. A., Ren, X., & Hurley, J. H. (2022). Self-assembly and structure of a clathrin-independent AP-1:Arf1 tubular membrane coat. *Science Advances*, *8*(42), 1–14. https://doi.org/10.1126/sciadv.add3914

Hubert, M., Larsson, E., Vegesna, N. V. G., Ahnlund, M., Johansson, A. I., Moodie, L. W. K., & Lundmark, R. (2020). Lipid accumulation controls the balance between surface connection and scission of caveolae. *ELife*, *9*, 1–31. https://doi.org/10.7554/eLife.55038

Hutchings, J., Stancheva, V., Miller, E. A., & Zanetti, G. (2018). Subtomogram averaging of COPII assemblies reveals how coat organization dictates membrane shape. *Nature Communications*, *9*(1). https://doi.org/10.1038/s41467-018-06577-4

Ingerman, E., Perkins, E. M., Marino, M., Mears, J. A., Mccaffery, J. M., Hinshaw, J. E., & Nunnari, J. (2005). Dnm1 forms spirals that are structurally tailored to fit mitochondria. *The Journal of Cell Biology*, *170*(7), 1021–1027. https://doi.org/10.1083/jcb.200506078

Insinna, C., Lu, Q., Teixeira, I., Harned, A., Semler, E. M., Stauffer, J., Magidson, V., Tiwari, A., Kenworthy, A. K., Narayan, K., & Westlake, C. J. (2019). Investigation of F-BAR domain PACSIN proteins uncovers membrane tubulation function in cilia assembly and transport. *Nature Communications*, *10*(1), 1–17. https://doi.org/10.1038/s41467-018-08192-9

Joiner, A. M. N., & Fromme, J. C. (2021). Structural basis for the initiation of COPII vesicle

biogenesis. *Structure*, *29*(8), 859-872.e6. https://doi.org/10.1016/j.str.2021.03.013

Kaksonen, M., & Roux, A. (2018). Mechanisms of clathrin-mediated endocytosis. *Nature Reviews Molecular Cell Biology*, *19*(5), 313–326. https://doi.org/10.1038/nrm.2017.132

Kieken, F., Jović, M., Naslavsky, N., Caplan, S., & Sorgen, P. L. (2007). EH domain of EHD1. *Journal of Biomolecular NMR*, *39*(4), 323–329. https://doi.org/10.1007/s10858-007-9196-0

Kong, L., Sochacki, K. A., Wang, H., Fang, S., Canagarajah, B., Kehr, A. D., Rice, W. J., Strub, M. P., Taraska, J. W., & Hinshaw, J. E. (2018). Cryo-EM of the dynamin polymer assembled on lipid membrane. *Nature*, *560*(7717), 258–262. https://doi.org/10.1038/s41586-018-0378-6

Kovtun, O., Tillu, V. A., Jung, W. R., Leneva, N., Ariotti, N., Chaudhary, N., Mandyam, R. A., Ferguson, C., Morgan, G. P., Johnston, W. A., Harrop, S. J., Alexandrov, K., Parton, R. G., & Collins, B. M. (2014). Structural insights into the organization of the cavin membrane coat complex. *Developmental Cell*, *31*(4), 405–419. https://doi.org/10.1016/j.devcel.2014.10.002

Kozlov, M. M., & Taraska, J. W. (2023). Generation of nanoscopic membrane curvature for membrane trafficking. *Nature Reviews Molecular Cell Biology*, *24*(1), 63–78. https://doi.org/10.1038/s41580-022-00511-9

Kremer, J. R., Mastronarde, D. N., & McIntosh, J. R. (1996). Computer Visualization of Three-Dimensional Image Data Using IMOD. *Journal of Structural Biology*, *116*(1), 71–76. https://doi.org/https://doi.org/10.1006/jsbi.1996.0013

Kroppen, B., Teske, N., Yambire, K. F., Denkert, N., Mukherjee, I., Tarasenko, D., Jaipuria, G., Zweckstetter, M., Milosevic, I., Steinem, C., & Meinecke, M. (2021). Cooperativity of membrane - protein and protein – protein interactions control membrane remodeling by epsin 1 and affects clathrin - mediated endocytosis. *Cellular and Molecular Life Sciences*, *78*(5), 2355–2370. https://doi.org/10.1007/s00018-020-03647-z

Larsson, E., Morén, B., McMahon, K. A., Parton, R. G., & Lundmark, R. (2023). Dynamin2 functions as an accessory protein to reduce the rate of caveola internalization. *Journal of Cell Biology*, *222*(4). https://doi.org/10.1083/jcb.202205122

Lee, S., Uchida, Y., Wang, J., Matsudaira, T., Nakagawa, T., Kishimoto, T., Mukai, K., Inaba, T., Kobayashi, T., Molday, R. S., Taguchi, T., & Arai, H. (2015). Transport through recycling endosomes requires EHD 1 recruitment by a phosphatidylserine translocase. *EMBO Journal*, 1–20. https://doi.org/10.15252/embj.201489703

Leneva, N., Kovtun, O., Morado, D. R., Briggs, J. A. G., & Owen, D. J. (2021). Architecture and mechanism of metazoan retromer : SNX3 tubular coat assembly. *Science Advances*, *March*, 1–9. https://doi.org/DOI: 10.1126/sciadv.abf8598

Liebschner, D., Afonine, P. V., Baker, M. L., Bunkoczi, G., Chen, V. B., Croll, T. I., Hintze, B., Hung, L. W., Jain, S., McCoy, A. J., Moriarty, N. W., Oeffner, R. D., Poon, B. K., Prisant, M. G., Read, R. J., Richardson, J. S., Richardson, D. C., … Adams, P. D. (2019). Macromolecular structure determination using X-rays, neutrons and electrons: Recent developments in Phenix. *Acta Crystallographica Section D: Structural Biology*, *75*, 861–877. https://doi.org/10.1107/S2059798319011471

Lin, S. X., Grant, B. D., Hirsh, D., & Maxfield, F. R. (2001). Rme-1 regulates the distribution and function of the endocytic recycling compartment in mammalian cells. *Nature Cell Biology*, *3*(6), 567–572. https://doi.org/10.1038/35078543

Liu, J., Alvarez, F. J. D., Clare, D. K., Noel, J. K., & Zhang, P. (2021). CryoEM structure of the super-constricted two-start dynamin 1 filament. *Nature Communications*, *12*(1), 1–11. https://doi.org/10.1038/s41467-021-25741-x

Liu, R., & Chan, D. C. (2017). OPA1 and cardiolipin team up for mitochondrial fusion. *Nature Cell Biology*, *19*(7), 760–762. https://doi.org/10.1038/ncb3565

Liu, T. Y., Bian, X., Romano, F. B., Shemesh, T., Rapoport, T. A., & Hu, J. (2015). Cis and trans interactions between atlastin molecules during membrane fusion. *PNAS*, *112*, E1851-1860. https://doi.org/10.1073/pnas.1504368112

Lopez-Robles, C., Scaramuzza, S., Astorga-Simon, E. N., Ishida, M., Williamson, C. D., Baños-Mateos, S., Gil-Carton, D., Romero-Durana, M., Vidaurrazaga, A., Fernandez-Recio, J., Rojas, A. L., Bonifacino, J. S., Castaño-Díez, D., & Hierro, A. (2023). Architecture of the ESCPE-1 membrane coat. *Nature Structural and Molecular Biology*, *30*(7), 958–969. https://doi.org/10.1038/s41594-023-01014-7

Low, H. H., Sachse, C., Amos, L. A., & Löwe, J. (2009). Structure of a Bacterial Dynamin-like Protein Lipid Tube Provides a Mechanism For Assembly and Membrane Curving. *Cell*, *50*, 1342–1352. https://doi.org/10.1016/j.cell.2009.11.003

Lu, Q., Insinna, C., Ott, C., Stauffer, J., Pintado, P. A., Rahajeng, J., Baxa, U., Walia, V., Cuenca, A., Hwang, Y.-S., Daar, I. O., Lopes, S., Lippincott-Schwartz, J., Jackson, P. K., Caplan, S., & Westlake, C. J. (2015). Early steps in primary cilium assembly require EHD1/EHD3-dependent ciliary vesicle formation. *Nature Cell Biology*, *17*(3), 228–240. https://doi.org/10.1038/ncb3109

Ludwig, A., Howard, G., Mendoza-Topaz, C., Deerinck, T., Mackey, M., Sandin, S., Ellisman, M. H., & Nichols, B. J. (2013). Molecular Composition and Ultrastructure of the Caveolar Coat Complex. *PLoS Biology*, *11*(8). https://doi.org/10.1371/journal.pbio.1001640

Ludwig, A., Nichols, B. J., & Sandin, S. (2016). Architecture of the caveolar coat complex. *Journal of Cell Science*, *129*(16), 3077–3083. https://doi.org/10.1242/jcs.191262

Marg, A., Schoewel, V., Timmel, T., Schulze, A., Shah, C., Daumke, O., & Spuler, S. (2012). Sarcolemmal Repair Is a Slow Process and Includes EHD2. *Traffic*, *13*(9), 1286–1294. https://doi.org/10.1111/j.1600-0854.2012.01386.x

Martens, S., Kozlov, M. M., & McMahon, H. T. (2007). How Synaptotagmin Promotes Membrane Fusion. *Science*, *316*, 1205–1209.

Mastronarde, D. N. (2005). Automated electron microscope tomography using robust prediction of specimen movements. *Journal of Structural Biology*, *152*(1), 36–51. https://doi.org/10.1016/j.jsb.2005.07.007

Matthaeus, C., Lahmann, I., Kunz, S., Jonas, W., Melo, A. A., Lehmann, M., Larsson, E., Lundmark, R., Kern, M., Blüher, M., Olschowski, H., Kompa, J., Brügger, B., Müller, D. N., Haucke, V., Schürmann, A., Birchmeier, C., & Daumke, O. (2020). EHD2-mediated restriction of caveolar dynamics regulates cellular fatty acid uptake. *Proceedings of the National Academy of Sciences of the United States of America*, *117*(13), 7471–7481. https://doi.org/10.1073/pnas.1918415117

Matthaeus, C., Lian, X., Kunz, S., Lehmann, M., Zhong, C., Bernert, C., Lahmann, I., Müller, D. N., Gollasch, M., & Daumke, O. (2019). ENOS-NO-induced small blood vessel relaxation requires EHD2-dependent caveolae stabilization. *PLoS ONE*, *14*(10), 1–22. https://doi.org/10.1371/journal.pone.0223620

Matthaeus, C., Sochacki, K. A., Dickey, A. M., Puchkov, D., Haucke, V., Lehmann, M., & Taraska, J. W. (2022). The molecular organization of differentially curved caveolae indicates bendable structural units at the plasma membrane. *Nature Communications*, *13*(1). https://doi.org/10.1038/s41467-022-34958-3

Matthaeus, C., & Taraska, J. W. (2021). Energy and Dynamics of Caveolae Trafficking. *Frontiers in Cell and Developmental Biology*, *8*(January). https://doi.org/10.3389/fcell.2020.614472

Mcbride, H. M., & Frost, A. (2016). Double agents for mitochondrial division. *Nature*, *540*, 43–44. https://doi.org/10.1038/nature20482

McMahon, H. T., & Boucrot, E. (2011). Molecular mechanism and physiological functions of clathrin-mediated endocytosis. *Nature Reviews Molecular Cell Biology*, *12*(8), 517–533.

https://doi.org/10.1038/nrm3151

McMahon, H. T., & Boucrot, E. (2015). Membrane curvature at a glance. *Journal of Cell Science*, *128*(6), 1065–1070. https://doi.org/10.1242/jcs.114454

McMahon, H. T., & Gallop, J. L. (2005). Membrane curvature and mechanisms of dynamic cell membrane remodelling. *Nature*, *438*(December), 590–596. https://doi.org/10.1038/nature04396

Melo, A. A., Hegde, B. G., Shah, C., Larsson, E., Isas, J. M., Kunz, S., Lundmark, R., Langen, R., & Daumke, O. (2017). Structural insights into the activation mechanism of dynamin-like EHD ATPases. *PNAS*, *2*(10), 1–6. https://doi.org/10.1073/pnas.1614075114

Melo, A. A., Sprink, T., Noel, J. K., Vázquez-Sarandeses, E., van Hoorn, C., Mohd, S., Loerke, J., Spahn, C. M. T., & Daumke, O. (2022). Cryo-electron tomography reveals structural insights into the membrane remodeling mode of dynamin-like EHD filaments. *Nature Communications*, *13*(1), 1–13. https://doi.org/10.1038/s41467-022-35164-x

Meunier, E., Dick, M. S., Dreier, R. F., Schürmann, N., Kenzelmann Broz, D., Warming, S., Roose-Girma, M., Bumann, D., Kayagaki, N., Takeda, K., Yamamoto, M., & Broz, P. (2014). Caspase-11 activation requires lysis of pathogen-containing vacuoles by IFN-induced GTPases. *Nature*, *509*(7500), 366–370. https://doi.org/10.1038/nature13157

Miller, S. E., Mathiasen, S., & Owen, D. J. (2015). Article CALM Regulates Clathrin-Coated Vesicle Size and Maturation by Directly Sensing and Driving Article CALM Regulates Clathrin-Coated Vesicle Size and Maturation by Directly Sensing and Driving Membrane Curvature. *Developmental Cell*, 163–175. https://doi.org/10.1016/j.devcel.2015.03.002

Morén, B., Hansson, B., Negoita, F., Fryklund, C., Lundmark, R., Göransson, O., & Stenkula, K. G. (2019). EHD2 regulates adipocyte function and is enriched at cell surface-associated lipid droplets in primary human adipocytes. *Molecular Biology of the Cell*, *30*(10), 1147–1159. https://doi.org/10.1091/mbc.E18-10-0680

Morén, B., Shah, C., Howes, M. T., Schieber, N. L., McMahon, H. T., Parton, R. G., Daumke, O., & Lundmark, R. (2012). EHD2 regulates caveolar dynamics via ATP-driven targeting and oligomerization. *Molecular Biology of the Cell*, *23*, 1316–1329. https://doi.org/10.1091/mbc.E11-09-0787

Naslavsky, N., Boehm, M., Backlund, P. S., & Caplan, S. (2004). Rabenosyn-5 and EHD1 Interact and Sequentially Regulate Protein Recycling to the Plasma Membrane. *Molecular Biology of the Cell*, *15*(May), 2410–2422. https://doi.org/10.1091/mbc.E03

Naslavsky, N., & Caplan, S. (2011). EHD proteins : key conductors of endocytic transport. *Trends*

in Cell Biology, *21*(2), 122–131. https://doi.org/10.1016/j.tcb.2010.10.003

Naslavsky, N., Mckenzie, J., Altan-bonnet, N., Sheff, D., & Caplan, S. (2009). EHD3 regulates early-endosome-to-Golgi transport and preserves Golgi morphology. *Journal of Cell Science*, *122*, 389–400. https://doi.org/10.1242/jcs.037051

Noel, J. K., Levi, M., Raghunathan, M., Lammert, H., Hayes, R. L., Onuchic, J. N., & Whitford, P. C. (2016). SMOG 2: A Versatile Software Package for Generating Structure-Based Models. *PLoS Computational Biology*, *12*(3), 1–14. https://doi.org/10.1371/journal.pcbi.1004794

Oh, P., Horner, T., Witkiewicz, H., & Schnitzer, J. E. (2012). Endothelin induces rapid, dynamin-mediated budding of endothelial caveolae rich in ET-B. *Journal of Biological Chemistry*, *287*(21), 17353–17362. https://doi.org/10.1074/jbc.M111.338897

Pant, S., Sharma, M., Patel, K., Caplan, S., Carr, C. M., & Grant, B. D. (2009). AMPH-1/Amphiphysin/Bin1 functions with RME-1/Ehd in endocytic recycling. *Nat Cell Biol.*, *11*(12), 1399–1410. https://doi.org/10.1038/ncb1986.AMPH-1/Amphiphysin/Bin1

Parton, R. G., Del Pozo, M. A., Vassilopoulos, S., Nabi, I., Le Lay, S., Lundmark, R., Kenworthy, A. K., Camus, A., Blouin, C., Sessa, W. C., & Lamaze, C. (2020). Caveolae: The FAQs. *Traffic*, *21*(1), 181–185. https://doi.org/10.1111/tra.12689

Parton, R. G., Kozlov, M. M., & Ariotti, N. (2020). Caveolae and lipid sorting: Shaping the cellular response to stress. *Journal of Cell Biology*, *219*(4), 1–13. https://doi.org/10.1083/JCB.201905071

Parton, R. G., McMahon, K. A., & Wu, Y. (2020). Caveolae: Formation, dynamics, and function. *Current Opinion in Cell Biology*, *65*, 8–16. https://doi.org/10.1016/j.ceb.2020.02.001

Pavlin, M. R., & Hurley, J. H. (2020). The ESCRTs – converging on mechanism. *Journal of Cell Science*. https://doi.org/10.1242/jcs.240333

Pilch, P. F., & Liu, L. (2011). Fat caves: Caveolae, lipid trafficking and lipid metabolism in adipocytes. *Trends in Endocrinology and Metabolism*, *22*(8), 318–324. https://doi.org/10.1016/j.tem.2011.04.001

Plomann, M., Wittmann, J. G., & Rudolph, M. G. (2010). A Hinge in the Distal End of the PACSIN 2 F-BAR Domain May Contribute to Membrane-Curvature Sensing. *Journal of Molecular Biology*, *400*(2), 129–136. https://doi.org/10.1016/j.jmb.2010.05.008

Porta, J. C., Han, B., Gulsevin, A., Chung, J. M., Peskova, Y., Connolly, S., McHaourab, H. S., Meiler, J., Karakas, E., Kenworthy, A. K., & Ohi, M. D. (2022). Molecular architecture of

the human caveolin-1 complex. *Science Advances*, *8*(19), 1–9. https://doi.org/10.1126/sciadv.abn7232

Praefcke, G. J. K., & McMahon, H. T. (2004). The dynamin superfamily: universal membrane tubulation and fission molecules? *Nat Rev Mol Cell Bio*, *5*(February), 133–147. https://doi.org/10.1038/nrm1313

Rai, A., Bleimling, N., Vetter, I. R., & Goody, R. S. (2020). The mechanism of activation of the actin binding protein EHBP1 by Rab8 family members. *Nature Communications*, *11*(1), 1–16. https://doi.org/10.1038/s41467-020-17792-3

Rao, Y., Ma, Q., Vahedi-Faridi, A., Sundborger, A., Pechstein, A., Puchkov, D., Luo, L., Shupliakov, O., Saenger, W., & Haucke, V. (2010). Molecular basis for SH3 domain regulation of F-BAR-mediated membrane deformation. *Proceedings of the National Academy of Sciences of the United States of America*, *107*(18), 8213–8218. https://doi.org/10.1073/pnas.1003478107

Rapaport, D., Auerbach, W., Naslavsky, N., Pasmanik-Chor, M., Galperin, E., Fein, A., Caplan, S., Joyner, A. L., & Horowitz, M. (2006). Recycling to the plasma membrane is delayed in EHD1 knockout mice. *Traffic*, *7*(1), 52–60. https://doi.org/10.1111/j.1600-0854.2005.00359.x

Reubold, T. F., Eschenburg, S., Becker, A., Leonard, M., Schmid, S. L., Vallee, R. B., Kull, F. J., & Manstein, D. J. (2005). Crystal structure of the GTPase domain of rat dynamin 1. *PNAS*, *102*, 13093–13098.

Reubold, T. F., Faelber, K., Plattner, N., Posor, Y., Ketel, K., Curth, U., Schlegel, J., Anand, R., Manstein, D. J., Noé, F., Haucke, V., Daumke, O., & Eschenburg, S. (2015). Crystal structure of the dynamin tetramer. *Nature*, *525*(7569), 404–408. https://doi.org/10.1038/nature14880

Richter, T., Floetenmeyer, M., Ferguson, C., Galea, J., Goh, J., Lindsay, M. R., Morgan, G. P., Marsh, B. J., & Parton, R. G. (2008). High-resolution 3D quantitative analysis of caveolar ultrastructure and caveola-cytoskeleton interactions. *Traffic*, *9*(6), 893–909. https://doi.org/10.1111/j.1600-0854.2008.00733.x

Rizzo, V., McIntosh, D. P., Oh, P., & Schnitzer, J. E. (1998). In situ flow activates endothelial nitric oxide synthase in luminal caveolae of endothelium with rapid caveolin dissociation and calmodulin association. *Journal of Biological Chemistry*, *273*(52), 34724–34729. https://doi.org/10.1074/jbc.273.52.34724

Sandvig, K., Kavaliauskiene, S., & Skotland, T. (2018). Clathrin-independent endocytosis: an

increasing degree of complexity. *Histochemistry and Cell Biology*, *150*(2), 107–118. https://doi.org/10.1007/s00418-018-1678-5

Sandvig, K., Pust, S., Skotland, T., & van Deurs, B. (2011). Clathrin-independent endocytosis: Mechanisms and function. *Current Opinion in Cell Biology*, *23*(4), 413–420. https://doi.org/10.1016/j.ceb.2011.03.007

Schneider, C. A., Rasband, W. S., & Eliceiri, K. W. (2012). NIH Image to ImageJ: 25 years of Image Analysis HHS Public Access. *Nat Methods*, *9*(7), 671–675.

Senju, Y., Itoh, Y., Takano, K., Hamada, S., & Suetsugu, S. (2011). Essential role of PACSIN2/syndapin-II in caveolae membrane sculpting. *Journal of Cell Science*, *124*(12), 2032–2040. https://doi.org/10.1242/jcs.086264

Shah, C. (2013). Structural and mechanistic analysis of membrane remodeling by Eps15-homology domain-containing protein 2. *PhD Thesis*. https://refubium.fu-berlin.de/handle/fub188/2340

Shah, C., Hegde, B. G., Morén, B., Behrmann, E., Mielke, T., Moenke, G., Spahn, C. M. T., Lundmark, R., & Daumke, O. (2014). Structural insights into membrane interaction and caveolar targeting of dynamin-like EHD2. *Structure*, *22*(3), 409–420. https://doi.org/10.1016/j.str.2013.12.015.Structural

Shajahan, A. N., Timblin, B. K., Sandoval, R., Tiruppathi, C., Malik, A. B., & Minshall, R. D. (2004). Role of Src-induced Dynamin-2 Phosphorylation in Caveolae-mediated Endocytosis in Endothelial Cells. *Journal of Biological Chemistry*, *279*(19), 20392–20400. https://doi.org/10.1074/jbc.M308710200

Sharma, M., Giridharan, S. S. P., Rahajeng, J., Caplan, S., & Naslavsky, N. (2010). An unusual Rab effector that links EHD1 to tubular recycling endosomes. *Communicative & Integrative Biology*, *3:2*(April), 181–183. https://doi.org/10.1091/mbc.E09-06-0535.key

Sharma, M., Naslavsky, N., & Caplan, S. (2008). A Role for EHD4 in the Regulation of Early Endosomal Transport. *Traffic*, *9*(6), 995–1018. https://doi.org/10.1111/j.1600-0854.2008.00732.x.A

Sotodosos-Alonso, L., Pulgar, M., & Pozo, M. A. (2023). Caveolae Mechanotransduction at the Interface between Cytoskeleton. *Cells*, *12*(942). https://doi.org/https://doi.org/10.3390/cells12060942

Soulet, F., Yarar, D., Leonard, M., & Schmid, S. L. (2005). SNX9 Regulates Dynamin Assembly and Is Required for Efficient Clathrin-mediated Endocytosis. *Mol Bio Cell*, *16*(April), 2058–2067. https://doi.org/10.1091/mbc.E04

Stoeber, M., Schellenberger, P., Siebert, C. A., Leyrat, C., Helenius, A., & Grünewald, K. (2016). Model for the architecture of caveolae based on a flexible, net-like assembly of Cavin1 and Caveolin discs. *Proceedings of the National Academy of Sciences of the United States of America*, *113*(50), E8069–E8078. https://doi.org/10.1073/pnas.1616838113

Stoeber, M., Stoeck, I. K., HéCurrency Signnni, C., Bleck, C. K. E., Balistreri, G., & Helenius, A. (2012). Oligomers of the ATPase EHD2 confine caveolae to the plasma membrane through association with actin. *EMBO Journal*, *31*(10), 2350–2364. https://doi.org/10.1038/emboj.2012.98

Sundquist, W. I., & Kra, H. (2012). HIV-1 Assembly, Budding, and Maturation. *Cold Spring Harb Perspect Med*, 1–24. https://doi.org/doi: 10.1101/cshperspect.a006924

Thottacherry, J. J., Sathe, M., Prabhakara, C., & Mayor, S. (2019). Spoiled for choice: Diverse endocytic pathways function at the cell surface. *Annual Review of Cell and Developmental Biology*, *35*, 55–84. https://doi.org/10.1146/annurev-cellbio-100617-062710

Vanni, S., Vamparys, L., Gautier, R., Drin, G., Etchebest, C., Fuchs, P. F. J., & Antonny, B. (2013). Amphipathic lipid packing sensor motifs: Probing bilayer defects with hydrophobic residues. *Biophysical Journal*, *104*(3), 575–584. https://doi.org/10.1016/j.bpj.2012.11.3837

Von Der Malsburg, A., Abutbul-Ionita, I., Haller, O., Kochs, G., & Danino, D. (2011). Stalk domain of the dynamin-like MxA GTPase protein mediates membrane binding and liposome tubulation via the unstructured L4 loop. *Journal of Biological Chemistry*, *286*(43), 37858–37865. https://doi.org/10.1074/jbc.M111.249037

Wang, S., Tukachinsky, H., Romano, F. B., & Rapoport, T. A. (2016). Cooperation of the ER-shaping proteins atlastin, lunapark, and reticulons to generate a tubular membrane network. *ELife*, *5*(September), 1–29. https://doi.org/10.7554/eLife.18605

Watson, H. (2015). Biological membranes. *Essays Biochem*, *59*, 43–69. https://doi.org/10.1042/BSE0590043

Weissenberger, G., Henderikx, R. J. M., & Peters, P. J. (2021). Understanding the invisible hands of sample preparation for cryo-EM. *Nature Methods*, *18*(5), 463–471. https://doi.org/10.1038/s41592-021-01130-6

Winn, M. D., Ballard, C. C., Cowtan, K. D., Dodson, E. J., Emsley, P., Evans, P. R., Keegan, R. M., Krissinel, E. B., Leslie, A. G. W., McCoy, A., McNicholas, S. J., Murshudov, G. N., Pannu, N. S., Potterton, E. A., Powell, H. R., Read, R. J., Vagin, A., & Wilson, K. S. (2011). Overview of the CCP4 suite and current developments. *Acta Crystallographica Section D: Biological Crystallography*, *67*(4), 235–242. https://doi.org/10.1107/S0907444910045749

Wu, L.-G., Hamid, E., Shin, W., & Chiang, H.-C. (2016). Exocytosis and Endocytosis: Modes, Functions, and Coupling Mechanisms. *Annu Rev Physiol*, *176*(5), 139–148. https://doi.org/10.1146/annurev-physiol-021113-170305

Xie, S., Reinecke, J. B., Farmer, T., Bahl, K., Yeow, I., Nichols, B. J., McLamarrah, T. A., Naslavsky, N., Rogers, G. C., & Caplan, S. (2018). Vesicular trafficking plays a role in centriole disengagement and duplication. *Molecular Biology of the Cell*, *29*(22), 2622–2631. https://doi.org/10.1091/mbc.E18-04-0241

Yeow, I., Howard, G., Chadwick, J., Mendoza-Topaz, C., Hansen, C. G., Nichols, B. J., & Shvets, E. (2017). EHD Proteins Cooperate to Generate Caveolar Clusters and to Maintain Caveolae during Repeated Mechanical Stress. *Current Biology : CB*, *27*(19), 2951-2962.e5. https://doi.org/10.1016/j.cub.2017.07.047

Zhang, J., Naslavsky, N., & Caplan, S. (2012). *Rabs and EHDs : alternate modes for traffic control Bioscience Reports*. *32*, 17–23. https://doi.org/10.1042/BSR20110009

Acknowledgements

I would like to thank my supervisor Oliver Daumke for the support and the trust he gave me throughout these years. Thank you for passing on your optimism and for always pursuing new techniques, approaches, and ideas. It is inspiring.

I have felt welcomed and supported at all times since I joined the lab and I am thankful to all members for that. Daily suggestions, and advice from all of them have helped me carry out my project and write this thesis. Ashwin, thanks for proof-reading the results and discussion. Eva, thanks for the feedback about the introduction. Marius, *vielen Dank für die Übersetzung(en)*.

I want to thank the cryo-EM facility in Buch for access to data collection. Especially, thanks to Thiemo for always being available for any sort of request. I want to thank Séverine and Mara from the EM facility from the MDC, for (countless) sample preparations and for brainstorming and pushing so hard. I want to thank Jeff for fitting the models and doing his molecular dynamics sorcery.

I would like to thank Arthur because he has been there since day one. Thanks for taking me as an intern that summer. It changed the course of my life and has led me to this page today. I learnt a lot from you, both scientifically and on a personal level, and I'm grateful for that. Your feedback and enthusiasm about my thesis kept me sane these last weeks. I feel I am in debt.

Krystof, you are a great and fun person. Thanks for always being up for beers. I wish you had joined earlier! Julia, I thank you for listening and for the countless advice. Connecting with you and thinking alike made my days in Buch much better. I admire your knowledge and your passion in life and I just hope I stay like you over the years. Eva, I want to thank you for your energy, for being social and fun. I cannot express how happy it made me that you joined the lab. I found a loyal beer hour companion, a daily dose of drama and gossip, and a source of fresh and young Gen-Z vocabulary. Most importantly, I found a solid friend. *You've made my days lit cuz you slay gurl*.

Vasilii, I am writing these acknowledgements the day after we left the club Anomalie at 7 am on a Saturday morning and I can only feel extremely fortunate because not everyone gets to collaborate with a close friend. Or should I say that not everyone gets to go clubbing with a collaborator? Both. I am inspired by your always positive mood, your sense of humor and your chilled and easy-going vibes. I could not think of a better fit for a collaboration. Thanks for the amazing work you put into this project and for your clever strategies, I am amazed! I must say that all the pages preceding this one would not have been possible without you.

I want to thank Chaves, Lidia and Naza for the trips, the nights out and for always showing interest in my research project - professional acting you guys! Clàudia, Carla, *sou genials*. I would like to

mention the amazing ballerinas who have made my ballet training evenings an exhausting, delightful and therapeutic time.

Irene, I cannot find the words to express what your friendship has meant to me all these years. I am thankful for having found you, I never thought I could match with someone on so many aspects. It has not been a smooth road but having you by my side at all times made everything much easier. I only hope I have served the same purpose for you. Thanks for listening to my complaints, frustrations and fears with patience and sympathy, and for celebrating with me my achievements and joys. We have had so much fun!!!! I am really sad that this chapter is coming to an end, and I must say that I am scared of a future in which there is no Berlin and in which we will spend less time together. And now it is when I would text "Irene, I need a *Weinerei* session". Do not worry, I am sure that we will find our *Flaschen der Woche* somewhere else. I am proud of you and of the person you have become over these years. Seeing you grow has made me grow better. Now we are very close to starting our postdocs and I can only think of taking holidays to go see each other. Meeting you is the best that this PhD has given me, seriously.

I want to thank the VBB for their great achievement in keeping the S-Bahn running in January and February 2019. Any of the frequent interruptions in the S2 could have made it impossible for me to meet Facu.

Facu, on our first date I told you that I had just started my PhD and that at least 4.5 years were ahead of me. I still cannot believe that that day you decided to embark in this long journey. You have been my greatest companion. Thank you for encouraging me, for deciphering my moods, for the patience and the endless affection and love. I could not have won this battle without your strength. Thank you for making me feel special and for valuing the career I chose. Exploring and understanding life next to you is the greatest learning I take from these years. Thank you for being there every day of the way. *Te quiero*.

My sister Alicia is hardworking, ambitious and one of the smartest people I know. Her rational and down-to-earth advice have helped me in the past years, and I am sure it will continue to be like this because she has been setting an example for me since I was born. *Gracias*.

My parents Alicia and Antonio are responsible for this accomplishment. The nurturing environment of affection, tolerance, culture, and books that characterized my childhood has shaped me into the person I am today and has led me towards this doctoral degree. I was privileged and I could never thank them enough. Throughout these years they have expressed genuine interest, unwavering support and unconditional love. *Os quiero mucho*.

I kept reminding myself my grandaunt Mer's words *"no te atosigues"* all this time. I miss you.